Marina Zajnulina

Optical frequency comb generation in optical fibres

Dissertation zur Erlangung des akademischen Grades
"doctor rerum naturalium" (Dr. rer. nat.)
in der Wissenschaftsdisziplin "Photonik"

Eingereicht
an der Mathematisch-Naturwissenschaftlichen Fakultät
der Universität Potsdam

2015

Published online at the
Institutional Repository of the University of Potsdam:
URN urn:nbn:de:kobv:517-opus4-88776
http://nbn-resolving.de/urn:nbn:de:kobv:517-opus4-88776

Selbstständigkeitserklärung

Ich erkläre hiermit, dass ich die vorliegende Doktorarbeit selbstständig und ohne fremde Hilfe verfasst, andere als die angegeben Quellen und Hilfsmittel nicht benutzt und die den benutzten Quellen wörtlich oder inhaltlich entnommenen Stellen als solche kenntlich gemacht habe. Die Arbeit wurde bisher in gleicher oder ähnlicher Form keiner anderen Prüfungskommission vorgelegt. Die Publikationen, für die Ergebnisse dieser Arbeit verwendet worden waren, sind in der Publikationsliste (List of Publications) zusammengefasst.

Declaration of Academic Honesty

I confirm that this doctoral thesis was written completely by me and without anyone's help. All information sources used for this work are either clearly cited or mentioned by the author's name. This thesis (in the presented or a similar framework) has not been submitted anywhere else. Publications that use results out of this the thesis are listed in the publication list.

Synopsis in English

Optical frequency combs (OFC) constitute an array of phase-correlated equidistant spectral lines with nearly equal intensities over a broad spectral range. The adaptations of combs generated in mode-locked lasers proved to be highly efficient for the calibration of high-resolution (resolving power > 50000) astronomical spectrographs. The observation of different galaxy structures or the studies of the Milky Way are done using instruments in the low- and medium resolution range. To such instruments belong, for instance, the Multi Unit Spectroscopic Explorer (MUSE) being developed for the Very Large Telescope (VLT) of the European Southern Observatory (ESO) and the 4-metre Multi-Object Spectroscopic Telescope (4MOST) being in development for the ESO VISTA 4.1 m Telescope. The existing adaptations of OFC from mode-locked lasers are not resolvable by these instruments.

Within this work, a fibre-based approach for generation of OFC specifically in the low- and medium resolution range is studied numerically. This approach consists of three optical fibres that are fed by two equally intense continuous-wave (CW) lasers. The first fibre is a conventional single-mode fibre, the second one is an amplifying Erbium-doped fibre with anomalous dispersion, and the third one is a low-dispersion highly nonlinear optical fibre. The evolution of a frequency comb in this system is governed by the following processes: as the two initial CW-laser waves with different frequencies propagate through the first fibre, they generate an initial comb via a cascade of four-wave mixing processes. The frequency components of the comb are phase-correlated with the original laser lines and have a frequency spacing that is equal to the initial laser frequency separation (*LFS*), i.e. the difference in the laser frequencies. In the time domain, a train of pre-compressed pulses with widths of a few pico-seconds arises out of the initial bichromatic deeply-modulated cosine-wave. These pulses undergo strong compression in the subsequent amplifying Erbium-doped fibre: sub-100 fs pulses with broad OFC spectra are formed. In the following low-dispersion highly nonlinear fibre, the OFC experience a further broadening and the intensity of the comb lines are fairly equalised. This approach was mathematically modelled by means of a Generalised Nonlinear Schrödinger Equation (GNLS) that contains terms describing the nonlinear optical Kerr effect, the delayed Raman response, the pulse self-steepening, and the linear optical losses as well as the wavelength-dependent Erbium gain profile for the second fibre. The initial condition equation being a deeply-modulated cosine-wave mimics the radiation of the two initial CW lasers. The numerical studies are performed with the help of Matlab scripts that were specifically developed for the integration of the GNLS and the initial condition according to the proposed approach for the OFC generation. The scripts are based on the Fourth-Order Runge-Kutta in the Interaction Picture Method (RK4IP) in combination with the local error method.

Before the results are described, the reader is introduced into the theoretical framework. So, an overview about OFC and their application in the Astronomy is given. The fibre-based approach for the generation of OFC in the low- and medium-resolution

range is presented in detail. Then, a step-by-step derivation of the mathematical model (GNLS + initial condition) is given. The GNLS describing the light propagation in optical fibres can have different solutions. The reader is introduced to the types of solutions that are important to understand the performed studies and achieved results, namely to solitary waves (fundamental and higher-order solitons) and to periodic waves (Akhmediev breathers, Kuznetsov-Ma solitons) as well as to soliton molecules. Then, adiabatic and non-adiabatic soliton compression is briefly described.

The studies began with the numerical calculation of the optimum lengths of the first and second fibre of the proposed fibre-based approach. At the optimum lengths, the optical pulses exhibit maximal compression and, thus, broadest possible OFC, but also the minimal level of intensity noise that characterises the pulse-to-pulse variation. The optimum lengths were calculated for three different typical values of the group-velocity dispersion (GVD) parameters of the first fibre, namely for $-7.5\ \mathrm{ps}^2/\mathrm{km}$, $-15\ \mathrm{ps}^2/\mathrm{km}$, and $-30\ \mathrm{ps}^2/\mathrm{km}$ as well as for three values of *LFS* (*LSF* = 40 GHz, 80 GHz, and 160 GHz). Depending on the GVD parameter of the first fibre and the initial laser power, the optimum lengths of the first fibre varied from 180 m to 980 m, whereas of the second amplifying fibre between 7.5 m and 37.5 m. For different values of *LFS* and different values of the laser input power, the optimum lengths ranged between 150 m and 1100 m for the first fibre and between 7 m and 35 m for the second fibre. The best system performance was shown for the GVD parameter of $-15\ \mathrm{ps}^2/\mathrm{km}$, and a *LFS* of 80 GHz.

At low power values, the optimum lengths of the first fibre showed no variation with the initial laser power. This gave rise to more detailed studies of the optical pulse formation in the first fibre by means of the numerical technique called Soliton Radiation Beat Analysis (SRBA). The understanding of the optical pulse formation is crucial for the ability to control the OFC generation within the experiment. The SRBA was performed for three different initial conditions (a single pulse, an Akhmediev breather, and a bichromatic deeply-modulated cosine-wave). The GVD parameter was $-15\ \mathrm{ps}^2/\mathrm{km}$, and the laser frequency separation *LFS* = 80 GHz. After a comparison of the different results, it was found that a collective soliton crystal state appears for low input power values. The soliton crystal continuously dissolves into separated optical solitons as the laser input power increases. In the region where the soliton crystal exists, the optimum lengths of the first fibre are independent of the initial laser power. According to the SRBA results, it was predicted that the best OFC are formed in the first fibre for the input powers between 1.0 W and 2.0 W.

Further SRBA studies showed that the pulse formation in the second amplifying Erbium-doped fibre is critically dependent on the features of the pulses formed in the first fibre. Thus, adiabatic soliton compression delivering low-noise OFC occurs in the second fibre for low values of the input power. At these values, the pulses formed in the first fibre have low soliton orders. At high values of the input power, the pulses in the first fibre have more complicated structures which leads to the pulse break-up in the second fibre with a subsequent degradation of the OFC noise performance. Best OFC

in the second amplifying fibre are predicted for the input powers between 2.0 W and 2.8 W for LFS = 80 GHz and between 4.0 W and 4.5 W for LFS = 160 GHz.

The pulse intensity noise studies that were performed within the framework of this thesis allow making statements about the noise performance of an OFC. Such studies showed that the intensity noise of the whole system decreases with the increasing laser frequency separation. Thus, the intensity noise goes up 10% for LFS = 40 GHz and can be kept below 1% for LFS = 80 GHz and LFS = 160 GHz. So, higher values of the laser frequency separation are preferable to obtain low-noise OFC.

Synopsis in German

Optische Frequenzkämme (OFK) stellen ein diskretes optisches Spektrum mit phasenkorrelierten Linien dar, die gleichen spektralen Abstand voneinander haben und fast gleiche Intensität über einen größeren Spektralbereich aufweisen. In modengelockten Lasern generierte Kämme haben sich als höchst effizient für die Kalibrierung von hochauflösenden (Auflösungsvermögen > 50000) astronomischen Spektrografen erwiesen. Die astronomische Beobachtung von verschiedenen Galaxie-Strukturen oder die Studien der Milchstraße werden jedoch mit Hilfe von nieder- bis mittelauflösenden Instrumenten gemacht. Zu solchen Instrumenten gehören zum Beispiel der Multi-Spectroscopic-Exproler (MUSE), der gerade für das Very-Large-Telescope (VLT) der Europäischen Südsternwarte (ESO) entwickelt wird, und das 4-metre-Multi-Object-Spectroscopic-Telescope (4MOST), das sich in der Entwicklung für das ESO-VISTA-4,1m-Teleskop befindet. Die existierenden Anpassungen von OFK von modengelockten Lasern sind für solche Instrumente nicht auflösbar.

Im Rahmen dieser Arbeit wird ein faserbasierter Ansatz für die Generierung von OFK für den Bereich der nieder- bis mittelauflösenden Instrumente numerisch studiert. Die experimentelle Umsetzung dieses Ansatzes besteht aus drei optischen Fasern, in die das Strahlungsfeld von zwei Dauerstrichlasern mit gleicher Intensität eingespeist wird. Die erste Faser ist eine konventionelle Monomodefaser, die zweite ist eine Erbium-dotierte Verstärkerfaser mit negativer Dispersion, die dritte ist eine hochnichtlineare Faser mit niedriger Dispersion. Die Entwicklung eines OFKs in diesem System geschieht auf folgende Art und Weise: als die Laserwellen mit verschiedenen Frequenzen sich durch die erste Faser ausbreiten, erzeugen sie einen Anfangskamm durch einen Kaskadenprozess der Vier-Wellen-Mischung (VWM). Die neu entstandenen Frequenzkomponenten des Kamms sind frequenzkorreliert und haben einen spektralen Abstand, der der Laserfrequenzseparation (*LFS*) gleicht. Dies entspricht dem Entstehen von einem Zug von prä-komprimierten optischen Impulsen mit Impulsbreiten von einigen Pikosekunden in der Zeitdomäne. Diese Impulse werden strakt komprimiert in der nachfolgenden Erbium-dotierten Faser: es entstehen Sub-100-Femtosekunden-Impulse mit breiten OFK-Spektren. In der anschließenden hochnichtlinearen Faser wird das Kamm-Spektrum weiter verbreitet, während seine Frequenzlinien in ihren Intensitäten ausgeglichen werden. Dieser Ansatz wurde mathematisch mit Hilfe einer Verallgemeinerten Nichtlinearen Schrödinger Gleichung (VNSG) modelliert, die die Terme für den nichtlinearen optischen Kerr-Effekt, den Raman-Effekt, die Impuls-Selbstaufsteilung, die optischen Verluste und das wellenlängenabhängigen Erbium-Verstärkungsprofil für die zweite Faser enthält. Die Gleichung der Anfangsbedingung von der Form einer bichromatischen tief durchmodulierten Kosinus-Welle repräsentiert das Strahlungsfeld zweier Dauerstrichlaser. Die numerischen Studien sind mit Hilfe von Matlab-Skripten durchgeführt, die speziell fr die numerische Integration der VNSG mit der bichromatischen Kosinus-Welle als Anfangsbedingung entworfen worden sind. Diese Skripte basieren auf dem numerischen Verfahren genannt Fourth-Order Runge-Kutta in the Interaction Picture Method, das mit der Methode der Auswertung von lokalen nu-

merischen Fehlern kombiniert wurde.

Bevor zu dem Teil mit den Ergebnissen übergegangen wird, wird die Leserin oder der Leser mit den theoretischen Grundlagen dieser Arbeit vertraut gemacht. Als Erstes wird ein Überblick über die OFK und deren Einsatz in der Astronomie gegeben. Dann wird eine detaillierte Beschreibung des faserbasierten Ansatzes fr die Generierung von OFK für den nieder- bis mittelauflsenden Bereich aufgeführt. Danach wird eine schrittweise durchgeführte Herleitung der VNSG mit der bichromatischen Kosinus-Welle als Anfangsbedingung präsentiert. Die VNSG, die die Ausbreitung der optischen Impulse in optischen Fasern beschreibt, kann verschiedene Lösungen haben. Wir präsentieren die Typen von Lösungen, die für das Verständnis dieser Arbeit relevant sind, nämlich die solitären Wellen (fundamentale Solitonen und die Solitonen höherer Ordnung) und die periodischen Wellen (die Akhmediev-Breather und die Kuznetsov-Ma-Solitonen). Anschließend beschreiben wir den Prozess der adiabatischen und nichtadiabatischen Solitonen-Kompression in optischen Fasern.

Unsere Studien begangen mit der Berechnung von optimalen Längen der ersten und der zweiten Faser des präsentierten Ansatzes. Die optimalen Faserlängen sind durch die maximale Impuls-Kompression und die breitesten OFK gekennzeichnet. Gleichzeitig ist das Intensitätsrauschen, das durch die Variation der Impuls-Spitzenleistung beschrieben wird, bei optimalen Faserlängen minimal. Die optimalen Längen werden für drei verschiedene Werte der Gruppengeschwindigkeitsdispersion (GGD) der ersten Faser ($-7.5\ \mathrm{ps}^2/\mathrm{km}$, $-15\ \mathrm{ps}^2/\mathrm{km}$ und $-30\ \mathrm{ps}^2/\mathrm{km}$) und für drei Werte der Laserfrequenzseparation (LSF = 40 GHz, 80 GHz und 160 GHz) berechnet. Abhängig von der GGD der ersten Faser und der anfänglichen Laserleistung reichten die optimalen Längen der ersten Faser von 180 m zu 980 m und der zweiten Faser von $7,5$ m zu $37,5$ m. Für verschiedene Werte der LFS und der Laserleistung variierten die optimalen Längen der ersten Faser zwischen 150 m und 1100 m und der zweiten Faser zwischen 7 m und 35 m. Beste Systemleistung trat für die GGD von $-15\ \mathrm{ps}^2/\mathrm{km}$ und die LFS von 80 GHz auf.

Die optimalen Längen der ersten Faser hängen nicht von der anfänglichen Laserleistung, wenn diese Leistung niedrig ist. Das hat uns zu detaillierten Studien der Impulsformation in der ersten Faser mittels des Verfahrens der Soliton Radiation Beat Analysis (SRBA) veranlasst, denn das Verständnis der Impulsformation ist entscheidend für das Kontrollieren der OFK-Generierung ihm Rahmen eines Experiments. So wurde die SRBA für drei verschiedene Typen der Anfangsbedingung (ein singulärer Impuls, ein Akhmediev-Breather und eine bichromatische tief durchmodulierte Kosinus-Welle) durchgeführt. Dabei wurde die GGD von $-15\ \mathrm{ps}^2/\mathrm{km}$ für die erste Faser und die LFS von 80 GHz gewählt. Nach dem Vergleich der Resultate haben wir realisiert, dass ein kollektiver Solitonenkristall bei niedrigen Eingangsleistungen entsteht, wenn eine bichromatische tief durchmodulierte Kosinus-Welle als Anfangsbedingung gewählt wird. Mit steigender Eingangsleistung löst sich der Solitonenkristall in einzelne freie Solitonen kontinuierlich auf. Die optimalen Längen der ersten Faser zeigen genau dann ihre Unabhängigkeit von der Eingangsleistung, solange so ein Solitonenkristall existiert.

Entsprechend den SRBA-Resultaten sollen die besten OFK im Eingangsleistungsbereich zwischen $1,0$ W und $2,0$ W entstehen.

Weitere SRBA-Studien haben gezeigt, dass die Impulsformation in der anschließenden Erbium-dotierten Verstärkerfaser stark von den Eigenschaften der Impulse in der ersten Faser abhängt. Zum Beispiel findet adiabatische Solitonen-Kompression in der zweiten Faser statt, wenn die Eingangsleistungen niedrig sind. Bei niedrigen Leistungen sind auch die Solitonenordnungen in der ersten Faser niedrig, in der zweiten Faser erfahren solche Solitonen daher keine Aufspaltung. Deswegen ist die adiabatische Kompression mit der Generierung von rauscharmen OFK verbunden. Bei höheren Eingangsleistungen weisen die optischen Impulse in der ersten Faser kompliziertere Strukturen und höhere Solitonenordnungen auf. Solche Impulse zerfallen in der zweiten Faser in mehrere Subimpulse, was zu der Degradierung des Rauschverhaltens der OFK führt. Wir erwarten die besten OFK für die Eingangsleistungen zwischen $2,0$ W und $2,8$ W für $LFS = 80$ GHz und zwischen $4,0$ W und $4,5$ W für $LFS = 160$ GHz in der zweiten verstärkenden Faser.

Die Studien des Intensitätsrauschens der optischen Impulse, die wir im Rahmen dieser Arbeit durchgeführt haben, erlauben uns die Aussagen über das Rauschverhalten der OFK. Unsere Studien haben gezeigt, dass das Intensitätsrauschen des Gesamtsystems (d.h. aller drei Fasern) mit steigender LFS nachlässt. So kann zum Beispiel das Intensitätsrauschen unter 1% für $LFS = 80$ GHz und $LFS = 160$ GHz gehalten werden, während es bis zu 10% für $LFS = 40$ GHz ansteigt. Deswegen sind höhere Laserfrequenzseparationen vorzuziehen, um rauscharme optische Frequenzkämme erzeugen zu können.

List of Publications

Journal Papers

- M. Zajnulina, J. M. Chavez Boggio, M. Böhm, A. A. Rieznik, T. Fremberg, R. Haynes, M. M. Roth: *Generation of optical frequency combs via four-wave mixing process for low- and medium-resolution astronomy.* Applied Physics B Vol. 120 Issue 1, DOI: 10.1007/s00340-015-6121-1 (2015)

- M. Zajnulina, M. Böhm, K. Blow, A. A. Rieznik, D. Giannone, R. Haynes, M. M. Roth: *Soliton Radiation Beat Analysis of Optical Pulses Generated from Two CW Lasers.* Accepted for publication with "Chaos: An Interdisciplinary Journal of Nonlinear Science", Manuscript #15408R (2015)

Conferences

- J. M. Chavez Boggio, A. A. Rieznik, M. Zajnulina, M. Böhm, D. Bodenmüller, M. Wysmolek, H. Sayinc, J. Neumann, D, Kracht, R. Haynes, M. M. Roth: *Generation of an astronomical optical frequency comb in three fibre-based nonlinear stages.* Proc. SPIE 8434, Nonlinear Optics and Applications VI, 84340Y (2012)

- M. Zajnulina, J. M. Chavez Boggio, A. A. Rieznik, R. Haynes, M. M. Roth: *Generation of Optical Frequency Combs in Fibres.* Proc. SPIE 8775, Micro-structured and Specialty Optical Fibres II, 87750C (2013)

- M. Zajnulina, J. M. Chavez Boggio, M. Böhm, A. A. Rieznik, R. Haynes, M. M. Roth: *Pulse compression in Er/Yb-doped fibres.* CLEO EUROPE/IQEC (2013)

- M. Zajnulina, M. Böhm, K. Blow, A. A. Rieznik, D. Giannone, R. Haynes, M. M. Roth: *Generation of optical frequency combs in fibres: an optical pulse analysis.* Proc. SPIE 9151, Advances in Optical and Mechanical Technologies for Telescopes and Instrumentation, 91514V (2014)

- J. M. Boggio, T. Fremberg, B. Moralejo, M. Rutowska, E. Hernandez, M. Zajnulina, A. Kelz, D. Bodenmüller, C. Sandin, M. Wysmolek, H. Sayinc, J. Nuemann, R. Haynes, M. M. Roth: *Astronomical optical frequency comb generation and test in a fiber-fed MUSE spectrograph.* Proc. SPIE 9151, Advances in Optical and Mechanical Technologies for Telescopes and Instrumentation, 915120 (2014)

Acknowledgments

I would like to thank my supervisors Prof. Martin M. Roth (Leibniz Institute for Astrophysics Potsdam (AIP)) and Prof. Arkady Pikovsky (University of Potsdam) for the scientific supervision of my PhD studies and the personal support. I am very thankful to Dr. José M. Chavez Boggio for providing me with the experimental data and to Andréz A. Rieznik for the Matlab-scripts. I want to express a very special thanks to Dr. habil. Michael Böhm for introducing me to his great technique of the Soliton Radiation Beat Analysis and many inspiring discussions about optical solitons - it is always joyful to talk to such professionals likes you, Micha!

My mother being a good parent always believed in me in times of despair. Thank you for that, Mom! My friends Alla Gildenstern, Sergej (Sergej Nikolajewitsch) Solopow, Anne Beyreuther, Jan and Julia (J & J) Schmidt, Madina (Madimba) Völker, Olga Worster, and Alex (Schatzi) Dirmeier deserve a special thanks just for being my friends, I love you, guys, you are absolutely great!

A part of my PhD studies was funded by the BMBF (Bundesministerium für Bildung und Forschung / Federal Ministry of Education and Research) (Grant 03ZAN11) which I would also like to acknowledge at this point.

Contents

1 Optical Frequency Combs in Astronomy: An Introduction

In this chapter, the reader is introduced into the general concept of optical frequency combs. Further, she or he learns how frequency combs can be deployed within the Astronomy.

1.1 Laser Optical Frequency Combs

Optical frequency combs (OFC) constitute an array of sharp equidistantly positioned spectral lines with almost equal intensities over a broad spectral range. Frequency combs were first realised as spectra of femto-second pulse trains generated in mode-locked lasers in the groups of J. L. Hall (Boulder, USA) and T. W. Hänsch (Garching, Germany) at the end of the 1990's. Both scientist were awarded with the Nobel prize for the discovery of OFC in 2005.

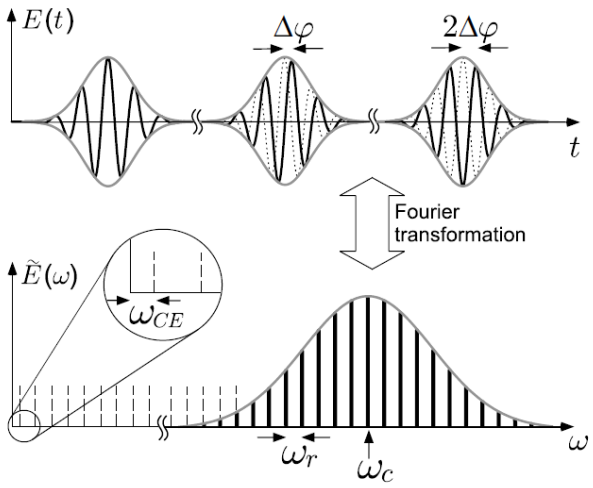

Figure 1.1: Time and frequency domain representation of a pulse train of a mode-locked laser [1]

Fig. 1.1 shows the time and frequency domain representation of a pulse train generated in a mode-locked laser. The pulse train is the result of a phase coherent superposition of many continuous-wave (CW) longitudinal laser cavity modes. In the frequency domain,

these modes constitute a series of frequency lines that form an OFC. The nth frequency line of the comb reads as:

$$\omega_n = n\omega_r + \omega_{CE}, \tag{1.1}$$

where ω_r denotes the frequency separation between the lines that is given by $\omega_r = 2\pi/T$ with T being the time between two neighbouring pulses (also called the pulse repetition time). n is the cavity mode number of some 10^6 and ω_{CE}, $0 < \omega_{CE} < \omega_r$, is the off-set frequency. The off-set frequency occurs because the carrier wave with the frequency ω_c propagates with the phase velocity (v_p) that is different from the group-velocity of the carrier-envelope (v_g) which results in a pulse-to-pulse phase shift $\Delta\phi_{CE}$:

$$\Delta\phi_{CE} = |1/v_g - 1/v_p|L_c\omega_c, \tag{1.2}$$

where L_c is the cavity round-trip length. The off-set frequency obeys the relation

$$\omega_{CE} = \Delta\phi_{CE}/T \tag{1.3}$$

and shifts the OFC as a whole from the strict harmonics of ω_r. To know absolute frequencies of an OFC, one needs to measure the frequencies ω_r and ω_{CE}. The measurement of ω_r is done by detection of the pulse repetition rate with a fast photodiode. The value of ω_{CE} is determined by measuring the beating frequency that arises if some frequency-doubled modes at the red side of the comb are superposed with modes at the blue side [1, 2].

For his studies of frequency combs, T. W. Hänsch used a Kerr-lens-mode-locked Ti:sapphire laser [3]. Also mode-locked fibre ring lasers [4], optical quantum-dot lasers [5], microring resonators [6], monolithic microresonators [7], or parametric oscillators [8] can be used for generation of OFC.

Since their inception, the OFC have induced the development of such fields of application like the frequency synthesis [9], the supercontinuum generation [10, 11], the component testing and the optical sampling in the telecommunication as well as the development of ultra-high capacity transmission systems based on optical time-devision multiplexing [12, 13, 14, 15, 16, 17]. The OFC can even be deployed for mimicking the physics of an event horizon [18].

1.2 Optical Frequency Combs for Calibration of Astronomical Spectrographs

Wavelength calibration of astronomical spectrographs is basically performed with the help of spectral emission lamps (Th/Ar, He, Ne, Hg, etc.) or absorption cells, for instance, iodine cells [19]. These techniques provide reliable and well characterised emission and absoption spectra, respectively, but have limitations in the spectral coverage. Moreover, the spectral line spacings and the line intensities are irregular [20, 21, 22].

High-resolution applications like the search for extra-solar planets via the observation of the stellar radial velocities' Doppler shifts and the measurement of the cosmological fundamental constants require an accuracy of a few cm/s in terms of radial velocity [23, 24, 25]. The resolution that typical Th/Ar lamps can provide is, however, limited to a few m/s.

Optical frequency combs constitute an ideal spectrograph calibrator since they provide a high density of stable almost equally intense spectral lines with uniform spacing [20, 26, 9, 27]. Filtered combs generated in mode-locked lasers have been proposed and already successfully tested as high-precision calibrators on such high-resolution instruments like the Ultra-High-Resolution Facility (UHRF) with resolving power of $R = \frac{\lambda}{\Delta\lambda} \approx 10^6$ at the 3.9 m Anglo-Australian Telescope [28], the High Accuracy Radial Velocity Planet Searcher (HARPS) spectrograph with $R = 115000$ at the ESO 3.6 m telescope at the La Silla observatory [29, 30], and at the 0.7 m solar German Vacuum Tower Telescope (VTT) at the Canarian Observatories [31, 32]. It was shown that - compared to the calibration lamp units - the tested broadband laser OFC improved the calibration accuracy by almost three orders of magnitude down to the cm/s−level.

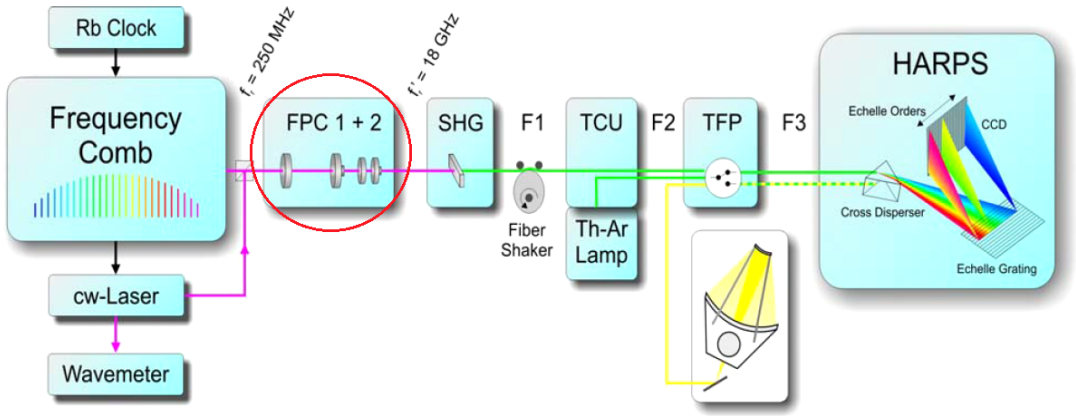

Figure 1.2: Experimental setup for the generation of OFC tested on the HARPS instrument: an Yb-fibre laser generates combs with spacing of 250 MHz, a series of Fabry-Perot cavities (FPC 1+2) filters this comb so that the resulting OFC has the line spacing of 18 GHz [30]

Mode-locked lasers produce combs with frequency line spacings of only a few tens to hundreds of MHz. Such spacings are too small to be resolvable by any astronomical spectrograph. Even for high-resolution applications, the lines of the laser-based combs need to be filtered by a set of stabilised Fabry-Perot cavities such that the line spacing is increased to $1 - 30$ GHz (Fig. 1.2.)

The instruments for the surveys of galaxy structures, the star observation, and the

Milky Way characterisation operate in the low- to medium resolution range (resolving power $R < 50000$). For instance, the spectrograph called the Multi Unit Spectroscopic Explorer (MUSE) being in development for the Very Large Telescope (VLT) has the resolving power of $R = 2000$ at $\lambda = 460$ nm and $R = 4000$ at $\lambda = 930$ nm [33]. The 4-metre Multi-Object Spectroscopic Telescope (4MOST) is a large-field multi-object spectrograph proposed for the New Technology Telescope (NTT). It consists of one spectrograph with the resolving power $R > 20000$ and several spectrographs with $R = 5000$ [34, 35]. For the OFC to be resolvable by such low- and medium-resolution instruments, the comb frequency line spacings need to be increased up to hundreds of GHz. In case of OFC produced in mode-locked lasers, this would require unfeasibly high-finesse stable Fabry-Perot cavities.

The OFC generated in monolithic microresonators due to the optical Kerr effect can be deployed specifically for the low-resolution applications. Such OFCs have frequency line spacings lying between 100 GHz and 1 THz [7, 36]. However, the microresonator-based combs suffer from the instabilities caused by the thermal effects due to the high optical-power levels inside the resonators and need to be regulary adjusted.

An all over fibre-based approach for generation of OFC in the near-IR (NIR) was proposed and experimentally realised by Dr. José M. Chavez Boggio, a member of our research group innoFSPEC at the Leibniz Institute for Astrophysics Potsdam (AIP) [37, 38, 39, 40]. This approach exploits the pulse compression in an amplifying Erbium-doped fibre with anomalous dispersion. It is comparably stable over a long period of time and has the advantage of a simple low-cost setup. Moreover, it allows to produce combs with frequency line spacings that can be tuned between a few tens of GHz and a few hundreds of GHz and so adjusted to the resolution features of a specific spectrograph. In this approach, the OFC evolves as the light from two lasers propagates through the following fibre stages: a conventional single-mode fibre, an Erbium-doped fibre, and a highly nonlinear low-dispersion fibre (Sec. 2.2).

Within this work, we[1] numerically study the proposed setup for generation of OFC in fibres. Before the reader gets to know the results of our numerical studies, she or he is introduced to the theoretical framework we are in. In Sec. 2, the general concept of the generation of OFC in optical fibres as well as the proposed fibre-based approach are presented in more detail. The mathematical model that describes the OFC formation in optical fibres is derived in Sec. 3. Different types of optical waves that exist in optical fibres and that can be deployed for an effective OFC generation are discussed in Sec. 4. The optical pulse compression techniques needed to obtain broadband OFC are presented in Sec. 5.

The results on the optical pulse formation in the first and the second fibre stage are analised in Sec. 6 and Sec. 7, respectively. In Sec. 8, the optimum fibre lengths are found

[1] In the following, "we" is used in the sense of "I"

as functions of the group-velocity dispersion parameter of the first fibre stage and of different values of the laser frequency separation. In Sec. 9, the pulse compression effectiveness in the first and the second fibre stage is studied as a function of the laser frequency separation. In Sec. 10, we present the studies on the pulse intensity noise and pulse coherence characteristics in all three fibre stages of the proposed setup.

2 Generation of Optical Frequency Combs in Optical Fibres

In Sec. 1, the reader was introduced to the general concept of optical frequency combs (OFC) and their application potential for calibration of astronomical spectrographs. The reader got to know the deployment of laser-based OFC with frequency line spacings reaching up to 30 GHz for high-resolution astronomical applications.

Specifically for low- and medium resolution applications, combs with frequency line spacings reaching from a few tens to hundreds of GHz can be generated in optical fibres starting from two continuous-wave (CW) lasers. In this case, the OFC generation is based on nonlinear cascaded four-wave mixing (FWM) processes taking place in optical fibres. Cascaded FWM-processes have been already extensively studied with the aim to generate ultra-short pulses at high repetition rates, but not with the idea to elaborate broadband OFC [13, 14, 16, 17]. In the recent past, however, some approaches targeting specifically the generation of OFC in highly nonlinear fibres were also reported [41, 42, 43, 44].

In this chapter, we introduce the reader to the general concept of the four-wave mixing in optical fibres. Moreover, we describe in detail the fibre-based approach for generation of frequency combs that was proposed within our research group innoFSPEC (AIP). We give a few experimental results proving the suitability of the proposed approach for low- and medium resolution astronomical application. The OFC was tested using a MUSE-type astronomical spectrograph [37, 38, 39, 40].

2.1 Four-Wave Mixing

The four-wave mixing (FWM) is a parametric nonlinear process relying on the third-order susceptibility $\chi^{(3)}$ of the material (cf. Sec. 3.1). During this process, photons from one or more waves are annihilated and new photons are created at different frequencies such that the net energy and momentum are conserved [45].

There are two types of this process: the non-degenerate FWM and the degenerate FWM. The non-degenerate FWM process takes place when two photons at different frequency ω_1 and ω_2 (coming from two pump beams) are annihilated with the simultaneous creation of two photons at frequencies ω_3 and ω_4 such that $\omega_1 + \omega_2 = \omega_3 + \omega_4$. The parametric gain that is responsable for the emergence of new frequency lines is given

by

$$g = \sqrt{4\gamma^2 P_1 P_2 - (\kappa/2)^2}, \tag{2.1}$$

where P_1 and P_2 denote the initial power of the pump beams with frequencies ω_1 and ω_2, γ is the so-called nonlinear parmeter of the medium, $\gamma \propto \chi^{(3)}$ (for more details see Sec. 3.2.4), and κ is the total phase mismatch given by

$$\kappa = \Delta k + \gamma(P_1 + P_2) \tag{2.2}$$

with k being the wave vector [46]. In the degenerate case, two photons at the same frequency $\omega_1 = \omega_2$ (coming from the same pump) are annihilated and two photons at different frequencies ω_3 and ω_4 are created: $2\omega_1 = \omega_3 + \omega_4$. The parametric gain for the degenerate case is the same as for the non-degenerate one [47].

The process during which the new generated waves create further photons at new frequencies is called cascaded FWM [48]. A cascade of FWM processes leads to the emergence of an OFC. The n-th tooth of such OFC is given by [44]:

$$\omega_n = n\Delta\omega + \omega_{\text{off}}, \tag{2.3}$$

where $\Delta\omega$ is the difference between two neighbouring frequency lines, ω_{off} is the offset frequency that is determined by the frequencies of the lasers involved. The offset frequency is by definition smaller than $\Delta\omega$. n is an integer of a few powers of ten (cf. Eq. 1.1).

According to Eq. 2.1, the maximum parametric gain occurs if $\kappa = 0$ or $\Delta k = -\gamma(P_1+P_2)$. In a more general case, in single-mode fibres, the phase-matching condition $\kappa = 0$ is written in the form:

$$\kappa = \Delta k_D + \Delta k_{NL} = 0, \tag{2.4}$$

where Δk_D is the mismatch that is caused by the material dispersion and the mismatch Δk_{NL} that is based on the nonlinear effects in the medium. The material contribution can be expressed as follows:

$$\Delta k_D \approx \beta_2(\omega_1 - \omega_3)^2 \left(= \beta_2(\omega_2 - \omega_4)^2\right) \tag{2.5}$$

with β_2 being the group-velocity dispersion (GVD) parameter, whereas Δk_{NL} reads as:

$$\Delta k_{NL} = \gamma(P_1 + P_2). \tag{2.6}$$

For κ to be zero, k_D and k_{NL} need to compensate each other:

$$\Delta k_D = -\Delta k_{NL}. \tag{2.7}$$

In an experimental setup, Δk_{NL} can be adjusted by changing the powers P_1 and P_2, whereas Δk_D can be effectively minimised in the anomalous, i.e. negative, dispersion region close to the zero-dispersion wavelength [43]. Further, the FWM as a parametric process is highly polarisation- and birefringence-dependent. Thus, to increase the effectiveness of the formation of a FWM-based comb, one needs to control the polarisation carefully within the experiment as well as minimise the birefringence effects [45].

2.2 Approach for Generation of Optical Frequency Combs for Astronomical Applications

Achieving the broadest possible frequency combs based on a cascade of FWM processes in optical fibres is possible in two ways. The first way is to choose fibres that are intrinsically highly nonlinear (HNLF: highly nonlinear fibres), i.e. fibres having a nonlinear parameter of $\gamma \geq 10\ \mathrm{W^{-1}km^{-1}}$ [41, 42, 43, 44]. The second way is to increase the efficiency of the nonlinear interaction in the fibre glass by injecting highly intense light into it. Intense light can be obtained, for instance, via the preceding amplification in an Erbium-doped fibre (EDFA) into the testing fibre [49, 50].

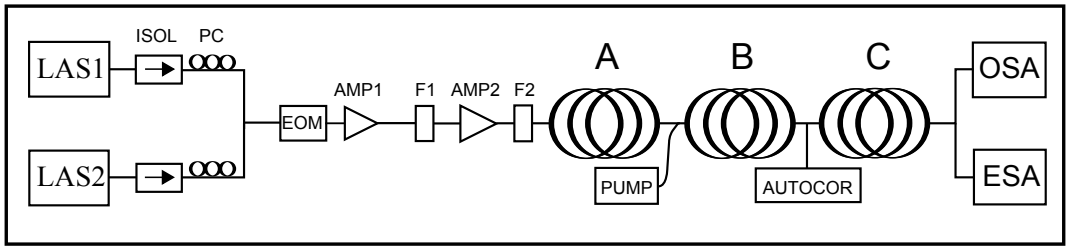

Figure 2.1: Experimental setup for the generation of OFC in fibres. ISOL: optical isolator, PC: polarisation controller, EOM: electro-optical modulator, LAS1: fixed CW laser, LAS2: tuneable CW laser, AMP1: Er-doped fibre amplifier 1, F1: optical bandpass filter 1, AMP2: Er-doped fibre amplifier 2, F2: optical bandpass filter 2, A: single-mode fibre, B: Er-doped fibre with anomalous dispersion, C: highly nonlinear low-dispersion fibre, PUMP: pump laser for fibre B, AUTOCOR: optical autocorrelator, OSA: optical spectrum analyser, ESA: electrical spectrum analyser [40]

The setup for generation of OFC in fibres proposed by our group makes use of both approaches: it contains an amplifying suitably pumped Erbium-doped fibre with anomalous, i.e. negative, dispersion as the second stage and a highly nolinear fibre as the final third stage. The first stage is a conventional single-mode fibre (Fig. 2.1) [37, 38, 39, 40].

The evolution of a frequency comb in this system is governed by the following processes: as the two initial CW-laser waves at ω_1 and ω_2 propagate through the fibre A, they generate an initial comb via a cascade of FWM processes [49, 18]. The new frequency components are phase-correlated with the original laser lines and have a frequency spacing that is equal to the initial laser frequency separation $LFS = |\omega_2 - \omega_1|/2\pi$ (Fig. 2.3A). In the time domain, a train of pre-compressed pulses with widths of a few pico-seconds arises out of the initial bichromatic deeply modulated cosine-wave [51, 52] (Fig. 2.2A). These pulses undergo a further compression as they propagate through the amplifying fibre B with anomalous dispersion [50, 53, 54, 55]: sub-100 fs pulses are

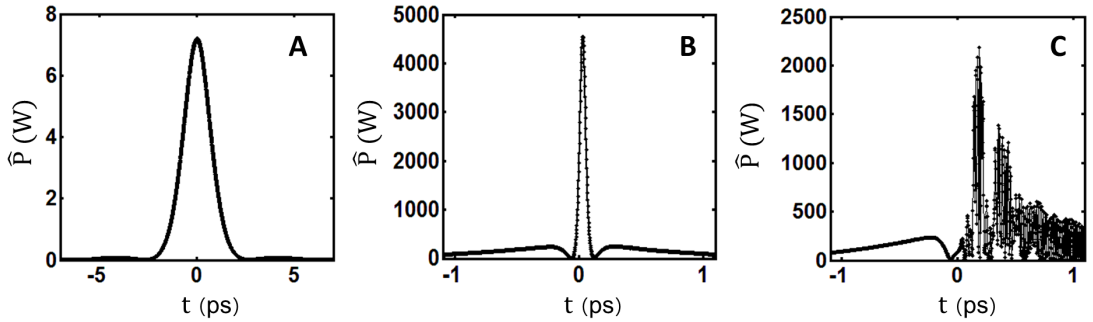

Figure 2.2: Optical pulse shapes after propagation in all three fibre stages obtained through a numerical simulation for laser frequency separation LSF = 80 GHz and initial power P_0 = 2 W

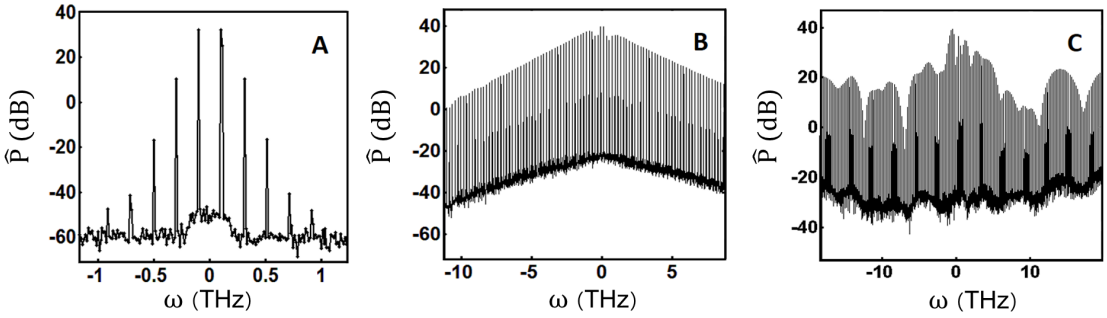

Figure 2.3: Evolution of an optical frequency comb in all three fibre stages obtained by means of numerical simulations for laser frequency separation LSF = 200 GHz and initial power P_0 = 6.5 W

generated (Fig. 2.2B). The OFC formed in fibre A is broadened after the pulses passed through fibre B (Fig. 2.3B). A low-dispersion HNLF is used as the last stage (Fig. 2.2C). In this fibre, the OFC gets strongly broadened and the intensity of the comb lines fairly equalised (Fig. 2.3C).

Fig. 2.4 shows the spectra of an optical frequency comb obtained with our experimental arrangement. The lasers that were used have equal intensity and feature relative stability of 10^{-8} over 1-hour time frame. This stability is adequate for astronomical applications in the low- and medium resolution range so that no additional stabilising techniques (like, for instance, the phase-locking to a high-finesse cavity) are required. The initial laser frequency separation is 200 GHz which is optimum for the resolution power of R = 3000. The cental wavelength is $\lambda_c = (\lambda_1 + \lambda_2)/2$ = 1552 nm. The electro-optical modulator EOM carves the initial wave that arises after the combination of both CW lasers into pulse trains with widths of 20 ns. The first amplifier AMP1 provides an average power of 12 mW. The second amplifier AMP2 raises the average

power to a value of 100 mW. The first bandpass filter F1 has a bandwidth of 100 GHz, the bandwidth of the second bandpass filter F2 is 30 GHz. A conventional single-mode fibre with total length of L^A = 350 m and dispersion and nonlinear parameters β_2^A = −21 ps^2/km and γ^A = 2 W^{-1}km^{-1}, respectively, was deployed as the first stage (A). A double-clad Er/Yb-fibre with length of L^B = 17 m was used as the second stage (B). This fibre is pumped with a power of 3 W at 940 nm. The fibre parameters are β_2^B = −15 ps^2/km, γ^B = 2.5 W^{-1}km^{-1}. Fibre C has the length of L^C = 3.5 m and parameters β_2^C = −0.5 ps^2/km, γ^B = 10 W^{-1}km^{-1} at 1550 nm.

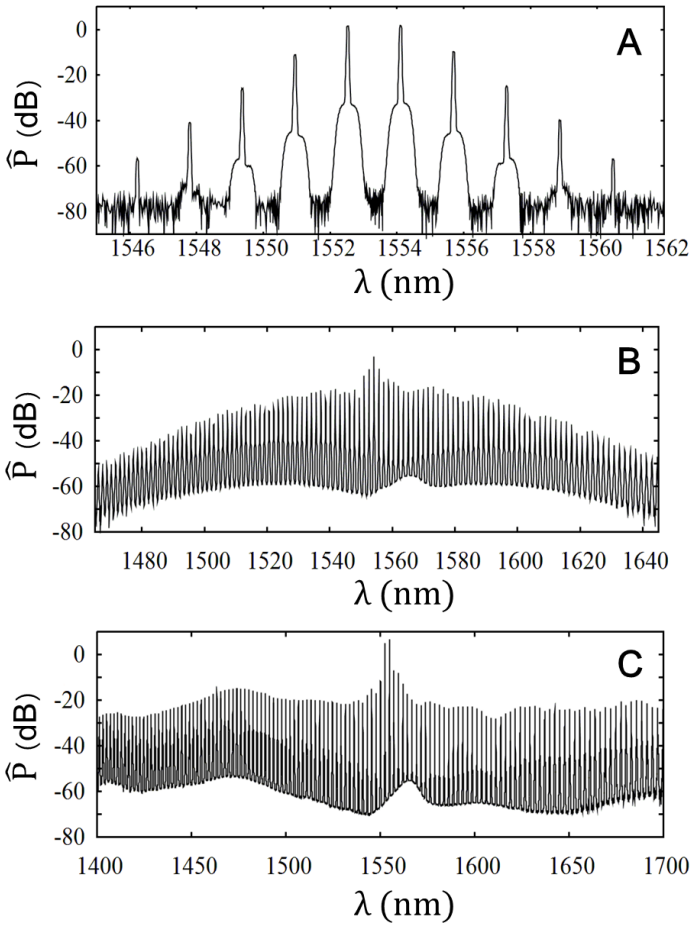

Figure 2.4: OFCs obtained after propagation through fibre stages A, B, and C with LFS = 200 GHz [40]

As shown in Fig. 2.4, the spectrum of fibre A extends from 1546.2 nm to 1560.5 nm, while the spectral bandwidth for fibre B is broadened from 1465 nm to 1645 nm. However, the OFC line intensities in fibre A and B differ in a few orders of magnitude. After propagation through fibre C, the OFC spectrum is broadened to the range between

1400 nm and 1700 nm and the line intensities are fairly equalised. The characterisation beyond 1700 nm was not possible because the operational bandwidth of spectrometer used in the experiment was exceeded [40].

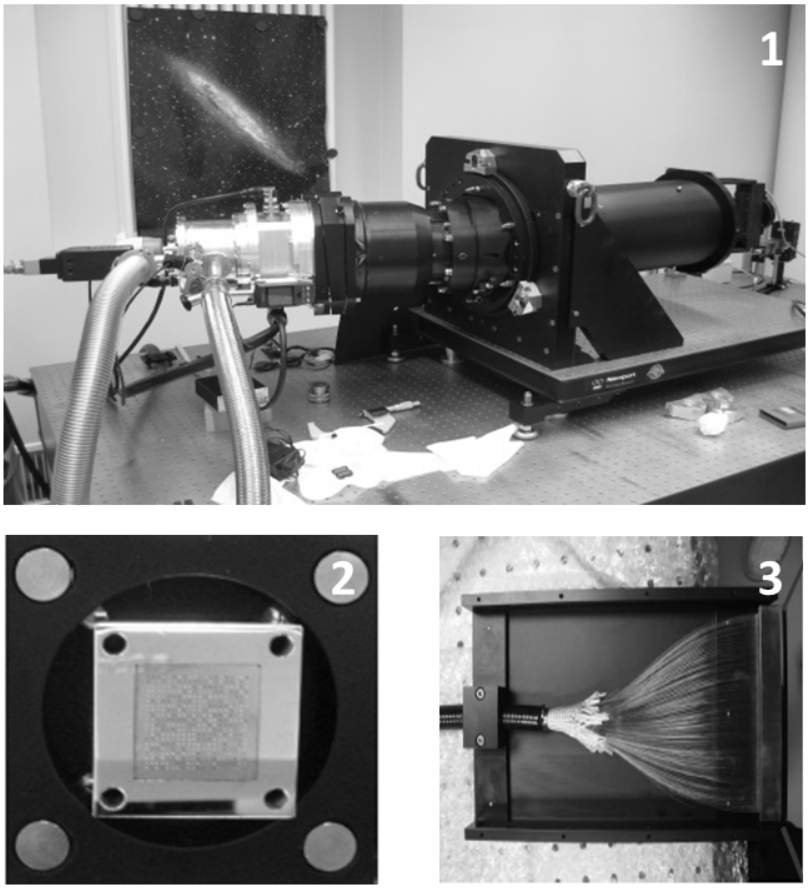

Figure 2.5: The modified MUSE-type spectrograph (1), the input (2) and the output (3) of the fibre bundle [40]

We show the suitability of the fibre-based OFC for calibration of astronomical spectrographs by testing it with a modified MUSE-type spectrograph (Fig. 2.5.1). Contrary to the original MUSE spectrograph that deploys image splicing mirrors, the modified version uses a $20 \times 20-$fibre-fed input (Fig. 2.5.2). The MUSE spectrograph itself operates in the wavelength range between 465 nm to 930 nm with a 4096×4096 CCD detector having 15 μm pixels. It exhibits the resolving power of $R = 4000$ at 930 nm. The wavelength calibration is performed using the spectral lines from Ne and Hg lamps [33]. The modified MUSE-type spectrograph exhibits the same features.

For the fibre-based OFC to be detectable by a MUSE-type spectrograph, it needs to be frequency-doubled from the NIR into the visible spectral range after fibre C. For that, an OFC centred at 1560 nm and spanning over 350 nm is focused into a BBO crystal with a thickness of 2 mm by means of a collimator and a focusing objective.

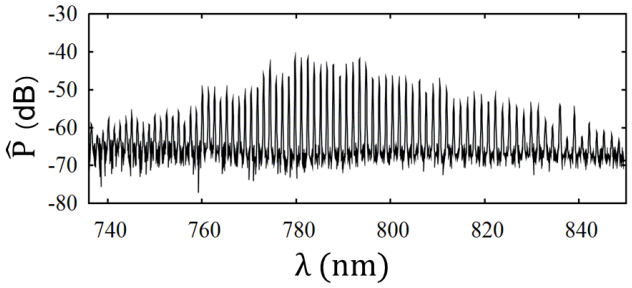

Figure 2.6: OFC obtained by means of the frequency-doubling of the output of fibre C [40]

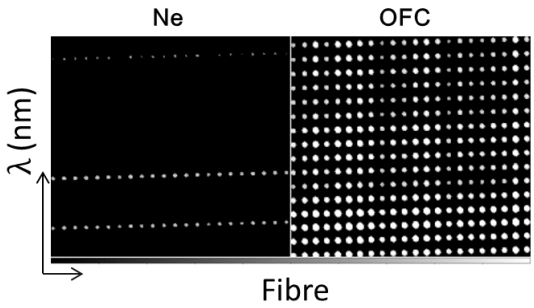

Figure 2.7: Comparison between calibration with a Ne lamp and an OFC in spectral region 1 of the MUSE-type spectrograph [40]

Fig. 2.6 shows the frequency-doubled spectrum obtained with $LFS = 708$ GHz. The OFC extends from 736 nm to 850 nm and exhibits ca. 80 narrow equidistantly positioned lines. The lines have, however, different intensities which is caused by the inequality of efficiency of the wavelength-dependent frequency-doubling process. The best performance in terms of the equality of line intensities is achieved in the spectral range between 780 nm and 800 nm [40].

Fig. 2.7 and Fig. 2.8 show the CCD images for two contiguous spectral regions (each one with 19.5 nm width) covering the range of 780 – 820 nm. The time exposure for both, the Ne and comb light, was 30 s, while different exposures were taken with a few minutes of difference between them. Each comb line was sampled by 5 pixels. While the comb spectra exhibit bright and uniformly spaced peaks, the Ne light shows only

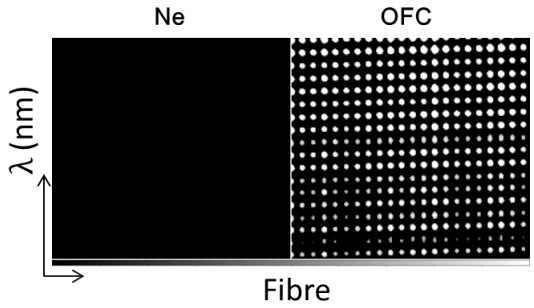

Figure 2.8: Comparison between calibration with a Ne lamp and an OFC in spectral region 2 of the MUSE-type spectrograph [40]

three lines in the spectral region 1 and none in the other region [40].

Here, we showed that the proposed fibre-based approach for generation of optical frequency combs is suitable for calibration of low- and medium resolution spectrographs and exhibits the required characteristics to outperform the Ne lamp calibration source. The 4MOST instrument would benefit from the deployment of the presented approach [34, 35].

3 Mathematical Model of Nonlinear Light Propagation in Optical Fibres

In Sec. 2.2, we presented a fibre-based approach for generation of OFC for low- and medium-resolution applications in Astronomy. Now, we focus ourselves on the derivation of the mathematical model that describes the optical pulse propagation in silica fibres according to the proposed approach. The spectra of these pulses obtained via the Fourier transform will constitute exactly the OFC we are interested in.

We begin with the description of the nonlinear optical effects that play an imporant role in silica fibres. Those effects are the optical Kerr effect, the delayed Raman effect, and the pulse self-steepening. Then, we derive the pulse-propagation equation. For that, we start with the Maxwell's equations. Having applied the well-known slowly varying envelope approximation (SVEA), we end up with a Generalised Nonlinear Schrödinger Equation (GNLS) in the co-moving frame that contains

- the group-velocity and the higher-order dispersion
- the nonlinear interaction terms (the optical Kerr effect, the Raman effect, and the pulse self-steepening)
- the linear fibre losses
- the Erbium gain for the second fibre stage of the proposed setup.

This equation (Eq. 3.46) will be used in the further course of our studies. Here, we also give a suitable initial condition equation (Eq. 3.47) that describes the radiation of two CW lasers of the proposed setup. After the pulse-propagation equation is derived, we briefly discuss the Fourth-Order Runge-Kutta Method in the Interaction Picture (RK4IP) that is used for the numerical integration of Eq. 3.46 and Eq. 3.47.

3.1 Nonlinear Optical Effects in Fibres

A great part of optical fibres available on the market is fabricated out of silica glass. If an optical plane wave with the electric field component $\mathbf{E}(z,t) = \mathbf{E}_0 e^{i(\omega t - kz)}$ propagates through this dielectric medium, it induces a charge displacement that yields formation of electric dipoles $\mathbf{p}(\mathbf{E})$. The sum of these dipoles constitutes the dielectric polarisation field:

$$\mathbf{P}(\mathbf{E}) = \frac{1}{V} \sum_i \mathbf{p}_i(\mathbf{E}), \tag{3.1}$$

where V denotes the volume element. The dependence of the time-dependent dielectric polarisation $\mathbf{P}(t)$ on the electric field $\mathbf{E}(t)$ can be expressed by means of a Taylor series expansion [56]:

$$\mathbf{P}(\mathbf{E}) = \epsilon_0 \left(\chi^{(1)}\mathbf{E} + \chi^{(2)}|\mathbf{E}|^2 + \chi^{(3)}|\mathbf{E}|^2\mathbf{E} + \dots \right), \tag{3.2}$$

where $\chi^{(n)}$ is the n-th order component of the electric susceptibility of the medium. The linear term in Eq. 3.2 describes the polarisation induced by the electric dipoles, the nonlinear contributions denote the formation of the multipoles. Generally holds that $\chi^{(n)}\mathbf{E}^{(n)} \gg \chi^{(n+1)}\mathbf{E}^{(n+1)}$, therefore the higher-order terms can be dropped if the intensity of the electric field is not too high. In this part, we are more interested in the physical meaning of the terms rather than in their time dependence, therefore the components of $\chi^{(n)}$ are assumed to be time-independent. Later on, we will take a closer look on the time dependence of the susceptibility components.

The first-order susceptibility in Eq. 3.2, i.e. $\hat{\chi}^{(1)}$, describes the linear dispersion of light inside the optical fibres. The third-order susceptibility $\hat{\chi}^{(3)}$ gives rise to the nonlinear effects that play an important role in silica materials, namely the optical Kerr effect and the Raman effect [45, 46]. The second-order susceptibility $\hat{\chi}^{(2)}$ is present only in dielectric media without inversion symmetry. Due to the symmetry properties of silica, the effects presented by $\hat{\chi}^{(2)}$ are not existent in optical fibres [57, 58]. Therefore, the second-order term drops out and the resulting polarisation reduces to the following form:

$$\mathbf{P}(\mathbf{E}) = \epsilon_0 \left(\chi^{(1)}\mathbf{E} + \chi^{(3)}|\mathbf{E}|^2\mathbf{E} \right). \tag{3.3}$$

3.1.1 Optical Kerr Effect

The optical Kerr effect is a phenomenon associated with the change of the medium refractive index due to the displacement of the electrons inside the material when an electric field $\mathbf{E}(z,t)$ propagates through it. The self-phase modulation is a nonlinear optical effect that is induced by the change of the refractive index due to the optical Kerr effect.

The refractive index depends on the dielectric suscebility via $n = \sqrt{1+\chi}$. Accordingly, the expression for polarisation presented in Eq. 3.3 implies the following form of the refractive index:

$$n(I) = n_0 + n_2 I(t), \tag{3.4}$$

where n_0 is the linear refractive index, whereas n_2 is the second-order nonlinear refractive index, $I(t)$ denotes the time-dependent light intensity, i.e. $I(t) = \frac{|\mathbf{E}(t)|^2}{A_{\text{eff}}}$ with A_{eff} being the effective modal area. Note that both, n_0 and n_2, are frequency-dependent.

To understand the effect of the self-phase modulation, consider the phase of the electric field $\mathbf{E}(t)$ propagating in $z-$direction in a medium that is subjected to the Kerr

effect:

$$\phi := \omega t - kz = \omega t - \frac{\omega n}{c} z = \omega \left(t - \frac{n_0}{c} z \right) - BI(t), \tag{3.5}$$

where $B := \frac{n_2 \omega}{c} z$ is proportional to the nonlinear part n_2 of the refractive index. The time derivative of the phase will give us the actual wave frequency:

$$\omega = \frac{d\phi}{dt} = \omega_0 - B \frac{dI}{dt}.$$

Obviously, for the increasing intensity of a light pulse that propagates through the medium, i.e. for $\frac{dI}{dt} > 0$, the effective frequency ω is smaller than the initial frequency ω_0. On the contrary, for $\frac{dI}{dt} < 0$, the value of the initial frequency increases. In other words, the spectral profile of the light pulse broadens due to the appearance of new frequency components. This broadening is symmetric for pulses that have symmetric intensity profiles [56].

The self-phase modulation appears if a monochromatic wave propagates through the material. If a polychromatic wave propagates through a nonlinear medium, the processes of cross-phase modulation and the four-wave mixing (Sec. 2.1) can take place due to the optical Kerr effect (Eq. 3.4) [45].

3.1.2 Raman effect

The displacement of the electrons inside the material due an electric field $\mathbf{E}(z, t)$ (the optical Kerr effect) occurs almost instantaneously. The vibration of silica molecules induced by $\mathbf{E}(z, t)$ also known as the (delayed) Raman effect is, however, time-dependent since it involves the response of more heavy nuclei. According to that, the response function $R(t)$ that includes both, the electronic and the nuclear contributions, can be written as [45, 46]:

$$R(t) = (1 - f_R)\delta(t) + f_R h_R(t), \tag{3.6}$$

where the first term describes exactly the Kerr effect and the second one the delayed Raman effect. In this equation, $f_R = 0.245$ is the fractional contribution of the Raman response to the nonlinear polarisation and $h_R(t)$ is the Raman response function. The Fourier transform of $h_R(t)$ is connected with the Raman-gain spectrum via the third-order susceptibility:

$$g_R(\Delta\omega) = \frac{f_R \omega_0}{cn(\omega_0)} \chi^{(3)} \operatorname{Im}\left(\tilde{h}_R(\Delta\omega) \right) \tag{3.7}$$

where $\Delta\omega = \omega - \omega_0$ [45].

Due to the amorphous nature of silica glass, it is difficult to calculate the precise form of the Raman response function $h_R(t)$. The spectrum of the Raman gain can be used to find an analytical approximation of $h_R(t)$. One of such possible approximations is the following one:

$$h_R(t) = (1 - f_b)h_a(t) + f_b h_b(t), \tag{3.8}$$

with the functions

$$h_a(t) = \frac{\tau_1^2 + \tau_2^2}{\tau_1 \tau_2^2} \exp\left(-\frac{t}{\tau_2}\right) \sin\left(\frac{t}{\tau_1}\right), \tag{3.9}$$

$$h_b(t) = \left(\frac{2\tau_b - t}{\tau_b^2}\right) \exp\left(-\frac{t}{\tau_b}\right), \tag{3.10}$$

where $\tau_1 = 12.2$ fs and $\tau_2 = 32$ fs are the characteristic times of the Raman response and $f_b = 0.21$ represents the vibrational instability of silica with $\tau_b \approx 96$ fs [46, 54, 37, 38, 39]. We will use this form of the Raman response function in the further course of our studies.

3.1.3 Pulse Self-Steepening

The effect of the self-steepening plays an important role for optical pulses with widths below 1 ps and has its origin in the intensity-dependence of the refractive index due to the Kerr effect (Eq. 3.4). To get an idea about the self-steepening, let us consider the pulse group velocity

$$v_g = \frac{c}{n} \tag{3.11}$$

with c being the speed of light in vacuum. If we put Eq. 3.4 into the definition of the group velocity, we see that the centre of the pulse moves at lower speed than the wings:

$$v_g(t) = \frac{c}{n_0 + n_2 I(t)}. \tag{3.12}$$

This yields that an initially symmetric pulse becomes asymmetric with its peak shift-

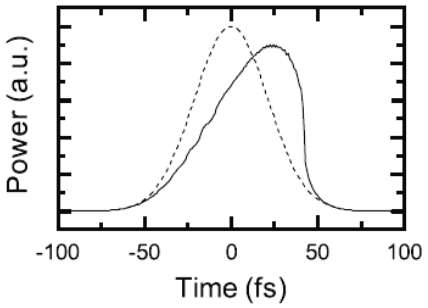

Figure 3.1: Demontration of the effect of self-steepening: a pulse at the input (dashed line) vs. the same pulse at the output (solid line) of a nonlinear Kerr medium [59]

ing towards the trailing edge, whereas the latter one becomes steeper and steeper with increasing propagation distance (Fig. 3.1). The growing pulse asymmetry yields increasing of the asymmetry of the spectrum: the steeper trailing edge of the pulse implies spectral broadening on the blue side of the spectrum. Contrary to acoustic or water

waves, the pulse shock in optical systems is prevented if GVD is present: the GVD dissipates the shock by broadening the spectrum of the steepening trailing edge [45].

3.2 The Wave Equation

3.2.1 General Form of the Wave Equation

The propagation of light in fibres is governed by the well-known Maxwell's equations [45, 60, 61]:

$$\begin{aligned} \mathrm{div}\mathbf{D} &= \rho \\ \mathrm{div}\mathbf{B} &= 0 \\ \mathrm{curl}\mathbf{E} &= -\partial_t \mathbf{B} \\ \mathrm{curl}\mathbf{H} &= \mathbf{j} + \partial_t \mathbf{D}, \end{aligned}$$

where $\mathbf{E}$ and $\mathbf{B}$ denote the electric field and the magnetic field, respectively, whereas $\mathbf{D}$ and $\mathbf{H}$ stand fot the electric displacement field and the magnetising field. Further, ρ denotes the charge density and $\mathbf{j}$ the current density. In optical fibres, free charges are absent. Thus, ρ and $\mathbf{j}$ can be set to 0.

Additionally to the Maxwell's equations, we also consider the material equations. They describe how different materials react to the applied electric and magnetic fields:

$$\begin{aligned} \mathbf{B} &= \mu_0(\mathbf{H} + \mathbf{M}) \\ \mathbf{D} &= \epsilon_0 \mathbf{E} + \mathbf{P}. \end{aligned}$$

In the material equations, $\mathbf{P}$ stands for the polarisation and $\mathbf{M}$ for the magnetisation of the medium. Silica glass can be considered as a nonmagnetic medium. So, the magnetisation $\mathbf{M}$ can be set to 0. All remained quantities, i.e. $\mathbf{D}$, $\mathbf{E}$, $\mathbf{B}$, and $\mathbf{H}$ are functions of the space $\mathbf{r}$ and the time t.

To obtain the wave equation that describes the propagation of the electric field $\mathbf{E}$ inside a silica fibre, we apply the curl differential operator on the Maxwell equation $\mathrm{curl}\mathbf{E} = -\partial_t \mathbf{B}$:

$$\begin{aligned} \mathrm{curl}(\mathrm{curl}\mathbf{E}) &= \underbrace{\mathrm{grad}(\mathrm{div}\mathbf{E})}_{=0} - \Delta\mathbf{E} = \\ &= -\mathrm{curl}(\partial_t \mathbf{B}) = \ldots = -\mu_0 \partial_{tt} \mathbf{D}, \end{aligned}$$

and obtain the general form of the sought wave equation:

$$\Delta\mathbf{E} = \mu_0 \partial_{tt}\mathbf{D} = \frac{1}{c^2}\partial_{tt}\mathbf{E} + \mu_0 \partial_{tt}\mathbf{P} = \frac{1}{c^2}\partial_{tt}\mathbf{E} + \frac{1}{\epsilon_0 c^2}\partial_{tt}\mathbf{P} \tag{3.13}$$

or also

$$\Delta\mathbf{E} - \frac{1}{c^2}\partial_{tt}\mathbf{E} = \frac{1}{\epsilon_0 c^2}\partial_{tt}\mathbf{P}, \tag{3.14}$$

where $c = \frac{1}{\sqrt{\epsilon_0\mu_0}}$ denotes the speed of light in vacuum.

3.2.2 Linear and Nonlinear Polarisation

As already mentioned, if an electric field of the form $\mathbf{E} = \mathbf{E}_0 e^{i(\beta z - \omega t)}$ propagates through a dielectric medium, it induces a displacement of charge carriers in atoms and molucules which leads to the formation of electric multipoles $\mathbf{p}(\mathbf{E})$. The sum of all electric multipoles per a unit volume V is the macroscopic dielectric polarisation $\mathbf{P}(\mathbf{E})$ (Eq. 3.1).

In silica, the dependence of the jth component of the dielectric polarisation on the applied electric field can be written as follows [56, 61, 62]:

$$\begin{aligned} P_j(\mathbf{r},t) &= \epsilon_0\Big(\int_{-\infty}^{\tau}\hat{\chi}^{(1)}_{jk}(t-\tau_1)E_k(\mathbf{r},\tau_1)d\tau_1 + \\ &+ \int_{-\infty}^{\tau}\hat{\chi}^{(3)}_{jklm}(t-\tau_1,t-\tau_2,t-\tau_3)E_k(\mathbf{r},\tau_1)E_l(\mathbf{r},\tau_2)E_m(\mathbf{r},\tau_3)d\tau_1 d\tau_2 d\tau_3\Big), \end{aligned} \tag{3.15}$$

where we used the Einstein notation that implies summation in case of the index duplication. The tensor $\hat{\chi}^{(n)}$ denotes the n-th order of the electric susceptibility (cf. Eq. 3.3).

The assumption of an instantaneous nonlinear response of the medium will help us to simplify Eq. 3.15. With this assumption, the tensor $\hat{\chi}^{(3)}$ can be written as a product of delta distributions:

$$\hat{\chi}^{(3)}_{jklm}(t-\tau_1,t-\tau_2,t-\tau_3) \quad =: \quad \chi^{(3)}\delta(t-\tau_1)\delta(t-\tau_2)\delta(t-\tau_3), \tag{3.16}$$

where $\chi^{(3)}$ is a scalar. The instantaneous response neglects the contribution of the molecular vibrations to $\chi^{(3)}$, it only takes the electronic (Kerr) response into account that is generally much faster that the response of the nuclei. In silica fibres, the vibrational or Raman response occurs over a time scale of $60 - 70$ fs. Therefore, Eq. 3.16 is valid only for optical pulses with widths > 1 ps [45]. A more precise consideration of the Raman effect and its inclusion into the wave equation will be done later in this section.

According to previous considerations, the polarisation can be split into a linear and a nonlinear part:

$$P_j(\mathbf{r},t) = \epsilon_0\left(\int_{-\infty}^{\tau}\hat{\chi}^{(1)}_{jk}(t-\tau_1)E_k(\mathbf{r},\tau_1)d\tau_1 + \chi^{(3)}(\mathbf{E},\mathbf{E})E_j\right) =: P_{j/\mathrm{LN}} + P_{j/\mathrm{NL}}, \tag{3.17}$$

where $(\mathbf{E},\mathbf{E})$ denotes the scalar product of the electric field with itself.

3.2.3 Slowly Varying Envelope Approximation

Eq. 3.14 is a partial differential equation of the second order. It can be simplified using the so called slowly varying envelope approximation (SVEA) that assumes the optical field to be quasi-monochromatic with the central frequency ω_0 of the carrier wave and the spectral width $\Delta\omega$ such that $\Delta\omega/\omega_0 \ll 1$. This assumption is valid for optical pulses as short as 0.01 ps and is applicable in our case [45].

Within the SVEA, the electric field can be written as:

$$\mathbf{E}(\mathbf{r},t) = \mathbf{x}E(\mathbf{r},t)e^{i(\beta_0 z-\omega_0 t)}, \tag{3.18}$$

the linear and the nonlinear polarisation as:

$$\mathbf{P}(\mathbf{r},t) = \mathbf{x}P(\mathbf{r},t)e^{i(\beta_0 z-\omega_0 t)} = \mathbf{x}\left(P_{\mathrm{LN}}(\mathbf{r},t) + P_{\mathrm{NL}}(\mathbf{r},t)\right)e^{i(\beta_0 z-\omega_0 t)} \tag{3.19}$$

where ω_0 and β_0 are the frequency and the propagation constant of the carrier wave, $\mathbf{x}$ is the polarisation unit vector, $E(\mathbf{r},t)$, $P_{\mathrm{LN}}(\mathbf{r},t)$, and $P_{\mathrm{NL}}(\mathbf{r},t)$ are the slowly varying envelopes of the electric field and polarisation. If we assume the maintainance of the polarisation along the fibre length, we can drop the polarisation vector from the consideration and treat the fields as scalars. This assumption is not exact, unless polarisation-maintaining fibres are used, because real fibres can not sustain perfect cylindrical shapes, random variations of the shape are always present. This yields a random change of the polarisation state. In practical terms, this effect will reduce the efficiency of the nonlinear effects. The latter ones exhibit the highest level of efficiency when the waves that propagate through an optical fibre have parallel and linear polarisation. However, the assumption of the polarisation maintainance does not only simplify the derivation of the mathematical model of the light propagation in optical fibres, but also works well in practice [45].

The envelopes $E(\mathbf{r},t)$ and $P(\mathbf{r},t)$ can be written as:

$$E(\mathbf{r},t) =: F(x,y)A(z,t), \tag{3.20}$$

$$P(\mathbf{r},t) =: F(x,y)\overline{P}(z,t), \tag{3.21}$$

where $F(x,y)$ denotes the fields' profiles in the $x-y-$plane transversal to the propagation direction z. It describes the mode distribution in the fibre and is generally given in the form of a Bessel function. Here, we consider the propagation of light through single-mode fibres. In this case, the single fundamental mode can be approximated by a Gaussian:

$$F(x,y) \propto e^{-\frac{x^2+y^2}{w^2}} \tag{3.22}$$

with the width parameter w that approximately equals the fibre core radius for standard telecommunication fibres [45]. The evolution of the field along the propagation direction z is given by the envelope functions $A(z,t)$ and $\overline{P}(z,t)$. Those are the functions, we are mainly interested in. Therefore, we will drop the mode distribution from our

consideration and focus ourselves on $A(z,t)$ and $\overline{P}(z,t)$, instead.

Within the SVEA, the envelope functions $A(z,t)$ and $\overline{P}(z,t)$ are assumed to have a slow spatio-temporal dependence. Quantitatively, this means [61]:

$$|\partial_{zz}A(z,t)| \ll \beta_0|\partial_z A(z,t)| \ll \beta_0^2|A(z,t)|, \qquad |\partial_{tt}A(z,t)| \ll \omega_0|\partial_t A(z,t)| \ll \omega_0^2|A(z,t)| \quad (3.23)$$

and similarly for $P(z,t)$:

$$|\partial_{zz}\overline{P}(z,t)| \ll \beta_0|\partial_z \overline{P}(z,t)| \ll \beta_0^2|\overline{P}(z,t)|, \qquad |\partial_{tt}\overline{P}(z,t)| \ll \omega_0|\partial_t \overline{P}(z,t)| \ll \omega_0^2|\overline{P}(z,t)|. \quad (3.24)$$

Appliyng the SVEA to Eq. 3.14, we obtain:

$$\begin{aligned}
\Delta\mathbf{E} \quad - \quad & \frac{1}{c^2}\partial_{tt}\mathbf{E} = \left(\partial_{zz} - \frac{1}{c^2}\partial_{tt}\right)A(z,t)e^{i(\beta_0 z-\omega_0 t)} = \\
= \quad & \left(\partial_{zz}A + 2i\beta_0\partial_z A - \beta_0^2 A\right)e^{i(\beta_0 z-\omega_0 t)} - \left(\frac{1}{c^2}\partial_{tt}A - 2i\frac{\omega_0}{c^2}\partial_t A - \frac{\omega_0^2}{c^2}A\right)e^{i(\beta_0 z-\omega_0 t)} \approx \\
\approx \quad & 2i\beta_0\left(\partial_z A + \frac{1}{c}\partial_t A\right)e^{i(\beta_0 z-\omega_0 t)} \qquad (3.25)
\end{aligned}$$

and

$$\begin{aligned}
\partial_{tt}\mathbf{P} \quad = \quad & \partial_{tt}\overline{P}(z,t)e^{i(\beta_0 z-\omega_0 t)} = \left(\partial_{tt}\overline{P} - 2i\omega_0\partial_t\overline{P} - \omega_0^2\overline{P}\right)e^{i(\beta_0 z-\omega_0 t)} \approx \\
\approx \quad & -\omega_0^2\overline{P}e^{i(\beta_0 z-\omega_0 t)}. \qquad (3.26)
\end{aligned}$$

Combining all terms, we get a more convenient form of the wave equation:

$$\left(\partial_z + \frac{1}{c}\partial_t\right)A(z,t) = i\frac{\beta_0}{2\epsilon_0}\overline{P}(z,t). \quad (3.27)$$

This wave equation is a first-order partial differential equation. Further, the fields' envelopes A and $\overline{P}$ are functions of only two variables, the propagation distance z and the time t.

3.2.4 General Pulse-Propagation Equation

Now, after we obtained the wave equation for the slowly variyng fields' envelopes (Eq. 3.27), we proceed with the derivation of a more realistic wave equation. We will do it in the frequency domain which will allow us to apply a few more assumptions for the simplification of the derivation process. So, consider the following Fourier transforms:

$$A(z,t) = \int_{-\infty}^{+\infty}\tilde{A}(z,\omega-\omega_0)e^{i(\omega_0-\omega)t}d(\omega-\omega_0), \quad (3.28)$$

$$\overline{P}(z,t) = \int_{-\infty}^{+\infty}\tilde{P}(z,\omega-\omega_0)e^{i(\omega_0-\omega)t}d(\omega-\omega_0), \quad (3.29)$$

where ω_0 denotes the frequency of the envelope's carrier wave and ω is the frequency of any other component of an optical pulse.

Applying the Fourier transforms to Eq. 3.27 and using the form of the polarisation that we elaborated in Eq. 3.17, we get the wave equation in the frequency domain:

$$\partial_z \tilde{A} + i(\beta(\omega) - \beta_0)\tilde{A} = \overline{\chi}^{(1)}(\omega)\tilde{A} + i\frac{\beta_0}{2}\chi^{(3)}|A|^2\tilde{A} \tag{3.30}$$

with the rewritten linear dielectric susceptibility $\overline{\chi}^{(1)} := i\frac{\beta_0}{2}\chi^{(1)}$. It is closely connected with the effective refractive index of the medium via

$$\overline{\chi}^{(1)}(\omega) = n_{\text{eff}}^2(\omega) - 1, \tag{3.31}$$

where n_{eff} is defined as

$$n_{\text{eff}}(\omega) = \beta\frac{c}{\omega}. \tag{3.32}$$

For a single-mode propagation, the frequency-dependent effective refractive index can be assumed to have a similar value as the refractive index at the frequency of the carrier wave, i.e. $n_{\text{eff}}(\omega) \approx n_{\text{eff}}(\omega_0)$. In this case, $n_{\text{eff}}(\omega_0)$ is a constant. This assumption will make the backward Fourier transform easier.

A precise expression for the propagation constant $\beta(\omega)$ is rarely known. Thus, it is useful to perform a Taylor expansion of $\beta(\omega)$ around the carrier frequency ω_0 [45]:

$$\beta(\omega) = \beta_0 + (\omega - \omega_0)\beta_1 + \frac{1}{2}(\omega - \omega_0)^2\beta_2 + \frac{1}{6}(\omega - \omega_0)^3\beta_3 + \dots, \tag{3.33}$$

where the expansion parameters are defined as

$$\beta_k = \left(\frac{d^k\beta}{d\omega^k}\right)_{\omega=\omega_0} \qquad (k = 1, 2, ...) \tag{3.34}$$

and β_0 is given by $\beta_0 = \frac{n(\omega_0)}{\omega_0}c$ with n_0 being the linear refractive index at the carrier frequency ω_0. Using the β_k coefficients, we obtain:

$$\partial_z \tilde{A} + i\sum_{k=1}^{K}\frac{\beta_k}{k!}(\omega - \omega_0)^k\tilde{A} = \overline{\chi}^{(1)}\tilde{A} + i\frac{\beta_0}{2}\chi^{(3)}|A|^2\tilde{A} \tag{3.35}$$

Note that the parameters β_m are just constants and denote the order of the dispersion, whereas the terms $(\omega - \omega_0)^m$ result in the time derivatives $i^m\frac{\partial^m}{\partial t^m}$ if Fourier-transformed back into the time domain.

Performing the backward Fourier transform, we obtain the following equation for the pulse propagation:

$$\frac{\partial A}{\partial z} - i\sum_{k=1}^{K} i^k\frac{\beta_k}{k!}\frac{\partial^k A}{\partial t^k} = (n_{\text{eff}}^2(\omega_0) - 1)A + i\gamma|A|^2A, \tag{3.36}$$

where the expression that contains the third-order susceptibility, i.e. $\frac{\beta_0}{2}\chi^{(3)}$, was substituted by the nonlinear parameter γ defined as follows:

$$\gamma = \frac{\omega_0 n_2}{c A_{\text{eff}}} \tag{3.37}$$

with n_2 being the nonlinear refractive index (cf. Eq. 3.4) and A_{eff} the effective mode area,

$$A_{\text{eff}} = \frac{\left(\int\int |F(x,y)|^2 dxdy\right)^2}{\int\int |F(x,y)|^4 dxdy}. \tag{3.38}$$

According to the definition of the nonlinear parameter γ, the term $\gamma|A|^2A$ on the right-hand side of Eq. 3.36 represents the optical Kerr effect.

A further simplification of Eq. 3.36 can be made if we "sit down" on the top of a pulse and "travel" with it along the fibre. In this case, the formulation of the pulse-propagation equation can be done in the co-moving frame. In the co-moving frame, the linear dispersion is not noticeable. That means that the linear term on the equation's right-hand side can be dropped, whereas the summation on the left-hand side will start up with $k = 2$:

$$\frac{\partial A}{\partial z} - i\sum_{k=2}^{K} i^k \frac{\beta_k}{k!}\frac{\partial^k A}{\partial t^k} = i\gamma|A|^2A. \tag{3.39}$$

Note that Eq. 3.39 reduces to the form of a Nonlinear Schrödinger Equation (NLS) if the sum goes only up to $K = 2$, i.e. if only β_2, also often referred to as the group-velocity dispersion (GVD) parameter, is kept:

$$\frac{\partial A}{\partial z} + i\frac{\beta_2}{2}\frac{\partial^2 A}{\partial t^2} = i\gamma|A|^2A. \tag{3.40}$$

If other parameters like β_3 called third-order dispersion (TOD) parameter and β_k ($k \geq 4$) called higher-order dispersion parameters are taken into acount, Eq. 3.39 is referred to as the Generalised Nonlinear Schrödinger Equation (GNLS).

The GNLS in the form as presented in Eq. 3.39 describes very well the dynamics of optical pulses in fibres if they have widths that are larger than 1 ps. The assumption of the instantaneous nonlinear response (Eq. 3.16) works quite well in this case. The spectra of ultra-short pulses with widths < 1 ps are, however, broad enough (> 1000 GHz) to be subjected to the intra-pulse Raman scattering: the Raman gain amplifies the low-frequency components at an expense of the high-frequency componets of the pulse spectrum. As a result, the pulse spectrum gets shifted towards the low-frequency (red) side [45]. According to that, the third-order susceptibility needs to be time-dependent in case of ultra-short pulses so that the intra-pulse Raman scattering can be properly included into the model. The time-dependency of $\hat{\chi}^{(3)}_{jklm}$ can be expressed via the response

function (Eq. 3.6):

$$\hat{\chi}^{(3)}_{jklm}(t_1,t_2,t_3) = \chi^{(3)}\left(R(t_1)\delta(t_2)\delta(t_3-t_1) + R(t_2)\delta(t_3)\delta(t_1-t_2) + R(t_3)\delta(t_1)\delta(t_2-t_3)\right). \tag{3.41}$$

The jth component of the nonlinear polarisation reads then as

$$P_{j/NL}(\mathbf{r},t) = \epsilon_0\chi^{(3)}E_j(\mathbf{r},t)\int_{-\infty}^{t} R(t-\tau)|\mathbf{E}(\mathbf{r},\tau)|^2 d\tau. \tag{3.42}$$

The fast change of the intensity profile of ultra-short pulses induces a fast change of the intensity-dependent refractive index (Eq. 3.4). Taking this into account, we can write down the pulse-propagation equation for the slowly varying envelope $A(z,t)$ [45, 54, 37, 38, 39]:

$$\frac{\partial A}{\partial z} = i\sum_{k=2}^{K}\frac{i^k}{k!}\beta_k\frac{\partial^k A}{\partial t^k} + i\gamma\left(1+\frac{i}{\omega_0}\frac{\partial}{\partial t}\right)A\int_{-\infty}^{\infty} R(t')|A(z,t-t')|^2 dt'. \tag{3.43}$$

Note that the function $R(t)$ (Eq. 3.6) contains not only the response of the nuclei that causes the Raman effect, but also the almost instantaneous electronic response that induces the optical Kerr effect. According to this, the time derivative in the last term on the right-hand side of Eq. 3.43 will imply not only the fast process of the intra-pulse Raman scattering, but also the phenomenon of the pulse self-steepening (cf. Sec. 3.1.3).

3.2.5 Final Pulse-Propagation Equation

As the light propagates through a fibre, it experiences losses due to the absorption of the medium:

$$\frac{P(z,t)}{P(z=0,t)} = e^{-\alpha z} \tag{3.44}$$

where $P(z,t) = |A(z,t)|^2$ is the optical power and α is the absorption coefficient [56]. The absorption coefficient is wavelength dependent. In silica fibres, the minimum of optical losses (ca. 0.2 dB/km) is exhibited in the wavelength region near 1.55 μm [46]. Mathematically, the fibre losses are accounted for by the adding of a linear term to Eq. 3.43 [45]:

$$\frac{\partial A}{\partial z} = i\sum_{k=2}^{K}\frac{i^k}{k!}\beta_k\frac{\partial^k A}{\partial t^k} + i\gamma\left(1+\frac{i}{\omega_0}\frac{\partial}{\partial t}\right)A\int_{-\infty}^{\infty} R(t')|A(z,t-t')|^2 dt' - \frac{\alpha}{2}A. \tag{3.45}$$

As presented in Sec. 2.2, the second fibre stage of the proposed setup for generation of OFC is an amplifying suitably pumped Er-doped fibre. Similar to the optical losses, the optical amplification is mathematically treated as an additional term in the wave equation:

$$\frac{\partial A}{\partial z} = i\sum_{k=2}^{K}\frac{i^k}{k!}\beta_k\frac{\partial^k A}{\partial t^k} + i\gamma\left(1+\frac{i}{\omega_0}\frac{\partial}{\partial t}\right)A\int_{-\infty}^{\infty} R(t')|A(z,t-t')|^2 dt' - \frac{\alpha}{2}A + \tilde{\mathcal{F}}\left(g(\omega)\widetilde{A}(z,\omega)\right), \tag{3.46}$$

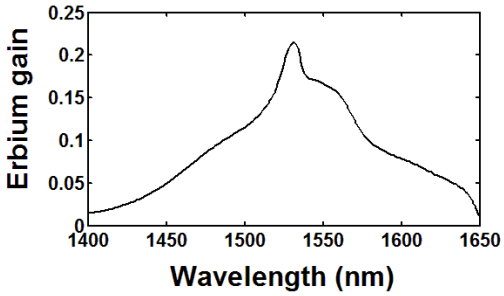

Figure 3.2: Wavelength dependent Erbium gain profile

where g is the frequency- or wavelength-dependent Erbium gain (Fig. 3.2) with its maximum at 1531 nm and $\widetilde{\mathcal{F}}(\cdot)$ denotes the backward Fourier transform from the frequency to the time domain. *Note that there is no Er-gain, i.e. $g = 0$, for the first (fibre A) and third (fibre C) stage of the proposed setup!*

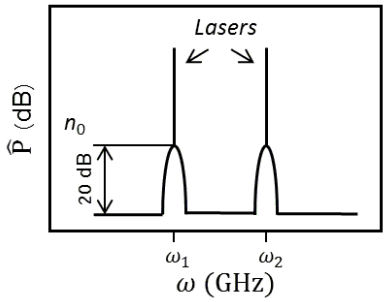

Figure 3.3: Schematic representation of the initial condition

Eq. 3.46 constitutes the final pulse-propagation equation we were looking for. The initial condition at $z = 0$ for this equation reads as

$$A_0(t) = \sqrt{P_0}\cos(\omega_c t) + \sqrt{n_0(t)}\exp\left(i\phi_{\text{rand}}(t)\right), \tag{3.47}$$

where the first term describes the two-laser optical field with a peak power of P_0 and a central frequency $\omega_c = (\omega_1 + \omega_2)/2$ that coincides with the central wavelength of $\lambda_c = 1531$ nm. The second term in Eq. 3.47 describes the noise field and has an amplitude varying between 0 and $\sqrt{n_0}$ and a phase ϕ_{rand} randomly varying between 0 and 2π. The deployment of optical filters within the experiment (Fig. 2.1) coincides mathematically with the convolution of the randomly destributed noise floor with two Gaussians that have the widths of 30 GHz and the depths of 20 dB. The maximum of each Gaussian is positioned at the respective laser frequency line as shown in Fig. 3.3 [40].

3.3 Numerical Methods

The numerical integration of Eq. 3.46 and Eq. 3.47 is performed by means of the Fourth-Order Runge-Kutta in the Interaction Picture Method (RK4IP). To explain the RK4IP algorithm, we start with the most commonly used numerical scheme for solving the GLNS, namely with the split-step Fourier method. Within this picture, Eq. 3.46 is formally viewed as

$$\frac{\partial A}{\partial z} = \left(\hat{D} + \hat{N}\right) A \tag{3.48}$$

with the $\hat{D}$ being the linear operator and $\hat{N}$ the nonlinear operator. The operators are defined as

$$\hat{D}(\cdot) = i\sum_{k=2}^{K} \frac{i^k}{k!}\beta_k \frac{\partial^k(\cdot)}{\partial t^k} - \frac{\alpha}{2}(\cdot) + \tilde{\mathcal{F}}\left(g(\omega)\widetilde{(\cdot)}\right), \tag{3.49}$$

$$\hat{N}(\cdot) = i\frac{\gamma}{A}\left(\left(1 + \frac{i}{\omega_0}\frac{\partial}{\partial t}\right) A \int_{-\infty}^{\infty} R(t')|A(z, t-t')|^2 dt'\right)(\cdot). \tag{3.50}$$

The linear dispersion operator is evaluated in the Fourier domain via the forward and backward Fast Fourier Transform (FFT), whereas the nonlinear operator is treated in the time domain. Within the symmetric split-step Fourier method, the solution of Eq. 3.48 over a step h reads then as [63]:

$$A(z+h, T) = A(z,t)\exp\left(\frac{h}{2}\hat{D}\right)\exp\left(\int_z^{z+h} \hat{N}(z')dz'\right)\exp\left(\frac{h}{2}\hat{D}\right). \tag{3.51}$$

The global error of the symmetric split-step Fourier method is of the order of $O(h^2)$. It can be reduced to the order of $O(h^4)$ if the Fourth-Order Runge-Kutta (RK4) method is chosen [63, 64].

Within the RK4IP method, Eq. 3.46 is transformed into the interaction picture to separate the effect of the dispersion contained in $\hat{D}$ from the nonlinear nondispersive terms in $\hat{N}$. The optical field envelope A is transformed into the interaction picture representation by

$$A_{IP} = \exp\left(-(z-z')\hat{D}\right) A, \tag{3.52}$$

where z' is the separation distance between the interaction picture and the normal one. The evolution of A_{IP} is given by

$$\frac{\partial A_{IP}}{\partial z} = \hat{N}_{IP} A_{IP}, \tag{3.53}$$

where

$$\hat{N}_{IP} = \exp\left(-(z-z')\hat{D}\right)\hat{N}\exp\left((z-z')\hat{D}\right) \tag{3.54}$$

denotes the nonlinear operator in the interaction picture [63].

The number of FFTs that is required for a straight-forward solution of Eq. 3.53 by means of RK4 can be reduced from 16 to 8 by choosing $z' = z + \frac{h}{2}$. The solution of Eq. 3.46 reads then as [63, 65, 66]:

$$A(z+h,t) = \exp\left(\frac{h}{2}\hat{D}\right)\left(A_{IP} + \frac{k_1}{6} + \frac{k_2}{3} + \frac{k_3}{3}\right) + \frac{k_4}{6} \tag{3.55}$$

with

$$\begin{aligned}
A_{IP} &= \exp\left(\frac{h}{2}\hat{D}\right)A(z,t), && (3.56)\\
k_1 &= \exp\left(\frac{h}{2}\hat{D}\right)\left(h\hat{N}(A(z,t))\right)A(z,t), && (3.57)\\
k_2 &= h\hat{N}\left(A_{IP} + k_1/2\right)\left(A_{IP} + k_1/2\right), && (3.58)\\
k_3 &= h\hat{N}\left(A_{IP} + k_2/2\right)\left(A_{IP} + k_2/2\right), && (3.59)\\
k_4 &= h\hat{N}\left(\exp\left(\frac{h}{2}\hat{D}\right)(A_{IP} + k_3)\right)\left(\exp\left(\frac{h}{2}\hat{D}\right)(A_{IP} + k_3)\right). && (3.60)
\end{aligned}$$

The global error of the RK4IP method is of the order of $O(h^4)$ [63]. The local error can be improved even to the order of $O(h^6)$ rather than $O(h^5)$ [65]. To achieve a highest possible level of accuracy, the RK4IP method is combined with the local error method within this work [49].

The original MATLAB code for integration of Eq. 3.46 and Eq. 3.47 by means of RF4IP was provided by Andrés A. Rieznik. It calculates and visualises the optical fields as well as the OCF spectra according to the proposed fibre-based approach for generation of OFC for low and medium resolution applications in Astronomy (Sec. 2.2). Specifically, it is possible to calculate the optimum fibre lengths using this code. In its original form, this code was used to obtain the results presented in Sec. 8. It was extended, changed or overworked to calculate the results presented in Sec. 6, Sec. 7, Sec. 9, and Sec. 10.

4 Types of Waves in Optical Fibres

In the previous section, we derived the Generalised Nonlinear Schrödinger Equation (GNLS) (Eq. 3.46) for the description of the ultra-short pulse propagation in silica fibres. This equation includes the higher-order dispersion terms, the optical Kerr effect, the Raman effect, the self-steepening, and the optical losses. The wavelength-dependent Erbium-gain profile is also included to describe the light amplification in the secon fibre stage of the proposed fibre-based approach for the generation of OFC (Fig. 2.1). However, the core of the pulse-propagation equation, i.e. the Nonlinear Schrödinger Equation (Eq. 3.40) with the cubic nonlinearity that represents the optical Kerr effect, is decisive for the pulse form and the way how the pulses propagate through the fibre:

$$\frac{\partial A}{\partial z} + i\frac{\beta_2}{2}\frac{\partial^2 A}{\partial t^2} = i\gamma|A|^2 A. \tag{4.1}$$

The higher-order dispersion terms, the Raman effect and the self-steepening can be considered as rather small perturbations to the governing NLS. Basically, to be able to predict the pulse dymanics, one needs to solve the NLS either numerically or analytically.

The exact solutions to the NLS are obtained via the usage of such mathematical methods like the Inverse Scattering Transform, the Darboux transformation, the Bäcklund transformation, the bilinear Hirota method. For these methods to be applied, the equation needs to be integrable. This is exactly the case when the NLS is written as presented in Eq. 4.1, any additional terms might destroy the integrability and make the usage of the mentioned methods not possible. The analytical solutions of the NLS are often complicated expressions that contain algebraic combinations of exponential, trigonometric, and polynomial functions of the coordinates z and t [69, 70, 71].

However, only a few types of analytic solutions of the NLS are interesting for the physics described within the framework of this thesis, namely the plane waves, the solitary waves and the periodic solutions.

4.1 Solitons as Solutions of the Nonlinear Schrödinger Equation

To the class of the exact solitary-wave solutions of the NLS belong the so called solitons with their typical sech-profile (Fig. 4.1):

$$A(z,t) = NA_0 \mathrm{sech}(t) e^{i\gamma|A_0|^2 z/2}, \tag{4.2}$$

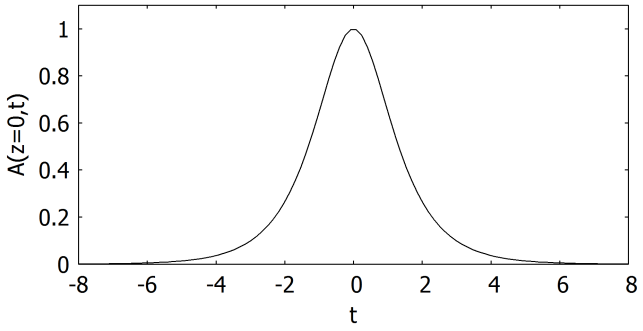

Figure 4.1: Fundamental soliton for the normalised time coordinate t, the initial condition $z = 0$, $A_0 = 1$, and $N = 1$

where t is a normalised coordinate and A_0 is a constant amplitude. Later on, t will play the role of the time coordinate and A_0 will be connected with the input power P_0 via $A_0 = \sqrt{P_0}$. N is a scale factor. Solitons have the following properties [67, 61]:

- they are localised structures
- they preserve their form
- they can interact with other solitons and emerge from the collision unchanged, except for a phase shift.

Due to these particle-like features, solitons obtained their name through Zabusky and Kruskal in 1965. The Greek ending "on" means "particle" and underlines the peculiar behaviour of these solitary waves [68].

The first recorded description of solitons was made by the Scottish scientist John Scott Russel in 1834 after he saw "a rounded smooth well-defined heap of water, which continued its course along the [Edinburgh-Glasgow] channel apparently without change of form or diminution of speed" for over two miles [69]. Since then, the solitons have been observed in a variety of physical systems, for instance in plasma physics, optical waveguides, Bose-Einstein condensate, phase transitions, bimolecule dynamics, open flow motions, spatially extended nonequilibrium systems [72, 73]. In particular, the solitons have drawn tremendous attention in telecommunication, where they can be used as "information bits" for parallel information storage and processing [74, 75, 76, 77]: the presence of an optical soliton in a nonlinear medium denotes an "one", the absence a "zero" within the frame of the binary alphabet. Not all these systems are described only by means of the NLS equation. Depending on the features of a given system, different types of nonlinear partial differential equations having solitons as solutions are deployed, for example the Korteweg-de Vries equation [68], the nonlinear Klein-Gordon equation [78], the complex Ginzburg-Landau equation [61, 79], and the Lugiato-Lefever equation [77, 80].

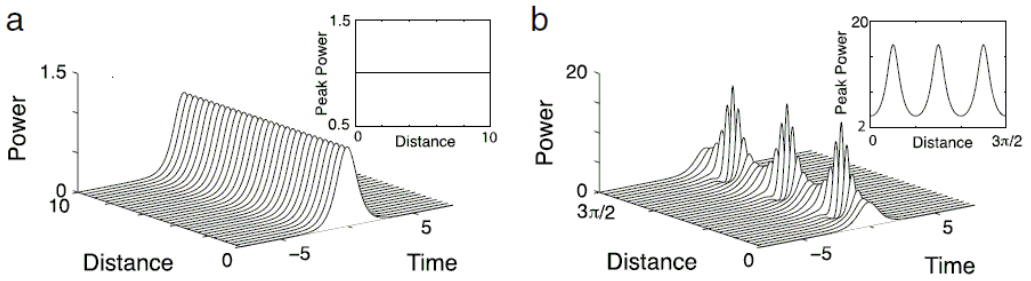

Figure 4.2: Propagation of a fundamental soliton (a) and a higher-order soliton with the order $N = 2$ (b) [83]

Depending on the features of a specific system, the localisation of solitons occurs either temporally, or spatially, or both. In systems, where the solitons are temporally localised, the localisation is due to a balance between the dispersion and the nonlinearity of the medium. The physical effect behind the formation of such temporal solitons is the self-phase modulation (cf. 3.1.1) [81]. In systems in which the solitons appear as spatially localised structures, i.e. as spatial solitons, the formation of these waves is given by the balance between the diffraction and the nonlinearity of the medium [61].

In Eq. 4.2, the scale factor N denotes the so-called soliton order. This number incorporates the important balance between the diffraction or the dispersion and the nonlinearity of the medium. In the next section, we will see what is the exact expression for N in case of optical fibres. It is important to know that solitons with $N = 1$ are called fundamental solitons. In this case, the diffraction or the dispersion of the medium is completely balanced by the nonlinearity which garantees extraordinary stability of the fundamental solitons against perturbations. For $N < 1$, the dispersion or the diffration of the medium dominates having the disintegration of the soliton as a result. For $N > 1$, the nonlinearity of the medium prevails [45]. Solitons with the order $N > 1$ are often referred to as higher-order solitons. They constitute states of two or more $N = 1-$solitons that propagate with nearly the same velocity and centre positions [82]. Contrary to the fundamental solitons that preserve their form as they propagate, the shape of a higher-order soliton evolves periodically with a period of $\pi/2$ (Fig. 4.2) [83, 84]. Within a higher-order soliton, there is no binding energy that holds together the individual $N = 1-$solitons. Thus, any perturbations of the NLS can lead to the break-up (fission) of the solitons with $N > 1$ [82].

As already mentioned, the pulse-propagation equation needs to be integrable, i.e. of the form of Eq. 4.1 to have solitons as solutions as presented above. An important feature of the physical systems that are described by this pure NLS is that they preserve energy, i.e. they are conservative. However, if any losses or some gain is added to a system, it loses its conservative nature and becomes dissipative. The solitons that are formed in such systems are often referred to as dissipative solitons. For them to be

stationary objects, not only the balance between the dispersion and the nonlinearity or the diffraction and the nonlinearity is crucial, but also the balance between the gain and the loss: even a slightes prevailing of the gain will let the solitons grow indefinitely or dissappear completely due to the losses [85].

4.2 Solitons in Optical Fibres

In the region of the anomalous (negative) dispersion, i.e. for wavelengths $\lambda > 1300$ nm in conventional single-mode fibres, bright temporal solitons constitute stable NLS-solutions:

$$A(z,t) = N\sqrt{P_0}\mathrm{sech}\left(\frac{t}{T_0}\right)e^{i\gamma P_0 z/2} \tag{4.3}$$

with T_0 being the pulse width and P_0 the initial optical peak power of the light source. Note that the cordinates t and z are not normalised as they were in the previous section (Eq. 4.2) and have now the meaning of time and propagation distance, respectively [45, 81, 86]. The theoretical prediction of the existence of optical solitons in single-mode fibres was made by A. Hasegawa et al. already in 1973. In 1980, L. F. Mollenauer et al. reported the first experimental observation of solitons in fibres [51, 81]. Since then, the solitons have been thoroughly studied to use them as information bits for telecommunication applications [81, 86, 84, 77, 87].

In optical fibres, the soliton order N is given as a ratio between the dispersion and the nonlinearity of the fibre glass:

$$N^2 = \frac{\gamma P_0 T_0^2}{|\beta_2|}, \tag{4.4}$$

where the expression $\frac{T_0^2}{|\beta_2|}$ is the dispersion length L_D and $\frac{1}{\gamma P_0}$ the nonlinear length L_{NL}. Both lengths characterise the soliton dynamics in optical fibres. Thus, if the dispersion length is shorter than the nonlinear length, the dispersive effects dominate. At the distance L_D, the linear dispersion causes the solitons to broaden to twice their initial widths. On the contrary, the pulse compression due to the self-phase modulation prevails if $L_{NL} < L_D$. At the distance L_{NL}, the pulses achieve a nonlinear phase rotation of π at their maxima [83]. The existence of fundamental solitons is given if both characteristic lengths are equal, i.e $L_D = L_{NL}$ [81, 85]. The periodic evolution of a higher-order soliton occurs over the soliton period z_0 that is expressed via the dispersion length [45]:

$$z_0 = \frac{\pi}{2}L_D = \frac{\pi}{2}\frac{T_0^2}{|\beta_2|}. \tag{4.5}$$

All fibres are dissipative systems, because the glass material absorbes at least 0.2 dB/km of the light optical power [45]. In fibres that are doped with such rare Earth ions like Erbium or Ytterbium, the light gets amplified via the stimulated emission in the dopants so that the optical gain is greater than the optical losses if the doped fibres are suitably pumped [84, 87]. Therefore, the solitons (no matter if fundamental of higher-order) that

propagate through optical fibres are always subjected either to the optical losses or to the gain. As we discussed previously, such solitons are called dissipative solitons.

Any asymmetry in the temporal or spectral profile will cause an eventual fission of higher-order solitons. The optical fibre loss is never symmetric for solitons with order $N > 1$. The reason for that lies in the uncertainty effects: it is not possible to know the central positions and velocities of the soliton components at the same time. Thus, the components of a higher-order soliton will always have either slightly different velocities or will not share the same central positions. The Raman effect causes the evolution of an asymmetric soliton spectrum and, thus, leads to the break-up of higher-order solitons [82].

Another perturbation that needs to be mentioned is the third-order dispersion (TOD) in optical fibres. If the optical pulses propagate far from the zero-disperion wavelength that lies at ca. 1300 nm in case of conventional single-mode fibres, the TOD shifts the soliton peaks from their original positions. For a typical TOD-value of $\beta_3 = 0.1$ ps^3/km, the solitons in the femto-second range are slowed down by the rate of 1.7 ps/km for the pulse width of $T_0 = 100$ fs. The impact of the TOD is even more severe, if the pulses propagated near the fibre zero-dispersion wavelength such that β_2 is nearly zero. In this case, the TOD causes the fission of higher-order solitons [45].

4.3 Soliton Molecules in Optical Fibres

Firstly proposed in 1994 and since then numerically and experimentally studied, there exist compound soliton states called soliton molecules. A soliton molecule consists of two bright pulses with opposite phases, the phase jump of π occurs at the central power zero (Fig. 4.3) [88]. Contrary to higher-order solitons, the components of a soliton molecule are hold together by a non-zero amount of binding energy. There is a stable equilibrium distance between the two pulses [89]. If they are brough together closer than the equilibrium distance, they experience a repulsive force. If they are beyond that distance, they get attracted to each other. This behaviour is reminiscent of the equilibrim separation of the two constituents of a diatomic molecule - hence the name "solion molecule" [81, 85]. Soliton compounds can contain more than only two solitons: 3(and more)-soliton molecules have been reported as well [90, 91, 92, 93], an extension to a soliton train is also possible [115].

Generally, soliton molecules constitute weakly bound states. In fibres with a constant dispersion, such compound states are unstable. Stable soliton molecules are formed if they propagate in dispersion-managed fibres (DMF) that consist of segments with alternate positive and negative group-velocity dispersion values [81, 83, 85]. In DMFs, soliton molecules inherit their stability from fundamental solitons [89], whereas molecules with odd number of components are more stable as the ones with even number [92]. However, the Raman effect causes the pulses to receive power-dependent frequency

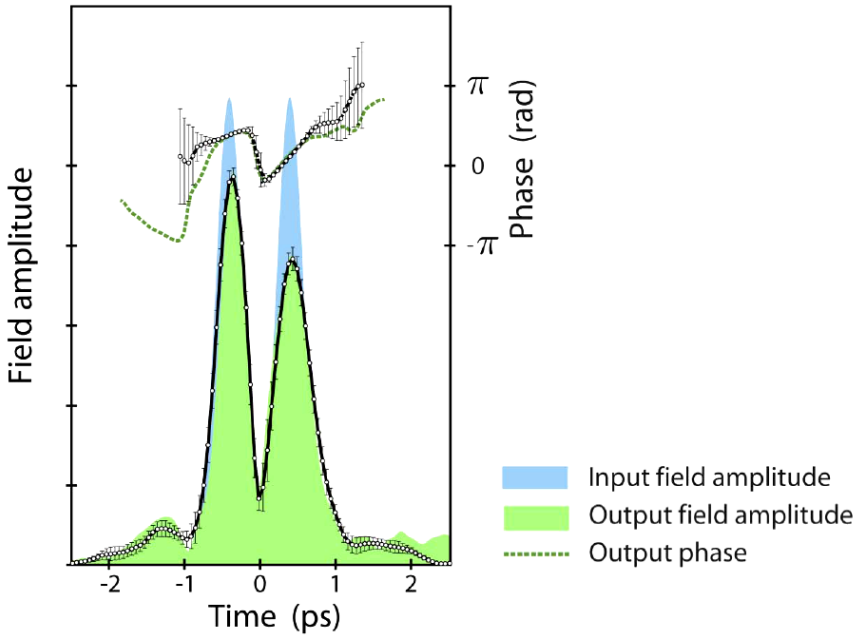

Figure 4.3: The input field, the output field, and the phase of a soliton molecule [90, 91]

shifts leading to a different peak heights of the components. This causes differential phase shifts which distorts the soliton molecule [90].

As for the deployment of molecule solitons, they can be used for the extension of the coding alphabet by further symbols like "no pulse", "single pulse", "double pulse", etc., in the telecommunication [89].

4.4 Periodic Waves in Optical Fibres

4.4.1 Modulational Instability

The NLS equation (Eq. 4.1) has a stable plane-wave solution of the form

$$A(z,t) = \sqrt{P_0}e^{i\gamma P_0 z} \tag{4.6}$$

with P_0 being the initial input power (coming from a CW laser with the frequency ω_1) if the GVD parameter is positive, i.e. $\beta_2 > 0$. However, for silica fibres, this plane-wave solution becomes unstable if the GVD parameter is negative, i.e. $\beta_2 < 0$, which is the case for wavelengths $\lambda > 1300$ nm [81].

Thus, if a periodic perturbation (for instance, a second CW laser beam with the frequency ω_2) is applied on the plane wave (Eq. 4.1), it gets amplified. The amplification

of the perturbation goes along with the cascading generation of new frequency components around the laser frequency ω_1 based on FWM (Sec. 2.1). The spectral enrichment leads to the modulation of the initial CW field and the subsequent break-up of the CW radiation into a train of ultrashort pulses. This instability of a plane wave against periodic perturbations is often referred to as modulational instability (MI). [47, 94].

Let us consider this in more detail. For that, Eq. 4.6 should be perturbed by means of a small perturbation function $a(z,t)$, $|a(z,t)| \ll \sqrt{P_0}$:

$$A(z,t) = \left(\sqrt{P_0} + a(z,t)\right) e^{i\gamma P_0 z}. \tag{4.7}$$

Inserting Eq. 4.7 into Eq. 4.1 within the frame of the linear stability analysis, we get an equation for the evolution of the perturbation function:

$$\frac{\partial a}{\partial z} + i\frac{\beta_2}{2}\frac{\partial^2 a}{\partial t^2} = i\gamma P_0 \left(a + a^*\right) \tag{4.8}$$

that is easily solved in the frequency domain. The solution is

$$a(z,t) = C_1 e^{i(Kz-\Omega t)} + C_2 e^{-i(Kz-\Omega t)}, \tag{4.9}$$

where K and Ω are associated with the wave vector and the frequency of the perturbation function via $K = |k_1 - k_2|$ and $\Omega = |\omega_1 - \omega_2|$, respectively. The numbers C_1 and C_2 provide a family of solutions, the nontrivial ones are given when the following dispersion relation is fulfilled:

$$K = \pm\frac{|\beta_2\Omega|}{2}\left(\Omega^2 + \mathrm{sgn}(\beta_2)\Omega_c^2\right)^{1/2} \tag{4.10}$$

with the power-dependent critical frequency Ω_c that is given by

$$\Omega_c = \pm 2\sqrt{\frac{\gamma P_0}{|\beta_2|}}. \tag{4.11}$$

This dispersion relation shows that for normal GVD, i.e. for $\beta_2 > 0$, K is real for any Ω and the plane wave solution (Eq. 4.6) is stable against small perturbations. In the case of anomalous dispersion, i.e. for $\beta_2 < 0$, K becomes imaginary for $|\Omega| < \Omega_c$ and the perturbation function grows exponentially with the propagation distance z (Eq. 4.9). The frequency-dependent gain exists only if $|\Omega| < \Omega_c$ and is given by

$$g_{MI}(\Omega) = |\beta_2\Omega|\left(\Omega_c^2 - \Omega^2\right)^{1/2}. \tag{4.12}$$

The gain has its maxima at two frequencies given by

$$\Omega_{max} = \pm\frac{\Omega_c}{\sqrt{2}} = \pm\left(\frac{2\gamma P_0}{|\beta_2|}\right)^{1/2}. \tag{4.13}$$

In other words, if a perturbing wave with the frequency $\omega_2 = \omega_1 + \Omega$ copropagates with the CW beam with the frequency ω_1, it experiences a net power gain according to

Eq. 4.12 as long as $|\Omega| < \Omega_c$. From the physical point of view, it means that the energy of two photons from the intense pump beam with ω_1 are used to create two photons, one at the frequency ω_2 and another one at the frequency $\omega_1 - \Omega$. In the time domain, this process coincides with the conversion of the initial CW beam (at ω_1) into a periodic pulse train with the pulse repetition period given by $T = \frac{2\pi}{\Omega}$ [45, 46].

4.4.2 Akhmediev Breathers

In 1986, N. Akhmediev and V. Koneev published a paper reporting a familiy of analytic periodic solutions of the NLS (Eq. 4.1) that describe the "modulational instability, i.e. the growth of long-wave periodic perturbations on the background of a continuous wave of constant amplitude". In particular, the amplitude of the initial small periodic modulation of the plane wave experiences growth and a subsequent decrease over time similar to the Fermi-Pasta-Ulam return in a system of coupled oscillators [95]. A temporally periodic, but spatially confined train of pulses on a finite background with the repetition period $T = 2\pi/\Omega$ called Akhmediev breather (AB) arises as a result. It has the following form:

$$A(z,t) = \sqrt{P_0}\frac{(1-4\bar{a})\cosh(\bar{b}z/L_{NL}) - i\bar{b}\sinh(\bar{b}z/L_{NL}) + \sqrt{2\bar{a}}\cos(\Omega t)}{\sqrt{2\bar{a}}\cos(\Omega t) - \cosh(\bar{b}z/L_{NL})}, \tag{4.14}$$

where P_0 is again the initial power and L_{NL} is the nonlinear length, $L_{NL} = (\gamma P_0)^{-1}$. The parameter $\bar{a}$ varies in the interval $0 < \bar{a} < 1/2$, the parameter $\bar{b}$ is defined by $\bar{b} = \sqrt{8\bar{a} - 16\bar{a}^2}$ and governs the MI growth. Ω is the modulation frequency given by

$$\Omega = \Omega_c \sqrt{1 - 2\bar{a}} \tag{4.15}$$

with Ω_c being the critical frequency (Eq. 4.11). According to Eq. 4.13, the maximum MI gain occurs for $\bar{b} = 1$ and $\bar{a} = 1/4$ [96].

As already mentioned, the amplitude of the individual pulses within an AB undergoes temporally periodic evolution. The maximum amplitude coincides with the minimum temporal pulse width at $z = 0$. The NLS solution at this point describes the maximally compressed AB and is given by [10]:

$$A(z=0,t) = \sqrt{P_0}\frac{(1-4\bar{a}) + \sqrt{2\bar{a}}\cos(\Omega t)}{\sqrt{2\bar{a}}\cos(\Omega t) - 1}. \tag{4.16}$$

Further, depending on the value of the parameter $\bar{a}$, a distinction is made between three cases (Fig. 4.4):

- for $0 < \bar{a} < 1/2$, the solution Eq. 4.14 describes Akhmediev breathers that are temporally periodic, but spatially localised
- for $\bar{a} = 1/2$, one has the case of Peregrine solitons that are temporally and spatially localised [97, 94]

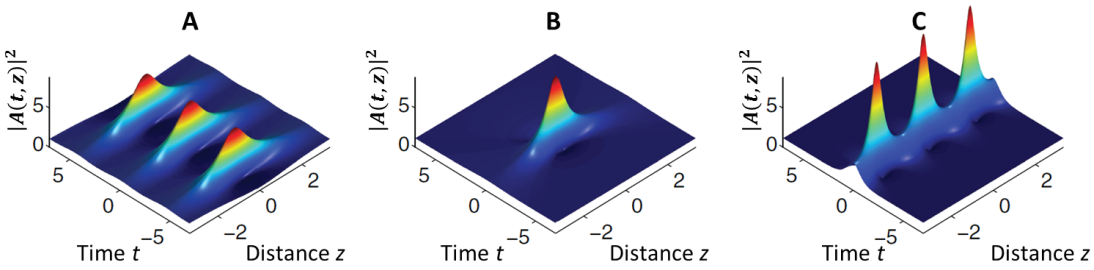

Figure 4.4: Comparison between an Akhmediev breather (A) with $\bar{a} = 1/4$, a Peregrine soliton (B) with $\bar{a} = 1/2$, and a Kuznetsov-Ma soliton (C) with $\bar{a} = 1$[97, 99]

- for $1/2 < \bar{a} \leq 1$, Eq. 4.14 describes the case of Kuznetsov-Ma solitons that are temporally localised, but spatially periodic [99, 100].

In the further course (Sec. 6), we will see that the initial condition given by Eq. 3.47 generates neither the Akhmediev breathers, nor the Peregrine solitons, nor the Kuznetsov-Ma solitons if it is integrated by means of the pulse-propagation equation Eq. 3.46, but delivers an input-power dependent state that consists of a collective soliton crystal, an intermediate state, and the state of free fibre solitons.

Now, after the reader was introduced to the solitary waves (fundamental and higher-order solitons), the soliton molecules and the periodic waves (Akhmediev breathers, Peregrine solitons, and Kuznetsov-Ma solitons) that all together are solutions of the Nonlinear Schrödinger Equation (Eq. 4.1), we proceed with the last purely theoretical chapter, namely the chapter "Soliton Compression in Optical Fibres", before we go over to the chapters that contain results of our studies.

5 Soliton Compression in Optical Fibres

The soliton compression in optical fibres is based on the effect of self-phase modulation. In Sec. 3.1.1, we mentioned that spectral profile of a pulse gets broadened due to the intensity-dependence of the refractive index. In case of normal fibre group-velocity dispersion (β_2 positive), i.e. dispersion for wavelengths < 1.3 μm, the linear part of the refractive index (Eq. 3.4) induces a chirp: the red components of the spectrum propagate faster than the blue ones inside the fibre medium. The pulse gets spectrally broadened due to the nonlinear part of the refractive index n_2 and disperses in the time domain due to the linear part n_0.

In the regime of anomalous GVD (β_2 negative) which appears for wavelengths > 1.3 μm, the blue components of the pulse spectrum travel faster than the red ones. The spectral profile decreases in time, the pulse itself gets compressed [56]. The compression factor describes the compression effectiveness after the propagation length L and is given by

$$C = \frac{T_{FWHM}(z = 0)}{T_{FWHM}(z = L)} \tag{5.1}$$

with T_{FWHM} being the full pulse width at the half of the maximum intensity [46].

The compression of solitons (also called soliton-effect compression) in fibres is based on the interplay between the self-phase modulation and the anomalous GVD. There are two commonly considered techniques for the soliton-effect compression: the adiabatic pulse compression method and the higher-order (non-adiabatic) soliton compression. In case of adiabatic soliton compression, a fundamental soliton is propagated through a map of fibres with monotonically decreasing dispersion or a fibre with steady amplification along its length (for instance, an Erbium-doped fibre as described in Sec. 2.2). If the dispersion decreases sufficiently slow or the fibre gain is not too high, the fundamental soliton can adjust itself to maintain the balance between the fibre dispersion and nonlinearity by reducing its pulse width [101, 102, 103]. The main drawback of this technique is that the maximum compression factor is limited to ca. 20 [103].

Much higher compression factors can be achieved in case of the higher-order soliton compression. Within the framework of this technique, a proper fibre length is chosen at which a higher-order soliton (undergoing periodic evolution over the soliton period) is maximally compressed. The compression factors in a conventional single-mode fibre can be estimated by the relation

$$C \approx 4.1N, \tag{5.2}$$

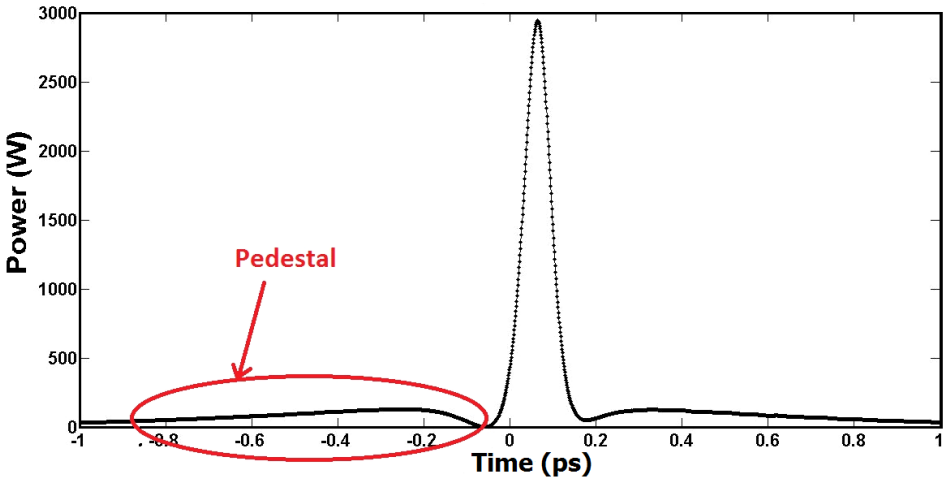

Figure 5.1: Example of a pulse pedestal after propagation through the amplifying fibre B of the proposed approach for generation of fibre-based OFC (Sec. 2.2)

where N is the soliton order given by Eq. 4.4 [46, 54]. However, this technique suffers from the build-up of big pulse pedestals (pulse flanks) (Fig. 5.1) that consist of dispersive waves radiated from the soliton pulses and being subjected to the GVD [104]. The total pulse energy is split between the desired compressed pulse and the undesired pedestal background (cf. the difference between a mathematically perfect *sech*−profiled soliton in red and a soliton that propagated through a fibre in black in Fig. 7.2). Up to 80% of the pulse energy can be lost into the pedestal [103].

For pulse widths < 100 fs, one should take a closer look if such higher-order effects like the self-steepening, the TOD, and the Raman intra-pulse scattering might affect the compression efficiency. In our case, the pulses are compressed down to 50 − 100 fs in the second amplifying fibre stage depending on the system parameters. For such pulse widths, the effect of the self-steepening is negligible since it starts to play a role for pulses in the range of ~ 10 ps. The TOD can degrade the quality of the compressed pulses if they propagate close to the zero-dispersion wavelength lying typically at ca. 1300 nm. Since, in our case, the pulses travel relatively far away way from the zero-dispersion length (the central wavelength is λ_c = 1531 nm), the effect of the TOD will also be negligible. This was also proved by our simulations that are beyond the scope of this thesis.

The only effect that plays a (minor) role in the proposed setup is the intra-pulse Raman scattering. It induced a soliton frequency-shift towards the lower (red) frequecies that coincides with a delay of optical pulses because of a change in the group-velocity of the pulse (Fig. 2.2B). This delay does not affect the quality of the pulse compression. On the contrary, it helps to produce almost pedestal-free pulses: the narrow com-

pressed spike travels slower that the pedestal and, eventually, separates from it because of the change in the group-velocity induced by the Raman effect (well seen after the propagation through the third highly-nonlinear fibre stage in Fig. 2.2C). If the pedestal is removed by spectral filtering, one gets red-shifted, pedestal-free, well-compressed pulses [46, 105, 106, 107].

6 Pulse Build-up in the First Fibre Stage

In Sec. 2.2, we introduced a setup for generation of optical frequency combs for the purpose of the calibration of astronomical spectrographs in the low- and medium resolution range. To be able to control the quality and the bandwidth of the OFC, it is crucial to understand the evolution of the optical pulses as they propagate through the fibres. Especially, one needs to know what happens in the first fibre stage (fibre A in Fig. 2.1) where the pulses arise out of the initial deeply-modulated bichromatic cosine-wave (Eq. 3.47). However, the pulse-propagation equation (Eq. 3.46) is not integrable. Therefore, it cannot be solved analytically. In this section, we use the numerical technique called Soliton Radiation Beat Analysis (SRBA) to get more insight into the pulse evolution.

6.1 Akhmediev Breather or Kuznetsov-Ma Solitons?

In Sec. 4.4.1, we discussed the impact of a small perturbation with the frequency ω_2 on a plane wave with the frequency ω_1 that propagates through a fibre with anomalous dispersion. In Sec. 4.4.2, Akhmediev breathers were introduced as analytic solutions of the NLS for such a case. Depending on the parameter $\bar{a}$, Eq. 4.14 describes the evolution of an Akhmediev breather, a Peregrine soliton, and a Kuznetsov-Ma soliton.

Due to the temporal periodicity of the initial condition (Eq. 3.47), it is reasonably to expect this initial condition to evolve into an Akhmediev breather (AB) or a Kuznetsov-Ma (KM) soliton in fibre A. In Ref. [99], B. Kibler et al. suggested and experimentally proved the existence of KM solitons in optical fibres. In fact, the optical power in our case looks similar to a train of temporally periodic KM solitons (Fig. 6.1). However, it needs to be carefully proven if optical structures that arise by using a bichromatic cosine-wave as initial condition (Eq. 3.47) have more similarities with Akhmediev breathers or Kuznetsov-Ma solitons.

To find out what type of NLS solutions the pulses in our case are similar to, we calculate the parameter $\bar{a}$ according to Eq. 4.15:

$$\bar{a} = \frac{1}{2}\left(1 - \frac{\Omega^2}{\Omega_c^2}\right). \tag{6.1}$$

In case of KM solitons, $\Omega^2 \leq 0$ (Ω_c^2 is positive per definition) which implies the temporal localisation of these optical structures. In our case, the modulational frequency Ω is given by $\Omega = 4\pi LFS = 4\pi\,(|\omega_1 - \omega_2|/2\pi)$ providing the same number of optical peaks

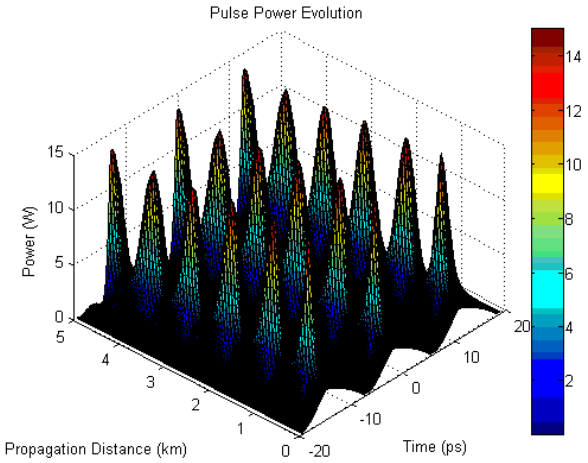

Figure 6.1: Pulse evolution in fibre A for the initial power $P_0 = 2.5$ W

as in the case of an AB. Obviously, this frequency is positive definite. So it is Ω^2. That means that, in our case, the initial bichromatic cosine-wave will definetively not evolve into a temporally periodic train of KM solitons. Thus, we expect it to evolve into structures that are similar to a travelling Akhmediev breather.

Fig. 6.2 shows the calculated values of parameter the $\bar{a}$ for three different values of the initial laser frequency separation, $LFS = 40$ GHz, $LFS = 80$ GHz, and $LFS = 160$ GHz, and different values of the input power, $0.0\text{ W} < P_0 \leq 6.0\text{ W}$. As one can see, for any values of LFS and P_0, the parameter $\bar{a}$ remains in the interval $[0, 0.5)$ which is the condition for Akhmediev breathers. This supports our idea that, for any parameters of fibre A, any values of the initial laser frequency separation LFS and the input power P_0, a bichromatic cosine-wave as initial condition is likely to evolve into optical structures that are similar to a (travelling) AB. We claimed evolution of KM solitons in Ref. [39]. This is disproved by our considerations here.

Comparison between Fig. 6.1 with Fig. 4.4A reveals that the pulse evolution in our case differs, however, from the evolution of an ideal AB. Thus, to find out what exactly happens in fibre A, we apply the numerical technique of Soliton Radiation Beat Analysis that will allow us to get a deeper insight into the pulse evolution in fibre A.

6.2 Soliton Radiation Beat Analysis of Pulses in the First Fibre Stage

In Sec. 6.1, we showed that a bichromatic cosine-wave (Eq. 3.47) should evolve into periodic structures that are close to travelling Akhmediev breathers. However, from the mathematical point of view, the theory of Akhmediev breathers cannot be directly

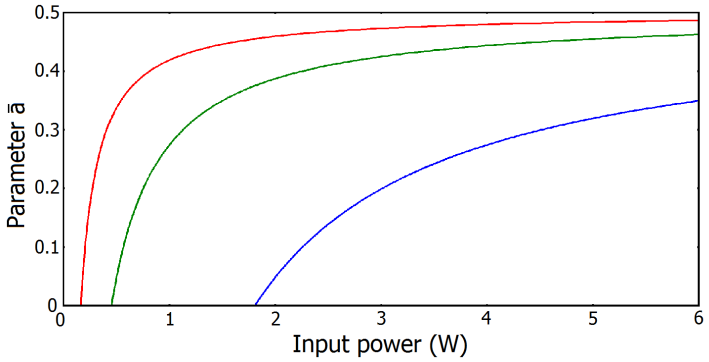

Figure 6.2: Parameter $\bar{a}$ for different value of input power P_0 and laser frequency separation LFS = 40 GHz (red curve), LFS = 80 GHz (green curve), and LFS = 160 GHz (blue curve)

applied for the description of the pulse formation in fibre A. The reason is that the perturbation of the initial CW field is not small any more. The Akhmediev solution of the NLS is given, however, only for a small perturbation (Sec. 4.4.2). In our case, the perturbing wave with the frequency $\omega_2 = \omega_1 + 2\pi LFS$ has the same intensity as the perturbed CW field with the frequency ω_1. Moreover, the formation of the new frequency components in the OFC spectrum occurs not around the frequency ω_1, but around both frequencies, ω_1 and ω_2. The new components have the same frequency spacing as the initial waves, namely $2\pi LFS$ (Fig. 2.3A). Further, the pulses within an Akhmediev breather undergo a periodic energy exchange via the finite background on which the pulses are "sitting". In our case, however, the pulses are separated from each other due to the fact that the initial wave is modulated down to zero, i.e. there is no background through which the pulses can interact and exchange energy.

To analyse the pulse formation in fibre A, we take advantage of the soliton radiation beat analysis (SRBA). The SRBA is a numerical technique that can answer the general question if solitons arise in a specific system and if the answer is "yes", the SRBA is able to provide the information about the energy, the velocity, the phase, and the position of each soliton involved [108, 109]. Since Eq. 3.46 is formulated in the co-moving frame, the velocity, the phase, and the position of solitons are not relevant because these can be set by the boundary conditions. Thus, the only important parameter left is the energy of solitons that can be related to the soliton order N (Sec. 4.1) [110].

6.2.1 Soliton Radiation Beat Analysis

The technique of SRBA should be introduced by a simple example. For that, the optical field $A(z,t)$ of fibre A is calculated by means of the numerical integration of Eq. 3.46 and Eq. 3.47. In Eq. 3.47, we set the noise amplitude to zero for the sake of simplic-

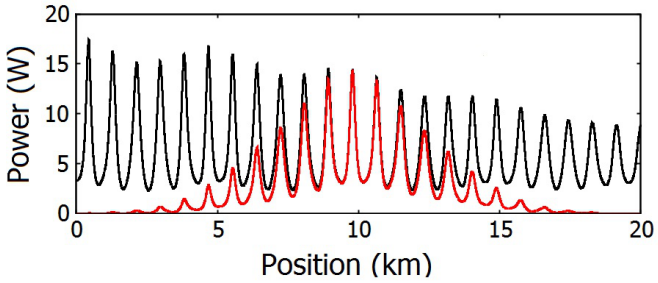

Figure 6.3: Optical power at $t = 0$ (black) and apodised optical power at $t = 0$ (red) vs. propagation distance for $P_0 = 3.3$ W [111]

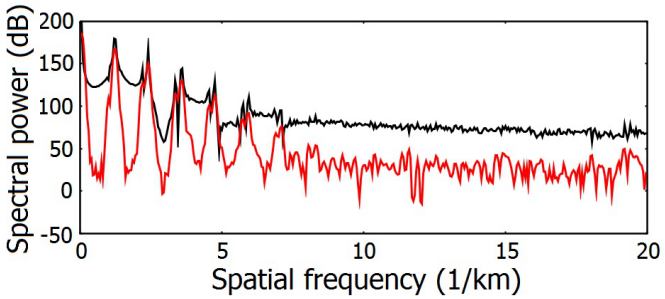

Figure 6.4: Spectral power of non-apodised optical power (black) and apodised optical power (red) vs. spatial frequency [111]

ity. The fibre parameters are chosen to be $\beta_2^A = -15$ ps^2/km, $\beta_3^A = 0.1$ ps^3/km, and $\gamma^A = 2$ W^{-1}km^{-1}. The optical losses are set to $\alpha^A = 0$ dB/km also for the sake of simplicity. The total fibre length is $L^A = 20$ km, the initial power $P_0 = 3.3$ W, and the laser frequency separation $LFS = 80$ GHz. The solution of Eq. 3.46 and Eq. 3.47 is calculated within a temporal window of 128 ps that is sampled with 2^{14} points.

After $A(z,t)$ is obtained, the optical power is calculated via $\hat{P}(z,t) = |A(z,t)|^2$. Using these data, we extract $\hat{P}(z) = \hat{P}(z, t = 0)$. As can be seen in Fig. 6.3, the power function $\hat{P}(z)$ (black curve) oscillates over the propagation distance z. This oscillation contains information about the involved solitons and their features.

To decode the information that is imprinted into the optical power oscillation, we perform a Fourier transform of the data $\hat{P}(z)$. The according Fourier spectral power $\tilde{P}(Z)$ is shown as the black curve in Fig. 6.4, where Z is the spatial frequency.

The oscillation of the optical power $\hat{P}(z)$ over the propagation distance results in peaks in the spatial frequency domain. Additionally to the peaks, there is a background seen in the spectrum. This background arises due to the discontinuity of $\hat{P}(z)$ at the boundaries and is an artifact of the Fourier transform. To suppress this artificial background, we

apodise $\hat{P}(z)$ by means of a Gaussian apodisation function that is presented as the red curve in Fig. 6.3. This function has the following form:

$$f(m) = \exp\left(-\left(\frac{m - M/2}{bM}\right)^2\right), \tag{6.2}$$

where $1/b$ is the apodisation strength and $m \in \{1, ..., M\}$ with M being the total number of distance sampling points [112].

As one can see in Fig. 6.4, the discontinuity of the apodised power $\hat{P}_{apo}(z)$ is effectively minimised at the boundaries compared to the non-apodised case. Accordingly, the Fourier-transformed power, i.e. $\tilde{P}_{apo}(Z)$, shows less background and the peaks are more visible (red curve in Fig. 6.4). Now, we can analyse the spectral-power peaks and draw conclusions about the involved solitons. However, to get more precise information about of the solitons and their beating frequencies, it is necessary to repeat the described algorithm for different values of the input power P_0 [113].

6.2.2 Initial Conditions

To find out what happens if a deeply-modulated bichromatic wave (Eq. 3.47) propagates through fibre A, we first choose two types of initial conditions that have predictable evolution known from literature, namely a single cosine-hump and a maximally compressed Akhmediev breather, and perform the SRBA on them. Having studied these two cases, we compare them with the SRBA results obtained using the bichromatic wave as initial condition (Eq. 3.47).

Here are the types of initial condition we will consider in this section.

- A temporally localised single cosine-hump (Fig. 6.5A) is expected to evolve into a soliton with a sech-profile in fibre A [45, 111, 114]:

$$A(z = 0, t) = \begin{cases} 0, & |t| > 1/LFS = 6.4 \text{ ps} \\ N\sqrt{P_0}\cos(\omega_c t), & |t| \leq 1/LFS = 6.4 \text{ ps} \end{cases} \tag{6.3}$$

  where $\omega_c = \left(\frac{\omega_1+\omega_2}{2}\right)$ such that $\omega_2 = \omega_1 + 2\pi LFS$.

- A temporally periodic maximally compressed Akhmediev breather (Fig. 6.5B) will propagate further as an Akhmediev breather through fibre A [10, 83, 111, 95]:

$$A(z = 0, t) = N\sqrt{P_0}\frac{(1 - 4\bar{a}) + \sqrt{2\bar{a}}\cos(\Omega t)}{\sqrt{2\bar{a}}\cos(\Omega t) - 1}, \tag{6.4}$$

  where $\Omega = 4\pi LFS$ due to reasons explained in Sec. 6.1.

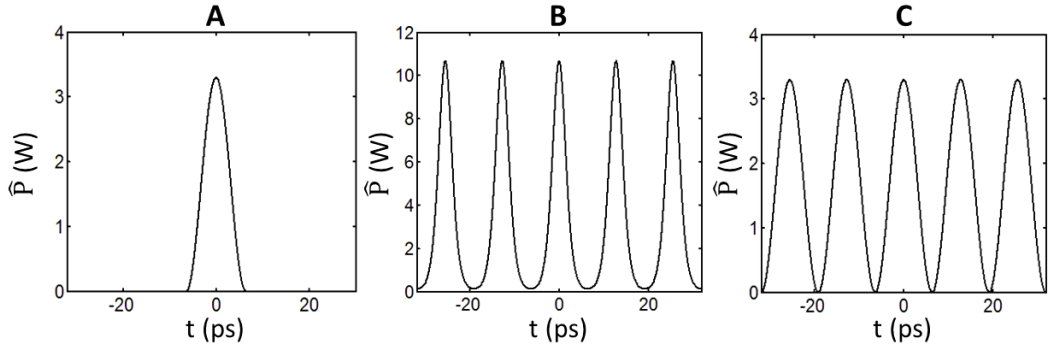

Figure 6.5: Three types of initial condition with initial power of $P_0 = 3.3$ W : A. Single cosine-hump, B. Maximally compressed Akhmediev breather, C. Deeply-modulated bichromatic cosine-wave according to the proposed setup (Sec. 2.2) [111]

- An experimentally accessible deeply-modulated bichromatic cosine-wave (Fig. 6.5C) that coincides with the initial condition of the proposed setup for generation of OFCs (Sec. 2.2) will be studied after two previous cases:

$$A(z = 0, t) = N\sqrt{P_0}\cos(\omega_c t) \tag{6.5}$$

with $\omega_c = \left(\frac{\omega_1+\omega_2}{2}\right)$ and $\omega_2 = \omega_1 + 2\pi LFS$.

In all three equations (Eq. 6.3-6.5), N is the scale soliton order (further referred to as soliton order) given by

$$N = \left(\frac{\gamma^A P_0}{(2\pi LFS)^2|\beta_2^A|}\right)^{1/2}. \tag{6.6}$$

The value of N correspods to the energy of the involved solitons. We use Eq. 6.6 rather than the one presented in Eq. 4.4 as the definition of the soliton order because for arbitrary pulses it is more practical to substitute the natural pulse width T_0 by $1/2\pi LFS$ [40, 113].

We use the following parameters for our studies: the input power is increased from $P_0 = 0.03$ W to $P_0 = 6.0$ W in steps of $\Delta P_0 = 0.03$ W, the total length of the fibre is $L^A = 20$ km sampled with $M = 20000$ points. As for the apodisation strength, the parameter b is set to $b = 0.2$. The time window is 128 ps sampled with 2^{14} points. The fibre parameters are again $\beta_2^A = -15$ ps^2/km, $\beta_3^A = 0.1$ ps^3/km, $\gamma^A = 2$ W^{-1}km^{-1}, and $\alpha^A = 0$ dB/km. The laser frequency separation is chosen to be $LFS = 80$ GHz [111].

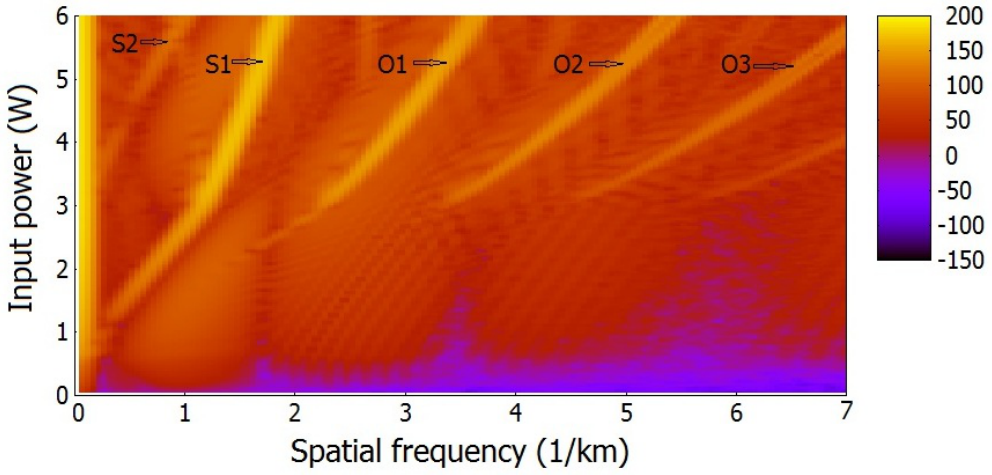

Figure 6.6: Spectral power for a single cosine-hump as initial condition and fibre length $L^A = 20$ km for different values of the input power P_0 [111]

6.2.3 Results

In any SRBA-graphs presented below, a strong peak is visible for any values of the initial power P_0 and the spatial frequency $Z = 0\ \mathrm{km}^{-1}$. This peak arises in the process of the Fourier transformation and corresponds to the average value of the optical power $\hat{P}(z)$. Since it constitutes a purely mathematical feature of the SRBA thechnique and, accordingly, does not contain any pieces of information about the solitons themselves, we will exclude it from consideration.

Single Cosine-Hump as Initial Condition

In Fig. 6.6 one can see the spectral power for different values of the input power P_0 that was obtained using a single cosine-hump as initial condition (Eq. 6.3). Typically, for a single soliton to arise, a positive input-power threshold value, $P_0 > 0$ W, is required [108, 114]. After this threshold value is reached, the soliton will evolve depending on $\sqrt{P_0}$ according to Eq. 6.6. In our case, such threshold exists at $P_0 = 0.7$ W and $Z = 0\ \mathrm{km}^{-1}$ denoting the beginning of branch $S1$ in Fig. 6.6. Thus, we can conclude that $S1$ constitutes a beating of a single soliton with the dispersive-waves background (pulse pedestals) which results in an oscillating behaviour of the optical power. According to Eq. 6.6, the order of the soliton that is involved into the beating is $N = 0.62$ (calculated at the input-power threshold). Since the soliton-order threshold for the creation of a fundamental soliton is $N = 0.5$, we can conclude that branch $S1$ constitutes a fundamental soliton [114].

The branches $O1$, $O2$, and $O3$ in Fig. 6.6 are the overtones of $S1$. Generally, overtones are a feature of the SRBA technique and contain no further information about the involved solitons. So, we will not focus our attention on the overtones in the course of

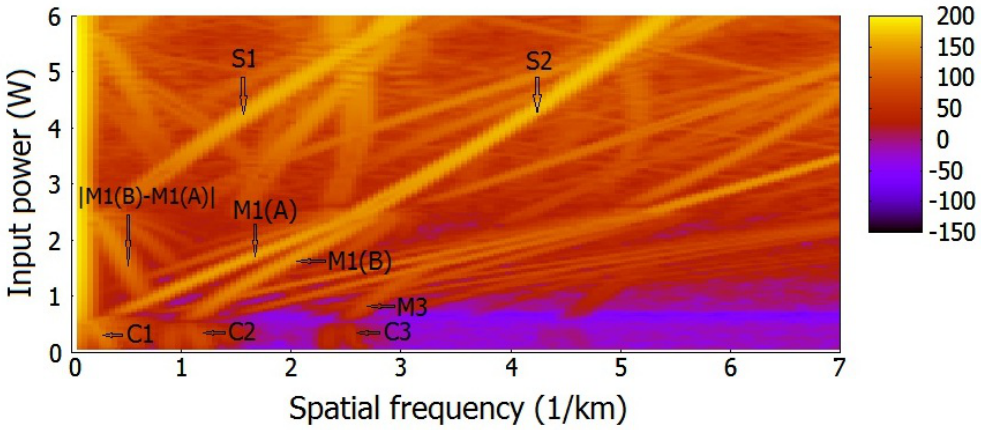

Figure 6.7: Spectral power for a maximally compressed Akhmediev breather as initial condition and fibre length $L^A = 20$ km for different values of the input power P_0 [111]

further studies.

The next branch $S2$ arising due to the beating of a soliton with the dispersive-waves background originates at $P_0 = 3.3$ W and $Z = 0$ km^{-1}. The soliton that is involved into this beating has the order $N = 1.35$ (calculated at $P_0 = 3.3$ W). Second-order solitons arise for $N \geq 1.5$ in a non-perturbed system [114]. Since the order of the $S2-$soliton is smaller than 1.5, the branch $S2$ constitutes another fundamental soliton. The energy growth of $S1$ with increasing input power starts decreasing as soon as $S2$ appears meaning that the energy provided by the input beam is now split between the two solitons. This manifests itself in the change of the slope of $S1$ that occurs at ca. $P_0 = 3.2$ W [111].

Maximally Compressed Akhmediev Breather as Initial Condition

Fig. 6.7 shows the spectral power that was obtained by choosing a maximally compressed Akhmediev breather as initial condition (Eq. 6.4). By looking at this graph, one can distinguish three input-power dependent regions with different soliton behaviour, namely 0.03 W $\leq P_0 <$ 0.54 W, 0.54 W $\leq P_0 <$ 2.3 W, and $P_0 \geq$ 2.3 W.

In the low input-power region, i.e. for 0.03 W $\leq P_0 <$ 0.54 W, three branches $C1$, $C2$, and $C3$ are noticeable. Unfortunately, those are not well resolved. To increase the resolution of the power spectrum, we performe the SRBA for the total fibre length of $L^A = 50$ km and the input power 0.01 W $\leq P_0 \leq$ 1.0W in steps of $\Delta P_0 = 0.01$ W (Fig. 6.8). This is done because the resolution of spectral-power plots within the SRBA strongly depends on the total fibre length chosen for simulation. More precisely, the resolution goes with $1/L^A$ [108, 113].

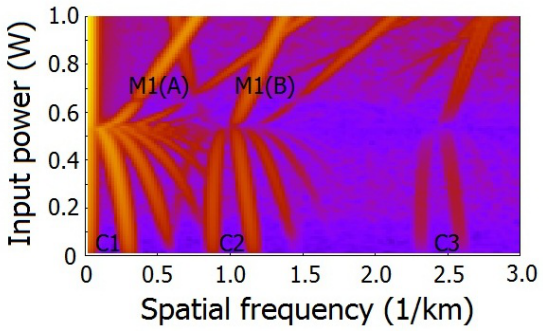

Figure 6.8: Spectral power for a maximally compressed Akhmediev breather as initial condition and fibre length $L^A = 50$ km for different values of the input power P_0 [111]

In the more detailed Fig. 6.8, one can see that there is no thereshold of the input power for the formation of the C-branches, i.e. the branches $C1$, $C2$, $C3$ and their overtones arise directly at $P_0 = 0$ W and $Z = 0.3$ km^{-1}, $Z = 1.2$ km^{-1}, and $Z = 2.6$ km^{-1}, respectively. As discussed previously, a power threshold is needed to form a soliton. In case of a maximally compressed Akhmediev breather as initial condition, a collective soliton state presented by the $C-$branches can be formed even at a very low input power, i.e. for $P_0 \to 0$ W. The reason for that is the following: a maximally compressed Akhmediev breather as initial condition delivers an infinite amount of energy for $t \to \pm\infty$ since it contains cos $-$functions in its definition (Eq. 6.4). A finite amount of the initial energy is delivered if the Akhmediev breather is truncated in time. This energy is used to built up the $C-$branches. By analogy to an electronic state in a crystal, the C-branches can be referred to as a collective soliton crystal state [111, 115].

For input powers $P_0 > 0.54$ W, we observe the emergence of significant branch groups that arise out of the branches $C1$, $C2$, and $C3$. To be precise, the branch $M1(A)$ originates from $C1$, $M1(B)$ from $C2$, and $M3$ from $C3$ (Fig. 6.7). The branches $M1(A)$ and $M1(B)$ merge as the value of P_0 increases. For the input powers $P_0 > 2.3$ W, we see the emergence of two soliton branches $S1$ and $S2$. Both solitons that are involved into the evolution of $S1$ and $S2$ have the soliton order $N = 1.13$ and, thus, constitute fundamental solitons. They are temporally well separated since their duration is small compared to their temporal separation (cf. Ref. [96]). In the region $P_0 < 2.3$ W, the soliton duration increases as the input power decreases [114]. Eventually, the solitons overlap temporally which makes their energies split having the emergence of branches $M1(A)$ and $M1(B)$ as a result [114]. So, we can regard the branches $M1(A)$ and $M1(B)$ as a common soliton molecule state in analogy to the energy splitting in molecules [88, 89, 90, 91, 92, 93]. The branch $|M1(B) - M1(B)|$ represents the mixing frequency between $M1(A)$ and $M1(B)$ [111].

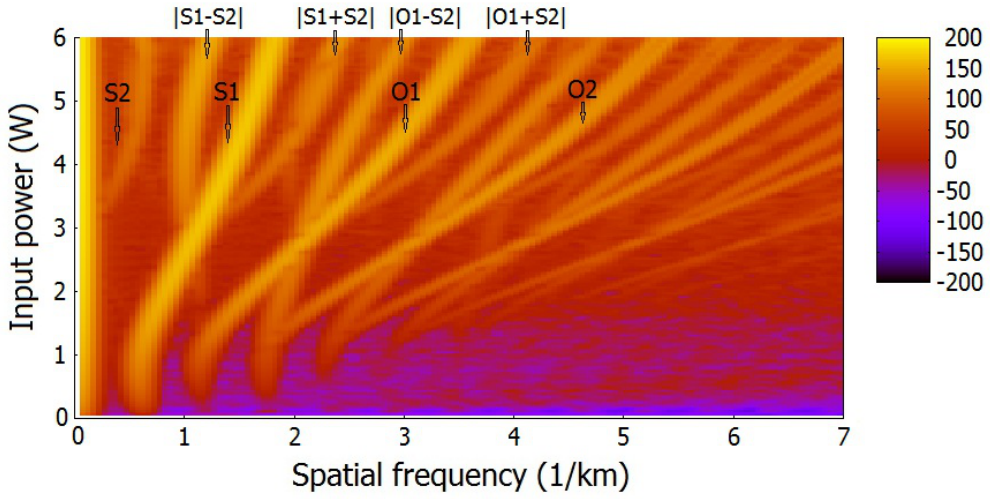

Figure 6.9: Spectral power for a deeply modulated cosine-wave as initial condition for different values of the input power P_0 according to the proposed setup for OFC generation. The chosen fibre length is $L^A = 20$ km [111]

Deeply-Modulated Bichromatic Cosine-Wave as Initial Condition

Fig. 6.5 shows the spectral power that was obtained using a deeply-modulated bichromatic cosine-wave as initial condition which corresponds to the initial condition of the system that we proposed for the generation of OFCs in fibres (Eq. 6.5). In this graph, the most incisive soliton branch $S1$ starts at $P_0 = 0$ W and $Z = 0.65$ km^{-1} meaning that no power thereshold was needed to built up this branch. The reason for that is the same as in case of the maximally compressed Akhmediev breather: the cosine in the definition of this initial condition provides an infinite amount of energy for $t \to \pm\infty$. This energy is used to form a collective soliton crystal state in the region 0 W $< P_0 < 1.3$ W.

In case of a maximally compressed Akhmediev breather as initial condition, the input-power region of the collective crystal state was separated from the molecule-state region at $P_0 = 0.54$ W. In case of a bichromatic cosine-wave as intial condition, the region of the molecule state is missing, the transition from the soliton crystal to a state of well-separated solitons occurs continuously. This is indicated by a smooth evolution of the $S1$-branch as the value of the input power increases. The order of the soliton that is involved into the emergence of branch $S1$ is $N = 0.85$ (calculated at $P_0 = 1.3$ W). This is the order of a fundamental soliton.

At $P_0 = 3.3$ W and $Z = 0$ km^{-1}, we observe the emergence of a second soliton branch $S2$. It shows the behaviour of a single soliton beating with the background. The order of this soltion is $N = 1.35$ meaning that $S2$ represents another fundamental soliton.

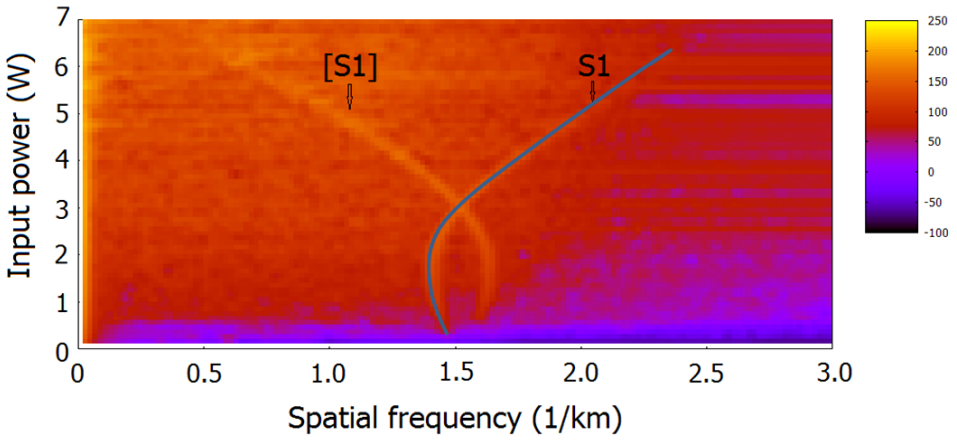

Figure 6.10: Spectral power for a deeply modulated cosine-wave as initial condition for different values of the input power P_0 according to the proposed setup for OFC generation. The chosen fibre length is $L^A = 50$ km and the initial laser frequency separation $LFS = 125$ GHz

The branches $O1$ at $P_0 = 0$ W and $Z = 1.2$ km^{-1} and $O2$ at $P_0 = 0$ W and $Z = 1.8$ km^{-1} are the overtones of $S1$, whereas the branches $|S1 - S2|$, $|S1 + S2|$, $|O1 - S2|$, and $|O1 + S2|$ constitute the frequencies emerged from the beating of solitons with each other or from the beating between the solitons and their overtones [111].

To prove that the appearance of such mixed soliton behaviour is not a result of numerical errors, we perform the SRBA for two additional values of laser frequency separation, namely for $LFS = 125$ GHz and $LFS = 160$ GHz. The total fiber length is now chosen to be $L^A = 50$ km sampled with $M = 50000$ points. The apodisation strength is given by $b = 0.3$. The input power increases from $P_0 = 0.1$ W to $P_0 = 7.0$ W in steps of $\Delta P_0 = 0.1$ W. The fibre parameters remain the same as previously.

Fig. 6.10 and Fig. 6.11 show the spectral power depending on the spatial frequency and the input power for $LFS = 125$ GHz and $LSF = 160$ GHz, respectively. In both graphs, we observe the appearance of branches $S1$ that constitute the beating of a soliton and the dispersive-wave background. Since these branches were hardly visible in the graphs, we emphasised them by the dark lines.

For $LFS = 125$ GHz, $S1$ starts at $P_0 = 0$ W and $Z = 1.5$ km^{-1}. In case of $LFS = 160$ GHz, $S1$ begins at $P_0 = 0$ W and $Z = 2.3$ km^{-1}. In the low input-power region, the curves go to the lower spatial frequecies as P_0 increases for both, $LFS = 125$ GHz and $LFS = 160$ GHz, following the pattern that is presented by $C-$branches for the case when an Akhmediev breather was chosen as initial condition. In this region, the branches $S1$ represent soliton crystal states. The decrease of the spatial frequency in the low input-power region is, actually, also given in case when a bichromatic deeply-modulated cosine-wave with

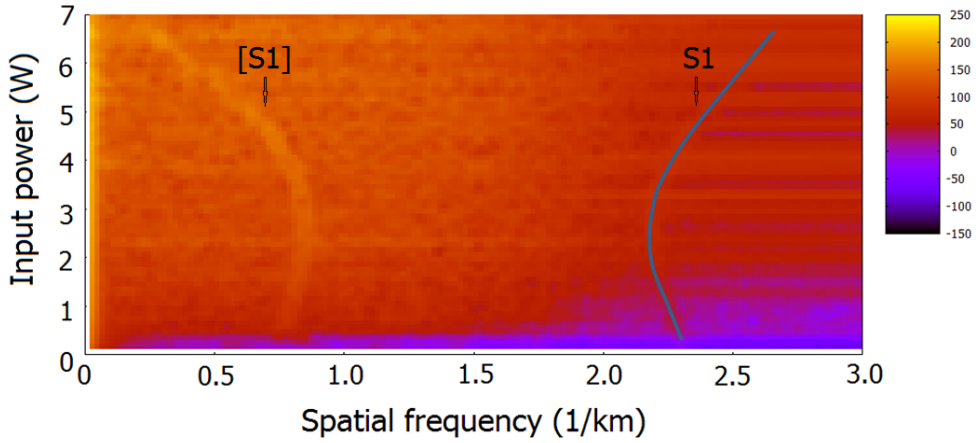

Figure 6.11: Spectral power for a bichromatic deeply-modulated cosine-wave as initial condition for different values of the input power P_0 according to the proposed setup for OFC generation. The chosen fibre length is $L^A = 50$ km and the initial laser frequency separation $LFS = 160$ GHz

$LFS = 80$ GHz was used as initial condition. Unfortunately, this effect is hardly visible due to the lower spatial resolution (Fig. 6.9).

Again, the transition from a soliton crystal state to the state of well-separated solitons occurs continously for both, $LFS = 125$ GHz and $LFS = 160$ GHz. The order of the soliton that is involved into the evolution of $S1$ is $N = 0.78$ (calculated at $P_0 = 2.8$ W) for $LFS = 125$ GHz and $N = 0.71$ (calculated at $P_0 = 3.8$ W) for $LFS = 160$ GHz. So, $S1$ constitutes the beating of a fundamental soliton with the dispersive-waves background in both cases.

In both graphs, we also see the branches $[S1]$ that can be interpreted as reflections of the branches $S1$. They arise due to the undersamping of our data: the number of the output spectra over the propagation distance calculated by means of the RK4IP and subsequently sampled (better to say interpolated) by $M = 50000$ equidistantly positioned points is not sufficient, it only amounts to 150 for the graphs in Fig. 6.10 and Fig. 6.11. This problem can be easily solved by increasing the number of the output spectra to a higher value. Figs. 6.6-6.9, for example, were produced using 500 output spectra sampled by $M = 20000$ points. Apparently, these graphs do not exhibit the branch reflections in the considered spatial-frequency region [113].

6.3 Conclusion and Discussion

Let us now summarise the achieved results. First, in Sec. 6.1, we showed that the first fibre stage (fibre A) of the proposed system for generation of optical frequency combs

allows formation of Akhmediev breathers or optical structures that are similar to them.

Then, in Sec. 6.2.3, we studied the formation of solitons in fibre A when a bichromatic cosine-wave is chosen as initial condition by comparison of its SRBA result with the SRBA results of well-known cases when a single-cosine hump and an Akhmediev breather are used as initial condition. As we used a single cosine-hump as initial condition, we observed the emergence of the first fundamental soliton at $P_0 = 0.7$ W and of the second one at $P_0 = 3.3$ W. For a maximally compressed Akhmediev breather as initial condition, we identified three input-power dependent regions in which different kinds of solitons had arisen. Thus, for input powers $0.03\,\text{W} \leq P_0 < 0.54\,\text{W}$, we observed the formation of a (collective) soliton crystal. For $0.54\ \text{W} < P_0 < 2.3$ W, the soliton crystal dissolved into a soliton molecule. For $P_0 > 2.3$ W, two fundamental solitons arose. Note, the regime transition between the state of a soliton crystal and a soliton molecule occurs at $P_0 = 0.54$ W, whereas the transition between the molecule state and the state of free (fundamental) solitons takes place at $P_0 = 2.3$ W.

The case we are interested in the most, namely the deeply modulated cosine-wave as initial condition, has shown the following features:

- we observe a collective soliton crystal state for $P_0 \to 0$ W which is similar to the case when an Akhmediev breather is chosen as initial condition
- contrary to the case of an Akhmediev breather, the input-power region where soliton molecules are formed is missing. Instead, the soliton crystal dissolves into the state of free (fundamental) solitons as the value of P_0 increases. The free solitons exhibit similar behaviour as in the case of a single cosine-hump as intitial condition. Note that the regime transition between the soliton crystal state and the state of free solitons occurs continuously in the input-power region $1.0\ \text{W} < P_0 < 2.0$ W.
- the continuous regime transition from a soliton crystal to the state of well-separated solitons was observed for three values of the initial laser frequency separation, $LSF = 80$ GHz, $LSF = 125$ GHz, and $LSF = 160$ GHz.

In other words, our system generates pulses that show features of Akhmediev breathers for low input powers and free solitons for higher input powers.

To achive a best possible OFC and to be able to control it, we need pulses that are temporally and spectrally periodic. The first option to have temporally periodic structures is to generate higher-order solitons in fibre A which might be achievable for high input powers using a bichromatic deeply modulated cosine-wave. In this case, however, it is highly possible that the pulses would break up which would drastically increase the intensity noise of the whole system. Moreover, after the fission the soliton components will have different centroids as the mother-soliton before the break-up which would lead to the increase of the timing jitter. However, the level of both, the intensity noise

and timing jitter, should be kept as low as possible to achieve a stable and low-noise OFC suitable for astronomical applications.

One also could go to another limit and generate pulses in the low input-power regime ($P_0 \rightarrow 0$ W) where the pulses have many similarities to the temporally periodic Akhmediev breathers. However, this would not be efficient since the input power would be too low to induce a sufficient level of fibre nonlinearity. The latter one, however, drives the FWM process. In case of $P_0 \rightarrow 0$ W, the OFC would have narrow bandwidths unsatisfactory for the requirements in the Astronomy.

Of course, one also could use proper Akhmediev breathers as initial condition and not a deeply modulated cosine-wave as we proposed. To do so within the framework of the proposed setup (Sec. 2.2), one would need to minimise the power of the second (tuneable) laser to a fraction of the power of the first (fixed) laser or vice versa. In this case, however, a great amount of the energy that gets provided by the lasers would get lost into the background on which the pulses would sit. Again, this would negatively affect the OFC bandwidth. Moreover, Akhmediev breathers have complex dymanics. In the studied case, there are many frequencies additional to the actual free-soliton branches S1 and S2 as shown in Fig. 6.7. The optical pulses that contain these additional frequencies sensitive even to small perturbations and tend to break up which would yield the increase of the system intensity noise.

Using a bichromatic cosine-wave as initial condition as we proposed in here, one would achieve best possible OFC spectra after fibre A for 2 W $< P_0 <$ 3.5 W (LFS = 80 GHz), 3.5 W $< P_0 <$ 6 W (LFS = 125 GHz), and 4 W $< P_0 <$ 7 W (LFS = 160 GHz). In these input-power regions,

- only fundamental solitons are generated and, so, there is no danger of soliton fission
- the temporal and spatial periodicity coming from the soliton crystal state is still imprinted into the pulses' features
- the pedestal content that we will discuss in the following sections is still low and, thus, a low amount of energy is lost into the pedestals.

To achieve a better understanding of the pulse build-up in fibre A, one should perform the SRBA for different fiber parameters (GVD β_2^A and the nonlinearity γ^A) to see if the change of these parameters might affect the pulse build-up and, thus, the OFC quality.

For the SRBA studies in this section, we excluded the optical fibre losses from consideration. However, even a typical fibre loss of 0.2 dB/km might affect the soliton dynamics in fibre A, especially, in the low input-power region. For instance, it is expected that the soliton oscillations would slow down with increasing propagation

length due to the energy loss [116]. It is also questionable if a soliton crystal state in the low input-power region exists in the presence of an optical loss. Thus, to be aware of the effect of optical losses, one needs to include them into the mathematical model and repeat the SRBA.

7 Pulse Build-up in the Second Fibre Stage

In Sec. 6, we discussed the optical pulse formation in the first fibre stage of the proposed setup for generation of OFC (Sec. 2.2) for different initial conditions (single cosine-hump, Akhmediev breather, bichromatic deeply modulated cosine-wave) for a fixed laser frequency separation of $LFS = 80$ GHz. In case when a bichromatic cosine-wave is chosen as IC, we also investigated the pulse build-up for $LFS = 125$ GHz and $LFS = 160$ GHz. The most interesting object for studies is, however, the second fibre stage within the proposed setup, i.e. the Erbium-doped fibre. In this fibre, the optical pulses formed in the first fibre stage are amplified due to the Erbium amplification process. Their intensities invoke a strong nonlinearity that induces a strong pulse compression. For example, the pulse widths are in the picosecond-range after the propagation through fibre A in case when a bichromatic cosine-wave is chosen as IC. After fibre B, the pulses are compressed down to a few tens of femtoseconds. Such strong pulse compression leads to the formation of a broadband OFC.

7.1 Methods

To study the pulse build-up in the second fibre stage, we again make use of the SRBA technique. However, a detailed analysis is difficult since the calculation time for the second fibre drasticaly increases with the input power, the total fibre length as well as with the number of the time sampling points. Thus, a balance needs to be found between the sufficiency of the SRBA data (the resolution of the SRBA graphs depends on the the total fibre length) and the calculation time. To do so, we will generate data for three graphs depending on the input power: for the system input power $0.1\ \text{W} \leq P_0 \leq 2.0\ \text{W}$, the total fibre length will be $L^B = 40$ m sampled with $M = 4000$ distance sampling points, for $2.1\ \text{W} \leq P_0 \leq 4.0\ \text{W}$, the length is $L^B = 35$ m sampled with $M = 3500$ points, and for $4.1\ \text{W} \leq P_0 \leq 7.0\ \text{W}$, $L^B = 30$ m sampled with $M = 3000$ points. The input power will be changed in steps of $\Delta P_0 = 0.1$ W. The fibre parameters are: $\beta_2^B = -14\ \text{ps}^2/\text{km}$, $\beta_2^B = 0.1\ \text{ps}^3/\text{km}$, and $\gamma^B = 2.5\ \text{W}^{-1}\text{km}^1$. The optical losses are set to zero, i.e. $\alpha^B = 0$ dB/km for the sake of simplicity. The SRBA will be peformed for the values of initial laser frequency separation, $LFS = 80$ GHz and $LFS = 160$ GHz, in a time window of 128 ps sampled with 2^{14} time points.

The initial condition for the second fibre B is prepared as follows: as the optical pulses

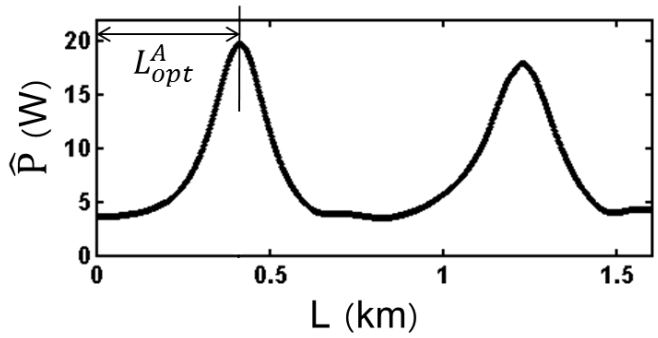

Figure 7.1: Definition of the optimum length of fibre A, L^A_{opt}, using an example with $P_0 = 3.5$ W and the initial laser frequency separation $LFS = 80$ GHz [40]

travel through fibre A, they undergo a periodic modulation of their intensities over the propagation distance (Fig. 7.1) if a bichromatic deeply modulated cosine-wave is chosen as IC for fibre A (Eq. 3.47). This modulation coincides with a periodic change of the temporal width: the pulse widths are minimal at the distance points where the pulse intensities are maximal. We define the optimum length of fibre A, L^A_{opt}, as the length from the beginning of the fibre until the point of the first pulse's intensity maximum. The optical pulses at the optimum length have a profile that is very close to a *sech*−profile of typical solitons (Fig. 7.2). So, we assume that almost perfect optical solitons are injected into the second amplifying fibre. The parameters of the first fibre are chosen to be: $\beta^A_2 = -15$ ps^2/km, $\beta^A_3 = 0.1$ ps^3/km, $\gamma^A = 2.0$ W^{-1}km^1, and $\alpha^A = 0$ dB/km.

7.2 Results

The Fig. 7.3 shows an example of the evolution of an IC prepared in fibre A. As can be seen, some additional peaks arise as the pulse propagates through the amplifying fibre B. This can be explained as follows: as the soliton with order $N = 1$ (Fig. 7.4) and chirped due to self-phase modulation propagates through the amplifying fibre B, it adiabatically tends to maintain its order by reducing its width (Eq. 4.4). Especially for higher-order solitons, this process is, however, non-adiabatic: a part of the pulse energy is shed into the dispersive waves that build up broad pulse pedestals. Due to the Erbium-gain and the instability of the background, parts of the dispersive waves can grow and evolve into additional chirped solitons. Each subsoliton, once it is stabilised, has nearly the same width and ca. the same amplitude. The spacing between the subsolitons changes during the formation of the subpulses, but becomes eventually nearly uniform. The chirped profiles of new solitons can overlap with each other or/and with the chirped profile of the main soliton. The interaction of chirped solitons via this overlap leads to oscillatory structures in the pulse spectra [46, 117].

Figs. 7.5-7.7 present the soliton radiation beat analysis for $LFS = 80$ GHz. As one can

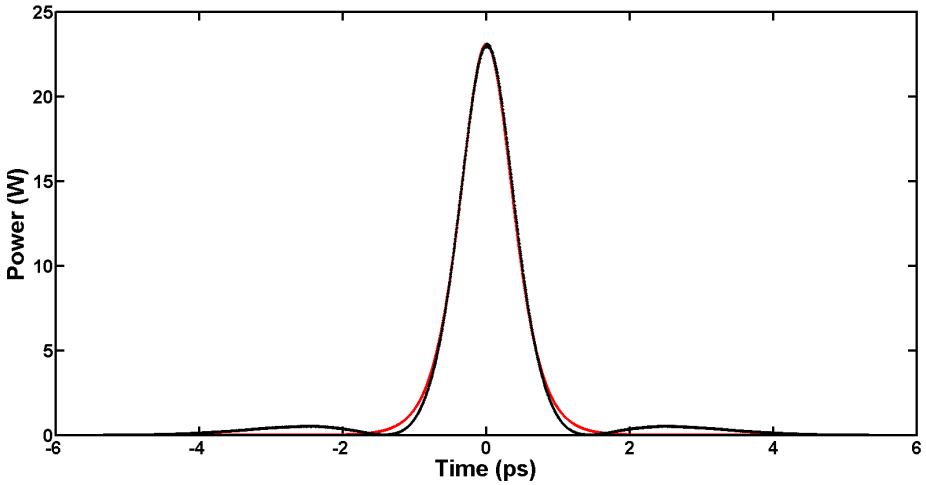

Figure 7.2: Temporal shape of a bichromatic pulse (black) after propagation in fibre A with the input power P_0 = 4.5 W and the initial laser frequency separation LFS = 80 GHz and the shape of a *sech*−pulse with the same pulse width and intensity (red)

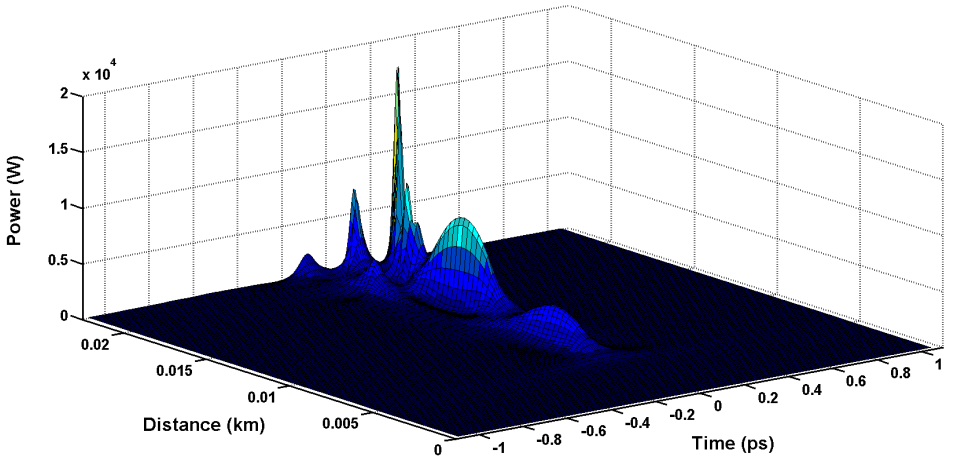

Figure 7.3: Example of the pulse evolution in fibre B for the input power P_0 = 4.5 W and the initial laser frequency separation LFS = 80 GHz

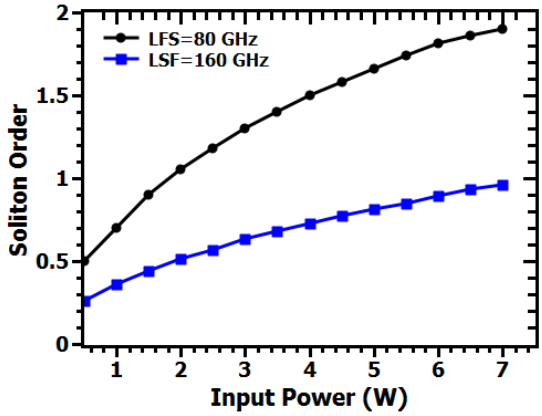

Figure 7.4: Soliton order of the pulses after the propagation through fibre A (corresponding to branches $S1$ in Fig. 6.9 and Fig. 6.11) for the initial laser frequency separation LFS = 80 GHz and LFS = 160 GHz calculated using Eq. 6.6

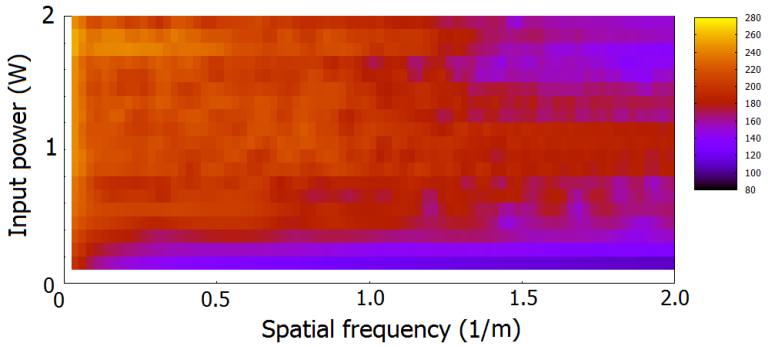

Figure 7.5: Spectral power in fibre B for the input powers 0.1 W $\leq P_0 \leq$ 2.0 W, the total fibre length L^B = 40 m, and the initial laser frequency separation LFS = 80 GHz

see, there are no visible branches in the SRBA-spectrum for input powers $P_0 < 2.8$ W (Fig. 7.5 and Fig. 7.6). In this input-power region, the soliton compression occurs adiabatically, that means the soliton maintains its order by reducing its pulse width. Although the soliton is not oscillating over the propagation distance, we still observe a spatial frequency continuum. This continum consists of many frequencies that arise due to the pulse amplification (a pulse oscillates faster and faster over the propagation distance as it gains energy due to the Erbium amplification).

The situation changes for input powers $P_0 > 2.8$ W. Already in fibre A, there appear mixing frequencies of two solitons ($|S1 - S2|$ and $|S1 + S2|$ in Fig. 6.9). The comparably high energy of the optical pulses in fibre A and the more complicated behaviour of them due to the appearance of mixing frequencies lead to the build-up of big pulse pedestals

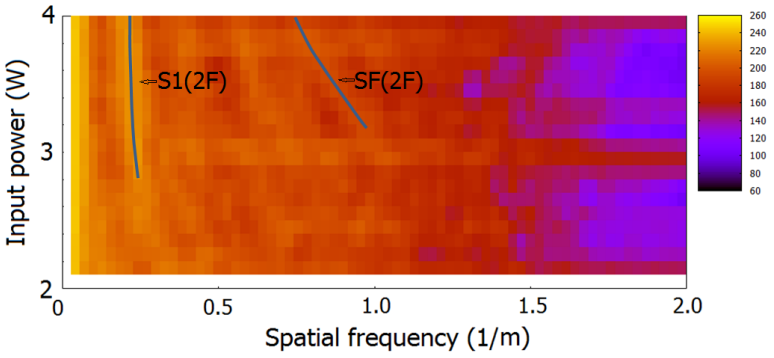

Figure 7.6: Spectral power in fibre B for the input powers 2.0 W $< P_0 \leq$ 4.0 W, the total fibre length L^B = 35 m, and the initial laser frequency separation LFS = 80 GHz

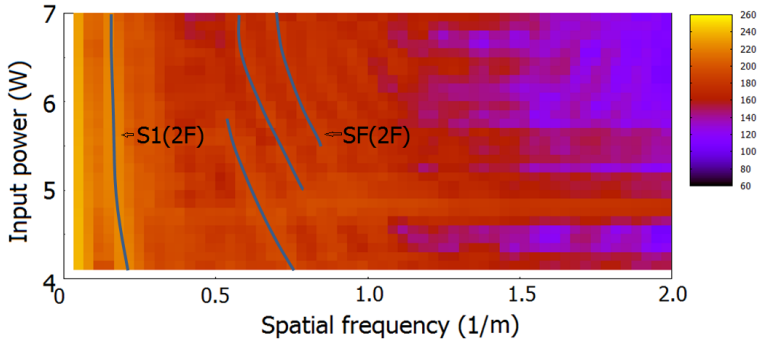

Figure 7.7: Spectral power in fibre B for the input powers 4.0 W $< P_0 \leq$ 7.0 W, the total fibre length L^B = 30 m, and the initial laser frequency separation LFS = 80 GHz

in fibre B which eventually ends up in the formation of additional subpulses. Such behaviour indicates the non-adiabatic higher-order soliton compression (Sec. 5). The branch $S1(2F)$ in Fig. 7.6 and Fig. 7.7 emerges due to the beating between the central soliton and the neighbouring subsolitons. The beating between the subsolitons with each other manifests itself in the branches that are all together referred to as $SF(2F)$. The number of the subpulses increases with the input power. Also the number of the branches $SF(2F)$ goes up with the value of P_0 : in Fig. 7.6, there is only one branch $SF(2F)$, whereas there are already three branches of that kind in Fig. 7.7.

Figs. 7.8-7.10 show the results of the soliton radiation beat analysis for the initial laser frequency separation of LFS = 160 GHz. For input powers $P_0 <$ 4.5 W, the solitons formed in fibre A propagate through fibre B adiabatically, they get amplified and well compressed at the same time. Some subpulses arise for higher values of P_0. Again, the

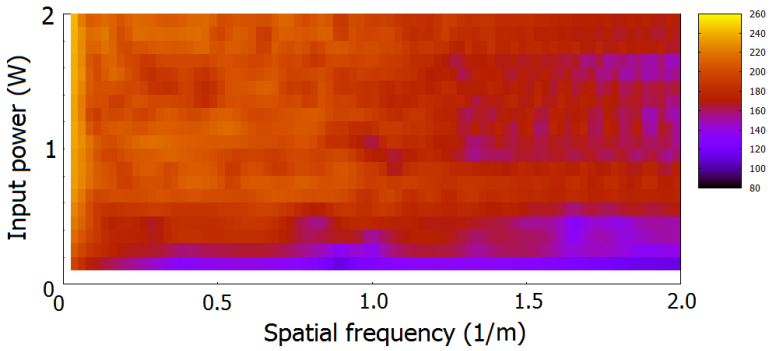

Figure 7.8: Spectral power in fibre B for the input powers 0.1 W $\leq P_0 \leq$ 2.0 W, the total fibre length L^B = 40 m, and the initial laser frequency separation LFS = 160 GHz

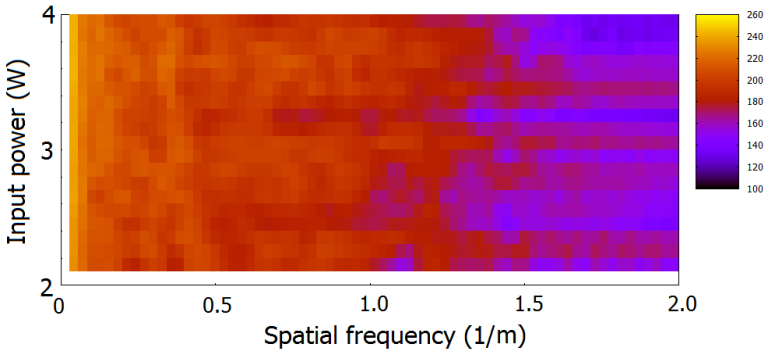

Figure 7.9: Spectral power in fibre B for the input powers 2.0 W $< P_0 \leq$ 4.0 W, the total fibre length L^B = 35 m, and the initial laser frequency separation LFS = 160 GHz

beating between the main soliton and the subpulses is represented by the branch $S1(2F)$ and the beating between the subsolitons is expressed by the branches $SF(2F)$ (Fig. 7.10).

7.3 Conclusion and Discussion

In this section, we considered the pulse build-up in the second (amplifying) fibre stage of our motivating setup for the initial laser frequency separation of LFS = 80 GHz and LFS = 160 GHz. Clearly, more detailed and better resolved SRBA-graphs are needed to get a deeper insight into the pulse behaviour in the Erbium-doped fibre. For that, longer propagation lengths need to be chosen as well as the input-power steps minimised.

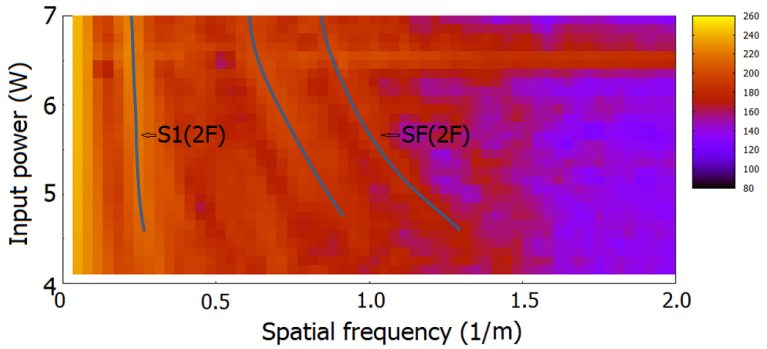

Figure 7.10: Spectral power in fibre B for the input powers 4.0 W $< P_0 \leq$ 7.0 W, the total fibre length L^B = 30 m, and the initial laser frequency separation LFS = 160 GHz

Further, the Erbium-amplification suffers from saturation [118, 119]. A more elaborated mathematical model including this important effect is required to describe the pulse evolution in fibre B in a more accurate way. This can be done by the extension of Eq. 3.46 by a saturable-absorber term [120, 121]. Actually, we have tried to do that, but, unfortunately, the inserting of such saturable-absorber term extremely increased the calculation time. So, we dropped it again for the efficiency's sake.

By setting $\alpha^B = 0$ dB/km, we have not included the impact of the optical losses on the SRBA-results. For the fibre lengths considered here, the neglection of the optical loss is justified. As already mentioned, more profound studies require longer propagation lengths for which the fibre losses should not be neglected anymore. Moreover, the implementation of the Erbium-saturation and the inclusion of optical losses into the model would lower the maximum peak power in fibre B. This might have a soliton compression as a (numerical) result that takes place more adiabatically than in the cases we considered here.

However, even using relatively poor data in this section, we have found that the pulse build-up in the amplifying stage of our setup critically depends on the features of the pulses formed in fibre A. So, adiabatic soliton compression occurs for low and medium vaues of the input power. In this region, the pulses formed after propagation through fibre A have low soliton orders and do not contain any additional mixing frequencies. For high values of the input power, however, the pulses after fibre A have more complicated structure featuring higher soliton orders or containing mixing frequencies. This has the emergence of subpulses in the amplifying fibre B as a result. The pulse compression process takes place non-adiabatically. The appearance of the additional pulses can also be considered as soliton fission and should be prevented since it increases the level of the intensity noise and degrades the OFC quality. The soliton fission occurs for input power values $P >$ 2.8 W for LFS = 80 GHz and $P >$ 4.5 W

for LFS = 160 GHz. According to the results obtained in this section and Sec. 6, the best optical frequency combs are expected to evolve in fibre B for the input powers 2.0 W < P_0 < 2.8 W for LFS = 80 GHz and 4.0 W < P_0 < 4.5 W for LFS = 160 GHz.

8 Optimum Lengths of the First and Second Fibres

After we considered the pulse build-up in fibres A and B of our motivating setup (Sec. 2.2) in Sec. 6 and Sec. 7, we now take a look at more practical issues. In this chapter, we focus our attention on the optimisation of fibre lengths of the first two stages.

The actual aim of the propagation of the initial deeply-modulated bichromatic field through fibre A and B is to generate maximally compressed pulses that exhibit minimum level of intensity noise (*IN*). Such pulses would provide us with maximally broad OFC that are hardly affected by noise. As the optical pulses propagate through fibre A, they experience a periodical modulation of their intensity over the propagation distance. This modulation occurs due to the formation and the subsequent propagation of optical solitons as described in Sec. 6. In fibre B, the changes in the pulse intensity result from the radiation of the pulse energy into the dispersive-wave background and a subsequent emergence of subpulses (Sec. 7). The optimum length of a fibre, L_{opt}, is defined as the propagation distance from the beginning of the fibre and the first pulse intensity maximum. At the optimum length, the pulses are maximally compressed and exhibit a minimum of *IN* (Fig. 8.1 and Fig. 8.2) [40]. Specifically in fibre B, the optimum length denotes the point from which on the formation of the subpulses begins.

The optimisation studies will be performed assuming negligible optical losses in both fibres, i.e. $\alpha^A = 0$ dB/km and $\alpha^B = 0$ dB/km (Eq. 3.46). After we calculate the optimum lengths, we will show that this assumption is valid and the inclusion of the optical losses does not change the system performance significantly for the considered optimum lengths since they are too short to let the optical absorption to play a role. For the sake of simplicity, we set the amplitude of the initial noise to zero, i.e. $n_0 = 0$ in Eq. 3.47 The optimisation studies are done in a time window of 256 ps sampled with 2^{16} time points. We calculate the optimum lengths of fibre A and B for different parameters of the GVD parameter of fibre A, β_2^A, and the different values of the initial laser frequency separation *LFS*. This is done because these parameters are easily changed within a real experiment.

8.1 Optimum Lengths for Different Values of β_2^A

Fig. 8.3 shows how the optimum lengths for fibre A (L_{opt}^A) and B (L_{opt}^B) depend on the initial laser power P_0 and three different values of the anomalous GVD parameter of

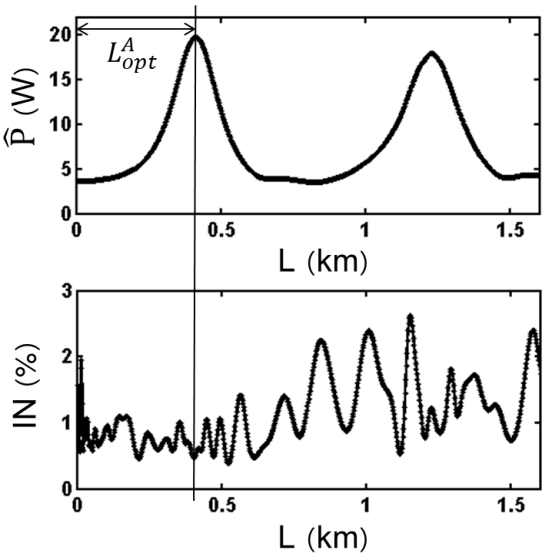

Figure 8.1: Peak power in W (upper graph) and intensity noise in % (lower graph) vs. propagation distance in km for fibre A [40]

fibre A, i.e. $\beta_2^A = -7.5$ ps^2/km, $\beta_2^A = -15$ ps^2/km, and $\beta_2^A = -30$ ps^2/km. The TOD parameter is $\beta_3^A = 0.1$ ps^3/km the nonlinear parameter is chosen to be $\gamma^A = 2\,\mathrm{W}^{-1}\mathrm{km}^{-1}$. These are the standard values for single-mode fibres [10, 122, 123].

As seen in Fig. 8.3, there is a plateau at low values of P_0, where the optimum lengths of fiber A are constant for each given value of the GVD parameter β_2^A. For these input-power values, a collective soliton crystal state is formed in fibre A (cf. Sec. 6). In this case, there is no well-defined optimum length L^A_{opt}, any fibre length can be used within an experiment. The edge of each plateau corresponds to an input-power value from which the formation of separated solitons starts in fibre A. For the input powers beyond the plateau region, the value of L^A_{opt} decreases as P_0 increases. This is because the soliton order N (Eq. 6.6) increases with the input power. For increasing soliton orders, the lengths of soliton cicles decrease and, so, the optimum lengths [114].

However, there is a strange behaviour of solitons in fibre A that we cannot explain at this moment. The soliton order also depends on the value of β_2^A not only on the value of P_0 (Eq. 6.6). If we calculate the order, for instance, at $P_0 = 5$ W, we get the following values: $N^A = 2.3$ for $\beta_2^A = -7.5$ ps^2/km, $N^A = 1.6$ for $\beta_2^A = -15$ ps^2/km, and $N^A = 1.15$ for $\beta_2^A = -30$ ps^2/km. That means that, for a specific value of P_0, the optimum lengths L^A_{opt} decreases with the soliton number, although it should be the other way around. To understand this behaviour, more detailed studies are required.

The optimum lengths of fibre B decrease for increasing input powers which is the

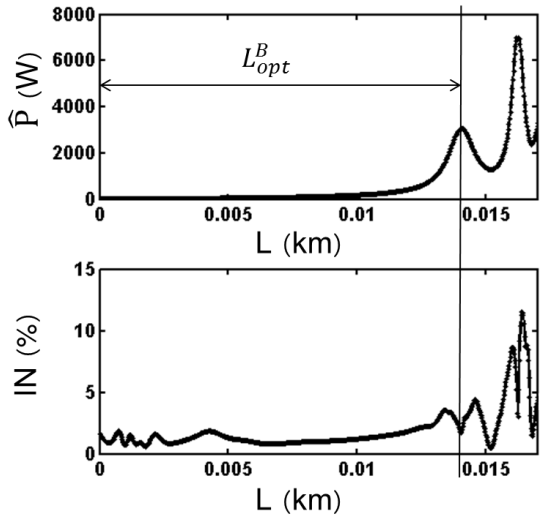

Figure 8.2: Peak power in W (upper graph) and intensity noise in % (lower graph) vs. propagation distance in km for fibre B [40]

result of the formation and the propagation of higher-order solitons in fibre A: the cycle of solitons with higher orders evolves over shorter distances also in fibre B meaning that a soliton with a higher order would be compressed on a shorter optimum length. For $P_0 \leq 4.5$ W, the value of the optimum length L^B_{opt} decreases with the decreasing absolute value of β_2^A suiting perfectly into the scheme of the higher-soliton compression.

At $P_0 = 4.5$ W, it comes to a crossing between the curves for $\beta_2^A = -7.5$ ps^2/km and $\beta_2^A = -15$ ps^2/km. The crossing of the curve for $\beta_2^A = -7.5$ ps^2/km with the curve for $\beta_2^A = -30$ ps^2/km occurs at $P_0 = 6.5$ W. This crossing is the result of the L^B_{opt}−saturation whereas the other curves still decrease with the increasing input power. The appearance of such saturation is probably connected with the spectral evolution of the pulses in fibre A. At the moment, however, the pulse build-up in fibre A is not fully understood. Therefore, we cannot explain why the optimum-lentgh decrease saturates in fibre B [40].

8.2 Optimum Lengths for Different Values of *LFS*

Now we set the GVD of fibre A to $\beta_2^A = -15$ ps^2/km and the nonlinear parameter to $\gamma^A = 2$ W^{-1}km^{-1}, and study the dependence of optimum lengths on the initial laser frequency separation (see Fig. 8.4). We choose *LFS* = 40 GHz, *LFS* = 80 GHz, and *LFS* = 160 GHz.

Again, we observe plateaus of L^A_{opt} for low and medium input powers that coincide to the formation and the subsequent propagation of soliton crystal states in fibre A (Fig. 8.4). After the plateau ends, which corresponds to the formation of separated soli-

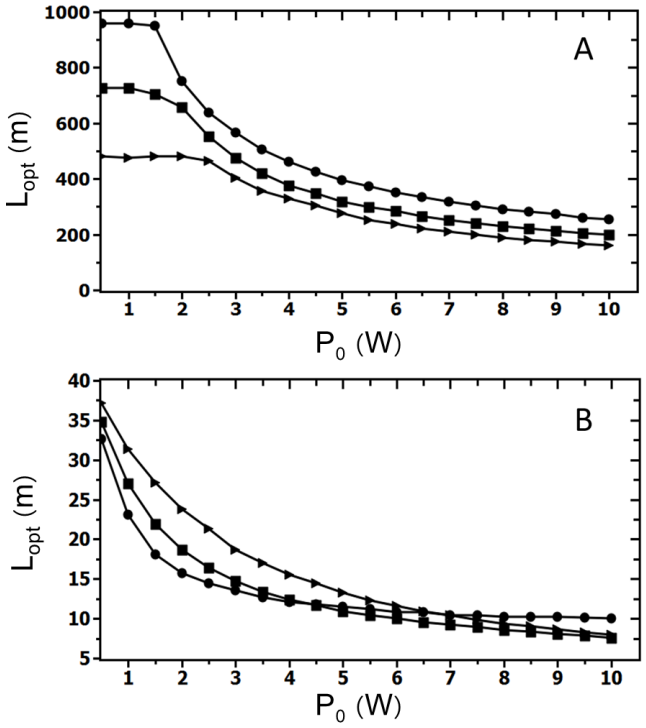

Figure 8.3: Optimum lengths of fibres A and B, L^A_{opt} and L^B_{opt}, in m vs. input power P_0 in W for different values of the GVD parameter of fibre A: $\beta^A_2 = -7.5$ ps^2/km (circles), $\beta^A_2 = -15$ ps^2/km (rectangles), and $\beta^A_2 = -30$ ps^2/km (triangles) [40]

tons, the optimum lengths L^A_{opt} decrease with the input power due to the increase of the soliton order with P_0. However, there appear, again, a disagreement with expectations for a fixed value of P_0, but different values of *LFS*: the optimum lengths decrease as the *LFS* increases, i.e. as the soliton order decreases, although it should be vice versa [114, 45]. For $P_0 = 5$ W, the soliton orders are the following: $N^A = 3.2$ for *LFS* = 40 GHz, $N^A = 1.6$ for *LFS* = 80 GHz, and $N^A = 0.81$ for *LFS* = 160 GHz.

The soliton-compression scheme works perfectly for fibre B: the optimum lengths L^B_{opt} decrease with the input power as well as with the order of solitons formed in fibre A [40].

8.3 Impact of the Optical Losses and the Characteristic Lengths L_D and L_{NL}

Previously, we peformed our studies assuming that the optical losses are negligible in fibre A and B and can be set to $\alpha^A = 0$ dB/km and $\alpha^B = 0$ dB/km, respectively. Now,

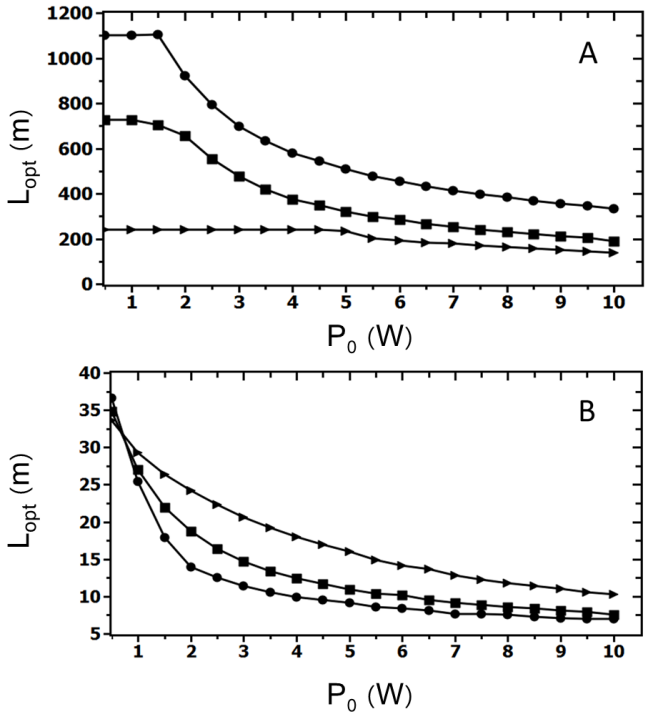

Figure 8.4: Optimum lengths of fibres A and B, L^A_{opt} and L^B_{opt}, in m vs. input power P_0 in W for different values of the initial laser frequency separation LFS : LFS = 40 GHz (circles), LFS = 80 GHz (rectangles), and LFS = 160 GHz (triangles) [40]

using one specific example, we want to show that this assumption is correct since the considered propagation lengths, L^A_{opt} and L^B_{opt}, are too short to let optical absorption to change the system behaviour in an appreciable way. Moreover, we compare the optimum lengths with the characteristic nonlinear (L_{NL}) and dispersion (L_D) lengths. The nonlinear length for fibre A is defined as follows:

$$L^A_{NL} = \frac{1}{P_0 \gamma^A}, \tag{8.1}$$

whereas for fibre B as

$$L^B_{NL} = \frac{1}{\hat{P} \gamma^B} \tag{8.2}$$

with $\hat{P}$ denoting the peak power of pulses after they propagated through fibre A [45, 46]. The dispersion length of fibre B obeys the classic definition:

$$L^B_D = \frac{(T^A_0)^2}{|\beta^B_2|}, \tag{8.3}$$

where T_0^A is the natural width of pulses after they propagated through fibre A. It is obtained via the determination of the FWHM and the expression $T_0^A \approx T_{\mathrm{FWHM}}^A/1.763$ being valid for solitonic structures [45, 46]. This definition is valid for chirp-free optical pulses with well-formed spectra which contain many lines. The initial spectrum, however, has only two frequency lines. Thus, the expression for the dispersion length of fibre A needs to be written as

$$L_D^A = \frac{1}{(2\pi LFS)^2 |\beta_2^A|} \tag{8.4}$$

with *LFS* denoting, as previously, the initial laser frequency separation [113, 40].

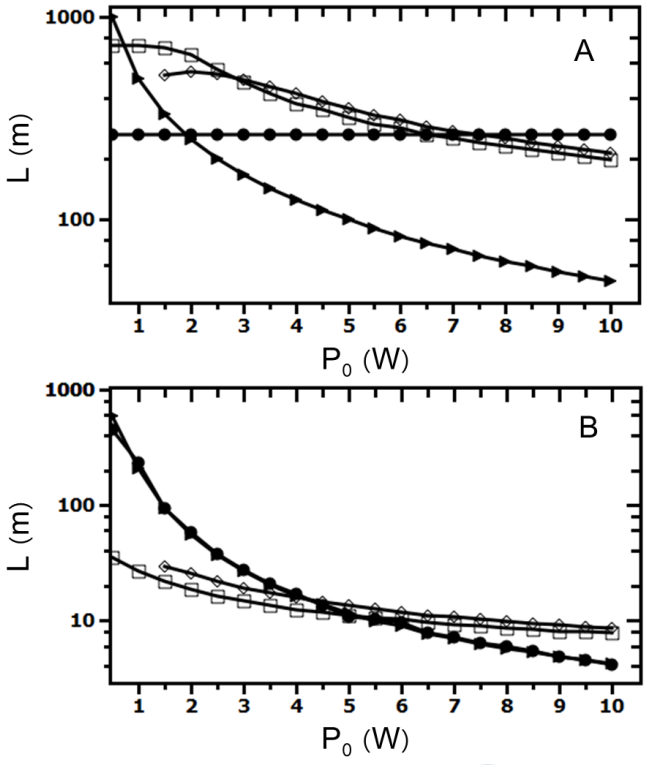

Figure 8.5: Optimum lengths with and without optical losses of fibres A and B, $L_{opt/\alpha}^A$, $L_{opt/\alpha}^B$ (diamonds), and L_{opt}^A, L_{opt}^B (rectangles) in comparison with characteristic lengths, L_D^A, L_D^B (circles), and L_{NL}^A, L_{NL}^B (triangles), in m vs. input power P_0 in W.

In this section, we use the following parameters for our studies: $\beta_2^A = -15$ ps^2/km, $\gamma^A = 2$ W^{-1}km^{-1}, $LFS = 80$ GHz. As for the optical fibre losses, we set $\alpha = 0.2$ dB/km for both, fibre A and B, assuming that the Er-absorption in fibre B is compensated by the pump (see Fig. 2.1) and only optical absorption plays a role [45, 46].

As shown in Fig. 8.5, the difference between the optimum lengths for fibre A calculated with and without optical losses, i.e. $L^A_{opt/\alpha}$ and L^A_{opt}, is 0 m for $P_0 = 3.0$ W and 15 m for $P_0 = 10.0$ W. In this region, the pulse shapes and the OFC spectra are similar. So, the optical losses can be neglected for 3.0 W $< P_0 \leq$ 10.0 W. However, for $P_0 \leq 3.0$ W, the optical losses have influence on the formation of periodically modulated optical pulses and, thus, optimum lengths. This feature is crucial especially for $P_0 \leq 1.5$ W, where no opimum lengths $L^A_{opt/\alpha}$ are possible. For these input-power values, the pulse intensity decays exponentially due to the optical losses. This is, however, exactly the region where we observed the formation of an soliton crystal state (cf. Sec. 6.2.3). The absence of optimal lengths for $P_0 \leq 1.5$ W, makes us suspect that there is no soliton crystal states in the presence of optical losses. However, to be sure about it, one needs to perform further SRBA-studies that include the optical attenuation.

The nonlinear lengths of fibre A, L^A_{NL}, are shorter than the optimum lengths $L^A_{opt/\alpha}$ and L^A_{opt} for any input powers and shorter that the dispersion lengths L^A_D for $P_0 > 1.8$ W. If characteristic lengths are compared with each other, the shortest length denotes the dominating effect [113, 114]. That means that for input-power values $P_0 > 1.9$ W the fibre nonlinearity dominates the pulse dynamics in fibre A.

Both, $L^A_{opt/\alpha}$ and L^A_{opt}, are longer than the calculated dispersion length L^A_D for $P_0 < 6.5$ W and $P_0 < 7.5$ W, respectively. That means that the fibre dispersion has an important effect on the pulse dynamics in fibre A for this input powers, although not as important as the fibre nonlinearity for $P_0 > 1.9$ W. The dispersion becomes negligible as the lengths $L^A_{opt/\alpha}$ and L^A_{opt} get shorter than L^A_D for higher values of P_0.

For ca. $P_0 = 1.9$ W, the curve for L^A_{NL} crosses the curve for L^A_D denoting the point where the formation of a (fundamental) soliton with order $N = 1$ takes place (Eq. 4.4). At this point, the balance between the fibre nonlinearity and dispersion is established. Solitons with orders $N > 1$ are formed for higher values of the input power. This stands in a good agreement with our previous studies (Sec. 6.2.3).

In case of fibre B, the curve for L^B_{NL} overlaps with the curve for L^B_D, i.e. $L^B_{NL} = L^B_D$, for any values of P_0. That means that the optical pulses propagate as fundamental solitons through fibre B experiencing a balance between the nonlinearity and the dispersion regardless whether the pulse were formed as fundamental or higher-order solitons in fibre A. A part of the energy of the pulses that were formed as higher-order solitons in fibre A is radiated into the the pedestal background in fibre B so that only an amount of energy per pulse remains that is required to form a fundamental soliton.

As for the optimum lengths, they lie below the $L^B_{NL} - L^B_D -$ overlap for $P_0 = 4.0$ W ($L^B_{opt/\alpha}$) and $P_0 = 5.0$ W (L^B_{opt}), respectively. That means that both, the fibre group-velocity dispersion and the nonlinearity, have a negligible impact on the pulse dynamics in this input-power region. The situation changes for higher values of P_0 for which the opti-

mum lengths are longer than the characteristic nonlinear and dispersion lengths. Here, the influence of the fibre dispersion and nonlinearity is important. In this input-power region, the very high pulse peak powers induce a high level of fibre nonlinearity that drives the pulse compression which affects the dispersion length that depends on the pulse widths.

As for the inpact of the optical losses, the difference between $L^B_{opt/\alpha}$ and L^B_{opt} is 8 m for $P_0 = 3.0$ W and only 1 m for $P_0 = 10.0$ W. Again, the pulse shapes and the according OFC spectra have barely changed after we included optical losses into consideration. Therefore, we will proceed our studies assuming negligible optical losses, i.e. $\alpha^A = 0$ dB/km and $\alpha^B = 0$ dB/km.

8.4 Conclusion and Discussion

In this section, we calculated the optimum lengths for fibre A and fibre B of our motivating setup (Sec. 2.2) for different values of the GVD parameter β_2^A of fibre A and different values of the initial laser separation *LFS*. Having excluded the optical losses, we found that the optimum lengths of fibre A vary in the range of 180 m $< L^A_{opt} <$ 980 m depending on the initial power P_0 and the GVD parameter β_2^A. The corresponding optimum lengths of fibre B take the values of 7.5 m $< L^B_{opt} <$ 37.5 m. For different values of *LFS* and P_0, the optimum lengths were 150 m $< L^A_{opt} <$ 1100 m for fibre A and 7 m $< L^A_{opt} <$ 35 m for fibre B.

The best system performance in terms of optimum lengths was shown for $\beta_2^A = -15$ ps^2/km and $LSF = 80$ GHz. Using these values, we showed that typical optical fibre losses of $\alpha^A = 0.2$ dB/km can be neglected for $P_0 > 3.0$ W since they do not change the system behaviour in a significant way. The optimum lengths for fibre A that are calculated with optical losses are equal to the optimum lengths calculated without the losses for $P_0 = 3.0$ W and are only 15 m longer for $P_0 = 10.0$ W. In case of fibre B, the difference between $L^B_{opt/\alpha}$ and L^B_{opt} is 8 m for $P_0 = 3.0$ W and only 1 m for $P_0 = 10.0$ W.

The situation changes, however, in the input-power region $P_0 \leq 3.0$ W in which the optical losses have an impact on the formation of optical pulses in fibre A. Especially for $P_0 \leq 1.5$ W, the formation of temporally periodic optical pulses and, thus, of optical lengths of fibre A and B is not possible due to the influence of the optical attenuation. In Sec. 6, we observed the build-up of a soliton crystal state in this input-power region. Now, due to the absence of optical lengths, we suspect that the formation of a soliton crystal is not possible due to the influence of the optical losses.

In Sec. 7, we identified the input-power region 2.0 W $< P_0 <$ 2.8 W as one in which the best possible OFC spectra are expected. These results were obtained without taking the optical losses into account. Now, as we see that the optical attenuation has an impact on

the pulse formation in fibre A for $P_0 \leq 3.0$ W, we need to state that some more extended SRBA studies including the optical losses are required to thoroughly understand the formation of optical pulses in fibre A for low input-powers.

Having compared the characteristic lengths for the case when $\beta_2^A = -15$ ps^2/km and $LSF = 80$ GHz, we found that the nonlinearity has the dominating effect on the pulse dynamics in fibre A. In fibre B, the optical pulses propagate as fundamental solitons for any values of P_0 no matter if they were formed as fundamental or higher-order solitons in fibre A. For low input-powers, neither the nonlinearity nor the dispersion has a significant effect on the pulse dynamics in fibre B. For $P_0 > 4.5$ W, the interplay of the group-velocity dispersion and the nonlinearity plays a crucial role in the pulse evolution in fibre B.

9 Pulse Compression Effectiveness in the First and Second Fibre

As briefly discussed in Sec. 5, during the process of pulse compression, a part of the pulse energy is radiated into an undesired pedestal (Fig. 5.1). Especially in case of higher-order soliton compression in amplifying or dispersion-decreasing fibres, the loss of the pulse energy into the pedestal can go up to 80% [101, 102, 103]. This causes a reduction of the pulse peak power which leads to the degradation of the pulse compression and, so, the evolution of a broad OFC. Further, the pulse and pedestal interaction can be amplified in fibre B which might result in the increase of the noise level due to the pulse or pedestal break-up. Therefore, to achieve broad and low-noise OFC, it is advisable to keep the pulse pedestal as small as possible.

We can calculate the pedestal energy content as the relative difference between the total energy of one single pulse and the energy of an approximating soliton sech-profile with the same peak power and the FWHM as it has the pulse itself (cf. Fig. 7.2) [102, 103, 40]:

$$PED = \frac{|E_{\text{total}} - E_{\text{sech}}|}{E_{\text{sech}}} \cdot 100\%, \tag{9.1}$$

where

$$E_{\text{sech}} = 2\hat{P}\frac{T_{FWHM}}{1.763} \tag{9.2}$$

with $\hat{P}$ being the peak power of the sech-profile soliton.

To describe the amount of energy that remains in the pulse and does not get radiated into the pedestal, we introduce a figure of merit that is defined as:

$$FoM = \frac{\text{Pulse peak power}}{\text{Pulse average power}}. \tag{9.3}$$

The maximum value of FoM will correspond to the best-quality optical pulses and, thus, best-possible OFC.

The pulse compression effectiveness is described by the compression factor C that is given by:

$$C = \frac{T_{FWHM}(z = 0)}{T_{FWHM}(z = L_{opt})} \tag{9.4}$$

with L_{opt} being the optimum length of fibre A or B, respectively (cf. Sec. 8).

Considering three different values of the initial laser frequency separation, LFS = 40 GHz, LFS = 80 GHz, and LFS = 160 GHz, we address the following questions in this section:

- How does the pedestal content of pulses formed in fibre A and B depend on the the initial LFS and the initial input power P_0?
- How does the FoM of fibre A and B change with LFS and P_0?
- What are the compression factors C in fiber A and B for different values of LFS and P_0?

To carry out these studies, we choose the following parameters for fibre A: β_2^A = -15 ps^2/km, $\beta_3^A = 0.1$ ps^3/km, $\gamma^A = 2.0$ W^{-1}km^1, and $\alpha^A = 0$ dB/km. The parameters of fibre B are: $\beta_2^B = -14$ ps^2/km, $\beta_3^B = 0.1$ ps^3/km, $\gamma^B = 2.5$ W^{-1}km^1, and $\alpha^B = 0$ dB/km. The simulations are performed in a time window of 256 ps sampled with 2^{16} points using optimised fibre lengths.

The dependence of the FoM, PED, and C on different values of the GVD parameter of fibre A, β_2^A, is published in Ref. [40].

9.1 Results

Fig. 9.1 shows the pedestal content for fibre A and B. For fibre A, one can recognise the input-power regions in which the collective soliton crystal states are built for different values of LFS (cf. Sec. 6). Those are the regions where the respective $PED-$curves decrease with P_0 until they reach a minimum which is easily apparent specifically for LFS = 80 GHz (minimum at ca. P_0 = 1.5 W) and LFS = 160 GHz (minimum at ca. P_0 = 4.5 W). For LFS = 40 GHz, the soliton crystal is built for $P_0 < 1.0$ W. In the input-power regions of soliton crystals, the optical pulses have, actually, almost no visible pedestals. The $PED-$values going up to 15% (at P_0 = 0.5 W) come around because the pulse form of a soliton crystal component significantly differs from an ideal sech-profile typical for separated solitons. The minima in the $PED-$curves coincide with the P_0-values from which the formation of separated solitons is supported. The following applies for separated solitons in fibre A: the further the pulses are from each other in the time domain, i.e. the smaller the laser frequency separation, the higher is the pedestal content. Further, the value of PED increases with P_0 for any values of LFS. This is because the solion order increases with P_0 (according to Ref. [103], the pedestal content grows with the order of fibre solitons). In the input-power region 5.0 W $\leq P_0 \leq$ 10.0 W, the pulse pedestal content in fibre A varies between 40% and 55% for LFS = 40 GHz, between 13% and 28% for LFS = 80 GHz, and between 4% and 14% for LFS = 160 GHz.

In fibre B, after decreasing of the $PED-$curves for low input powers, the values of PED reach minima (PED = 48.5% at P_0 = 3.0 W for LFS = 40 GHz and only PED = 30%

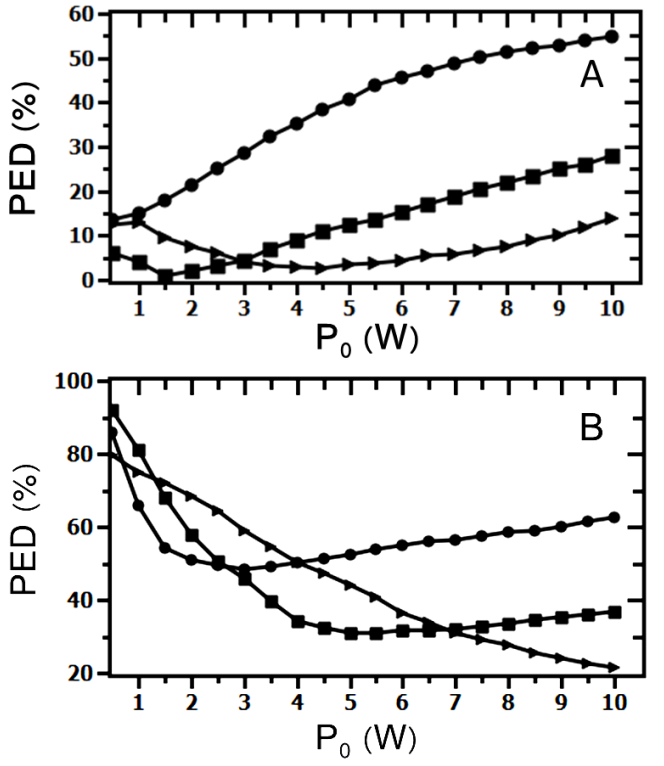

Figure 9.1: Pedestal content of optical pulses after propagation through fibre A and B for different values of input power P_0 and laser frequency separation LFS : LFS = 40 GHz (circles), LFS = 80 GHz (rectangles), and LFS = 160 GHz (triangles)

at P_0 = 5.0 W for LFS = 80 GHz) and then increase with P_0 again. For LFS = 160 W, a minimum of the pulse pedestal content is expected to occur for $P_0 > 10.0$ W. In the region 5.0 W $\leq P_0 \leq$ 10.0 W, the pulse pedestal content in fibre B varies between 53% and 65% for LFS = 40 GHz, between 30% and 38% for LFS = 80 GHz, and between 42% and 22% for LFS = 160 GHz. The pedestal contents in our case are slightly higher than the results presented in Ref. [103] for which the compression of higher-order solitons in dispersion-decreasing fibres was investigated.

Fig. 9.2 shows the figure of merit, FoM, for fibre A and B. Both fibres behave similarly: the less is the laser frequency separation, the better is the system performance in terms of figure of merit. Thus, we have the following values for fibre A: FoM = 25 for LFS = 40 GHz, FoM = 13 for LFS = 80 GHz, and FoM = 9 for LFS = 160 GHz at P_0 = 5 W. The values of FoM are even higher in fibre B: FoM = 115 for LFS = 40 GHz, FoM = 90 for LFS = 80 GHz, and FoM = 50 for LFS = 160 GHz at the same input power.

However, the evolution of pulse pedestals degrades the figure of merit in fibre B.

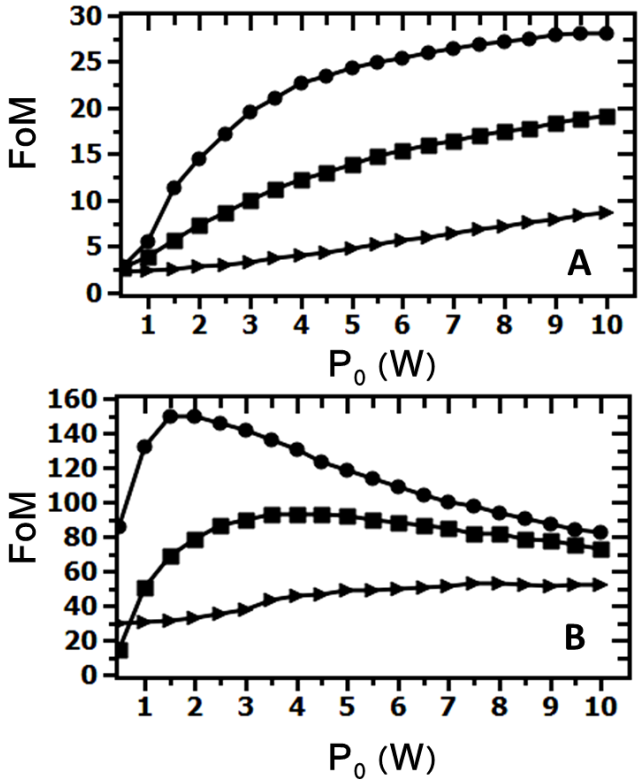

Figure 9.2: Figure of merit in fibre A and B for different values of input power P_0 and laser frequency separation LFS : LFS = 40 GHz (circles), LFS = 80 GHz (rectangles), and LFS = 160 GHz (triangles)

After the $FoM-$curves reach their maxima at P_0 = 1.5 W (LSF = 40 GHz) and P_0 = 4.0 W (LSF = 80 GHz), they start to decrease because more and more energy is lost into the pedestal and, thus, cannot be effectively transferred into the pulse peak power during the compression process. The $FoM-$curve for LFS = 160 GHz has a broad maximum of ca. FoM = 53 extending from P_0 = 5.0 W to a input-power value that lies beyond 10.0 W. This curve is also expected to decrease.

In Sec. 7, we identified the following input-power regions for the generation of best-possible OFC: 2.0 W < P_0 < 2.8 W for LFS = 80 GHz and 4.0 W < P_0 < 4.5 W for LFS = 160 GHz. Those are the regions before the corresponding $FoM-$ reach their maxima. Transferring this knowledge to the case of LFS = 40 GHz, we expect such input-power region to be 0.5 W < P_0 < 1.0 W. Those input-power values are, however, too low to induce the formation of a broad optical frequency comb.

Fig. 9.3 shows the compression factors for fibre A and B. For fibre A, the compression factors increase with the input power and decrease with the laser frequency separation.

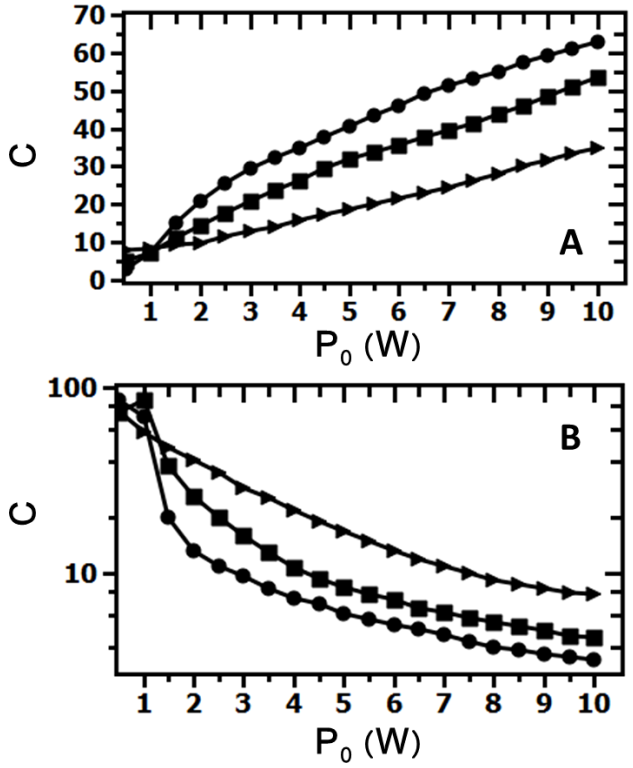

Figure 9.3: Compression factor for fibre A and B for different values of input power P_0 and laser frequency separation *LFS* : *LFS* = 40 GHz (circles), *LFS* = 80 GHz (rectangles), and *LFS* = 160 GHz (triangles)

This is because the compression effectiveness increases with the soliton order: we have $C = 40$ for *LFS* = 40 GHz ($N^A = 3.2$), $C = 31$ for *LFS* = 80 GHz ($N^A = 1.6$), and $C = 19$ for *LFS* = 160 GHz ($N^A = 0.81$) at $P_0 = 5.0$ W. The group-velocity dispersion, however, limits the further compression in fibre B: the compression factors decrease with the value of P_0 and *LFS*. At $P_0 = 5.0$ W, $C = 6$ for *LFS* = 40 GHz, $C = 8.5$ for *LFS* = 80 GHz, and $C = 17$ for *LFS* = 160 GHz. In our case, higher compression factors are achieved in the first fibre stage (fibre A), but lower ones in the second amplifying stage (fibre B) than the factors presented in Ref. [103].

9.2 Conclusion

In this section, we considered three different values of the initial laser separation, *LFS* = 40 GHz, *LFS* = 80 GHz, and *LFS* = 160 GHz, and calculated the relative energy pedestal content, *PED*, the figures of merit, *FoM*, and the compression factors, *C*, in fibres A and B of our motivating setup as functions of these values of *LFS* and the initial input power P_0.

For fibre A, we found that there are higher values of *PED* in the input-power regions of soliton crystal states. These values are, however, artificial and come around due to the mathematical formulation of *PED* (Eq. 9.1), the pulses themselves have almost no pedestals. In the P_0−region of separated solitons, the pedestal content in fibre A increases with P_0 and decreases with *LFS*. The maximal pedestal content of *PED* = 55% was observed for *LFS* = 40 GHz at P_0 = 10.0 W. For fibre B, minima of *PED*−curves were observed at P_0 = 3.0 W for *LFS* = 40 GHz (*PED* = 48.5%) and at P_0 = 5.0 W for *LFS* = 80 GHz (only *PED* = 30%).

As for the figure of merit *FoM*, we found that it is better for both, fibre A and B, if the value of *LFS* is small. At P_0 = 5.0 W, the highest values were achieved for *LFS* = 40 GHz: *FoM* = 25 in fibre A and *FoM* = 115 in fibre B. The evolution of pulse pedestals degrades, however, the figure of merit in fibre B: the *FoM*−curves decrease with P_0 after having maxima at P_0 = 1.5 W (*LFS* = 40 GHz) and P_0 = 4.0 W (*LFS* = 80 GHz).

The compression factors increase with the soliton order in fibre A. That means the value of *C* grows with P_0 and decreases with *LFS*. The group-velocity limits the compression effectiveness in fibre B. Therefore, the value of *C* in fibre B decreases with P_0 and *LFS*.

Altogether, the best performance in the considered input-power region was achieved for *LFS* = 80 GHz [40].

10 Intensity Noise and Optical Pulse Coherence

The pulse intensity noise (*IN*) leads to the reduction of the optical signal-to-noise ratio (OSNR) in the frequency domain and, so, degrades the quality of optical frequency combs. In fibre A of the proposed setup for generation of OFC for low- and medium resolution applications in Astronomy (Fig. 2.1), the increase of the initial intensity noise that comes from the two CW lasers can be caused by the modulational instability (Sec. 4.4.1) [124]. In the amplifying Er-doped fibre B, there are three reasons for the increase of the pulse intensity noise. First, any noise that comes from the first fibre stage and lies spectrally within the Raman gain is amplified due to the Raman amplification. Second, amplifying fibres generate additional noise due to the amplified spontaneous emission. This kind of noise is not included into our model (Eq. 3.46). Third, the modulational instability can also contribute to the increase of the *IN*−level in the second fibre stage [46]. As for the third fibre C, the main source of *IN* is the high nonlinearity of the fibre. It induces the soliton break-up with a subsequent emergence of subpulses. The subpulses propagate with slightly different central frequencies than the mother-solitons which constitutes a spectral noise floor additionally to the actual OFC.

The pulse intensity noise *IN* manifests itself in the pulse-to-pulse peak power variation (cf. Fig. 10.1C). We define the (maximum) *IN* as the difference between the maximum peak power within a pulse train at the end of each fibre, i.e. $\max(|\hat{A}|^2)$, and the according peak-power average, i.e. $\langle|\hat{A}|^2\rangle$, in percentage terms [40]:

$$IN = \frac{|\max(|\hat{A}|^2) - \langle|\hat{A}|^2\rangle|}{\langle|\hat{A}|^2\rangle} \cdot 100\%. \tag{10.1}$$

First, we study the intensity noise evolution in fibre B as a function of the initial laser frequency separation *LFS* and the input power P_0, we choose the following values: $LFS = 40$ GHz, $LFS = 80$ GHz, $LFS = 160$ GHz and $0.5\ \text{W} \leq P_0 \leq 10$ W. The initial intensity noise contribution is generated as a randomly distributed noise floor with the maximal power of $n_0 = 2P_0 10^{-8}$.

Then, we consider three cases of the initial *IN*−power (Eq. 3.47): the ideal case of $n_0 = 2P_0 10^{-10}$ that coincides with 90 dB OSNR, $n_0 = 2P_0 10^{-8}$ that corresponds to 70 dB OSNR, and $n_0 = 2P_0 10^{-6}$ that corresponds to 50 dB OSNR. The first case is hardly feasible in a real experiment, while two latter ones are, on the contrary, realistic [40].

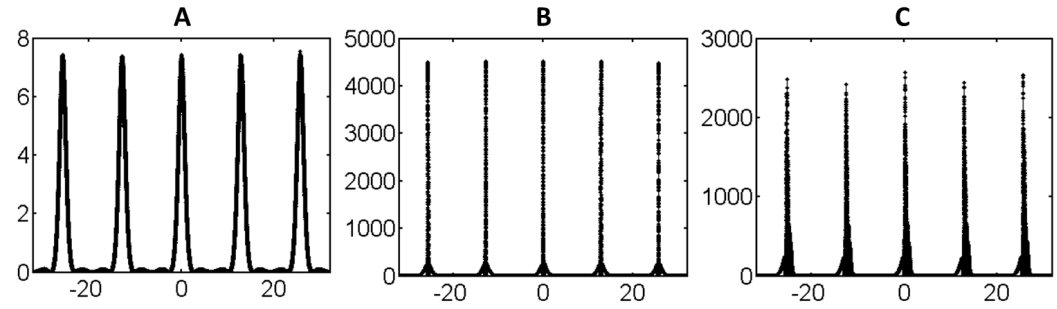

Figure 10.1: Optical pulse power (in W) as the function of time t (in ps) after propagation through different fibre stages of the proposed setup for generation of OFC for $\beta_2^A = -15$ ps^2/km, $LFS = 80$ GHz, and $P_0 = 2.0$ W. A: first fibre stage, B: second amplifying stage, C: third highly nonlinear fibre stage

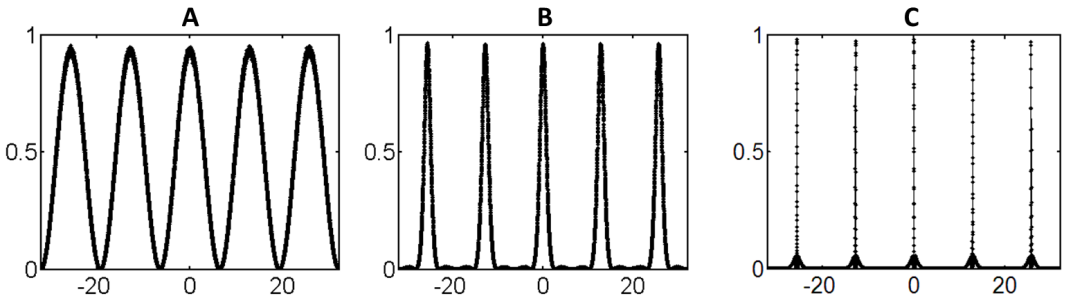

Figure 10.2: The coherence overlap function $\tilde{g}$ depending on the time t (in ps) made out of 10 pulse trains after propagation through different fibre stages of the proposed setup for generation of OFC for $\beta_2^A = -15$ ps^2/km, $LFS = 80$ GHz, and $P_0 = 2.0$ W. A: first fibre stage, B: second amplifying stage, C: third highly nonlinear fibre stage

The timing jitter of the optical pulses causes the broadening of the OFC lines. We study the impact of the timing jitter by means of the pulse coherence time T_c that we define as the FWHM of the pulses that arise by a pairwise overlapping of pulse trains generated at two different times, i and $i+1$, and that have, accordingly, different randomly generated initial $IN-$level. The overlap function is given by [40]

$$\tilde{g}(t) = \left\langle \frac{A_i^*(t) A_{i+1}(t)}{\sqrt{|A_i(t)|^2_{\max} |A_{i+1}(t)|^2_{\max}}} \right\rangle \tag{10.2}$$

where

$$|A_i|^2_{max} = \max(|A_i|^2) \tag{10.3}$$

is the maximum norm (cf. [45]). For the calculation of $\tilde{g}(t)$, we use 10 different pulse trains, i. e. $i \in (1, ..., 10)$ (compare Fig. 10.1 and Fig. 10.2). A high level of pulse coherence

corresponding to low timing jitter is given when $T_c > T_p$. Note, T_p is the pulse FWHM.

Afterwards, we show the effectiveness of the optical filtering technique in terms of the noise minimisation and the improvement of the optical pulse coherence characteristics. This filtering technique consists of two bandpass filters as described in Sec. 2.2 (Fig. 2.1) [40].

The following parameters for fibre A are chosen for our studies: $\beta_2^A = -15$ ps^2/km, $\beta_3^A = 0.1$ ps^3/km, $\gamma^A = 2.0$ W^{-1}km^1, and $\alpha^A = 0$ dB/km. The parameters of fibre B are set to: $\beta_2^B = -14$ ps^2/km, $\beta_3^B = 0.1$ ps^3/km, $\gamma^B = 2.5$ W^{-1}km^1, and $\alpha^B = 0$ dB/km. The simulations are performed in a time window of 256 ps sampled with 2^{16} points using optimised fibre lengths.

The dependence of the IN^B on different values of the GVD parameter of fibre A, β_2^A, is published in Ref. [40].

10.1 Intensity Noise in the Amplifying Fibre Depending on the Initial Laser Frequency Separation

Here, we consider the $IN-$level in the amplifying Er-doped fibre B as function of the laser frequency separation: $LSF = 40$ GHz, $LSF = 80$ GHz, and $LSF = 160$ GHz. The initial intensity noise contribution is generated as a randomly distributed noise floor with the maximal power of $n_0 = 2P_0 10^{-8}$.

Fig. 10.3 shows that, for input powers for which fibre A has plateaus in its optimum lengths (Fig. 8.4), the IN^B-level is very high. In this P_0-region, the optical pulses are not moulded into separated solitons yet when they propagate through fibre A, but constitute a collective soliton crystal state (Sec. 6). This soliton crystal state seems to lack the stability and the robustness of separated solitons to sustain the perturbation that is caused by the fibre parameter change at the conjunction between fibre A and B (the GVD parameter suddenly changes from $\beta_2^A = -15$ ps^2/km to $\beta_2^B = -14$ ps^2/km and the fibre nonlinearity changes from $\gamma^A = 2.0$ W^{-1}km^1 to $\gamma^B = 2.5$ W^{-1}km^1). As a result, the pulses break-up as they enter fibre B which yields a high level of IN^B for low input powers.

In the P_0-region in which an intermediate state between a soliton crystal and the separated solitons exists in fibre A, the stability of the optical structures grows as the input power increases, i.e. with the approaching of the P_0-region of the separated solitons. Here, the level of IN^B decreases until it reaches a minimum: $IN^B \leq 1\%$ for any considered values of LFS. The IN^B remains below 1% also for higher values of P_0 for $LSF = 80$ GHz and $LSF = 160$ GHz.

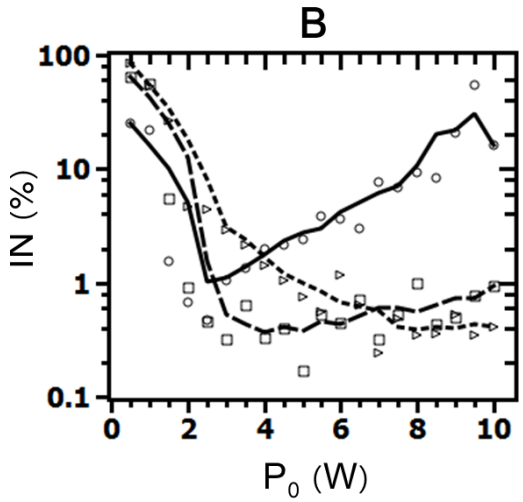

Figure 10.3: Intensity noise in fibre B, IN^B, in % vs. input power P_0 in W for different values of the initial laser frequency separation LFS : LFS = 40 GHz (circles), LFS = 80 GHz (rectangles), and LFS = 160 GHz (triangles) [40]

The soliton order is higher for smaller LFS (cf. Fig. 7.4). Higher-order solitons are subjected to a break-up due to the parameter change at the conjunction between fibre A and B. This leads to to the increase of the intensity noise. Therefore, the IN^B−level increases up to ca. 38% for LFS = 40 GHz for high values of P_0. An optimum system performance is shown for LSF = 80 GHz [40].

10.2 Intensity Noise Level Depending on the Initial Noise Power

Now, we choose LFS = 80 GHz to study the influence of the initial noise power on the noise characteristics in all three fibre stages of the proposed setup for generation of OFC for low- and medium resolution astronomical applications. We consider three values of the initial IN−power generated as a randomly distributed floor (Eq. 3.47): $n_0 = 2P_0 10^{-10}$, $n_0 = 2P_0 10^{-8}$ and $n_0 = 2P_0 10^{-6}$.

Fig. 10.4 shows that the whole system is sensitive to the value of the initial noise power. This dependence begins already in fibre A. Thus, IN^A takes the following values: ca. 0.1% for the ideal case of $n_0 = 2P_0 10^{-10}$, ca. 1% for $n_0 = 2P_0 10^{-8}$, and ca. 10% for $n_0 = 2P_0 10^{-6}$ [40].

As for fibre B, the IN^B−level is again very high for low input powers and any considered values of the initial intensity noises power. We assume, this is due to the fact that

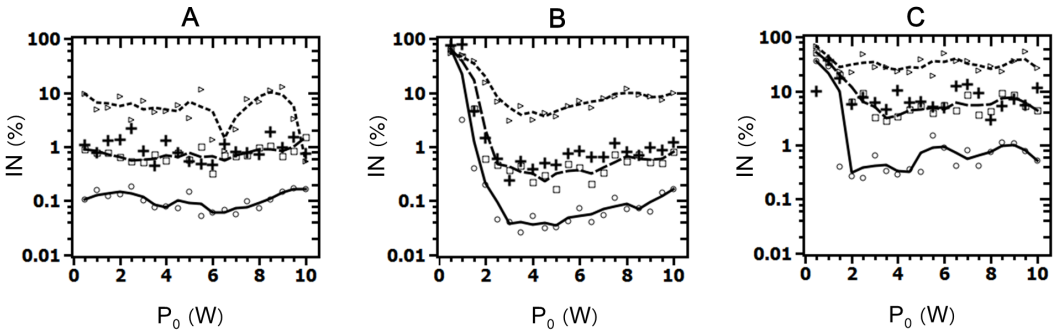

Figure 10.4: Intensity noise of fibres A, B, and C, IN^A, IN^B, and IN^C, in % vs. input power P_0 in W for different values of the initial noise power: $n_0 = 2P_0 10^{-10}$ (solid line), $n_0 = 2P_0 10^{-8}$ (dashed line), and $n_0 = 2P_0 10^{-6}$ (dotted line). The crosses present the intensity noise of the filtered signal [40]

the soliton crystal formed in fibre A in this input power region is unstable against perturbations based on the fibre parameter change. In the input-power region of separated solitons, 2.5 W $\leq P_0 <$ 8 W, the IN^B−level is almost the same as the level of IN^A in fibre A. That means that the Raman amplification has a negligible role on the intensity-noise evolution within the proposed approach for the OFC generation [40].

The nonlinearity of fibre C, however, induces the increase of a significant amount of IN^C, especially if the initial condition is highly noisy. So, we have IN^C of $< 1\%$ for $n_0 = 2P_0 10^{-10}$, ca. 6% for $n_0 = 2P_0 10^{-8}$, and ca. 40% for $n_0 = 2P_0 10^{-6}$ for the values of P_0 for which separated solitons exist in fibre A. Thus, to keept the level of the intensity noise as low as possible it is advisable to choose a low-noise initial condition [40].

Now we analyse the effectiveness of the proposed filtering technique. Two 20 dB−filters with 30 GHz bandwidth are used to filter the noise coming from the amplifiers (AMP1 and AMP2 in Fig. 2.1). The filters are modelled by two Gauss functions as described in Sec. 3.2.5. In our studies, the Gaussian-shaped filters reduce the amplifier noise floor with $n_0 = 2P_0 10^{-6}$ down to $n_0 = 2P_0 10^{-8}$ (Fig. 3.3). The according results are presented in Fig. 10.4 as crosses. As one can see, the crosses lie close to the curves that present the IN−level for the situation when a noise floor with $n_0 = 2P_0 10^{-8}$ is chosen as initial condition. To be precise, the IN^A_{filter} is ca. 2%, $IN^B_{\text{filter}} < 1\%$, and IN^C_{filter} is less than 12% for $P_0 > 2.5$ W. That means that the proposed filtering technique is highly effective in the suppression of intensity noise and should be deployed in a real experiment [40].

10.3 Optical Pulse Coherence in Fibres A, B, and C

Here, we consider the coherence time T_c for three different values of the input power P_0 and the initial noise IN with $n_0 = 2P_0 10^{-8}$ generated as a randomly distributed floor.

Fibre A			
P_0, [W]	*IN*	T_c, [ps]	T_p, [ps]
2.0	floor	6.16	1.58
	filtered	6.39	
5.5	floor	6.14	0.67
	filtered	6.28	
9.0	floor	6.15	0.46
	filtered	6.41	

Table 10.1: Coherence time T_c and FWHM of optical pulses T_p in fibre A for a floor and filtered initial noise with $n_0 = 2P_0 10^{-8}$ [40]

Fibre B			
P_0, [W]	*IN*	T_c, [ps]	T_p, [ps]
2.0	floor	1.56	0.06
	filtered	1.61	
5.5	floor	0.66	0.08
	filtered	0.67	
9.0	floor	0.46	0.09
	filtered	0.47	

Table 10.2: Coherence time T_c and FWHM of optical pulses T_p in fibre B for a floor and filtered initial noise with $n_0 = 2P_0 10^{-8}$ [40]

Afterwards, these results will be compared with the case when the initial noise level with $n_0 = 2P_0 10^{-6}$ is filtered down to $n_0 = 2P_0 10^{-8}$ by means of Gaussian filters as described above. The initial frequency separation is chosen to be $LFS = 80$ GHz [40].

As one notes from Tab. 10.1, the pulse width T_p decreases with the input power P_0 in fibre A due to the power-dependent compression process. Thus, we have $T_p = 1.58$ ps for $P_0 = 2.0$ W and $T_p = 0.46$ ps for $P_0 = 9.0$ W. However, for any values of P_0, the coherence time T_c remains almost the same, it slightly varies around the average value of $\langle T_c \rangle = 6.15$ ps. This value is much larger than the pulse FWHM T_p which indicates a high level of the pulse coherence and a low level of the timing jitter [40].

In fibre B (Tab. 10.2), the pulse widths T_p slightly increase with the input power P_0 due to the dispersion effects. So, we have $T_c = 0.06$ ps for $P_0 = 2.0$ W, $T_c = 0.08$ ps for $P_0 = 5.5$ W, and $T_c = 0.09$ ps for $P_0 = 9.0$ W. Contrary to fibre A, the value of T_c strongly depends on the initial power: $T_c = 1.56$ ps for $P_0 = 2.0$ W, $T_c = 0.66$ ps for $P_0 = 5.5$ W, and finally $T_c = 0.46$ ps for $P_0 = 9.0$ W. This occurs due to the pulse pedestal distortion with the increasing input power. Nonetheless, the coherence time T_c is more than 5 times larger than the pulse width T_p meaning still a good coherence performance with a low level of the timing jitter [40].

Fibre C			
P_0, [W]	*IN*	T_c, [ps]	T_p, [ps]
2.0	floor	0.07	0.06
	filtered	0.08	
5.5	floor	0.08	0.08
	filtered	0.09	
9.0	floor	0.09	0.09
	filtered	0.10	

Table 10.3: Coherence time T_c and FWHM of optical pulses T_p in fibre C for a floor and filtered initial noise with $n_0 = 2P_0 10^{-8}$ [40]

The optical pulses do not get compressed any further in fibre C (see Tab. 10.3). However, the values of the coherence time T_c drop after the pulses propagate through fibre C and are only a bit higher than the pulse widths T_p: $T_c = 0.07$ ps for $P_0 = 2.0$ W, $T_c = 0.08$ ps for $P_0 = 5.5$ W, and $T_c = 0.09$ ps for $P_0 = 9.0$ W. The reason for low coherence time is the break-up of the pulse pedestals into subpulses with irregular intensities and repetition time. This break-up is driven by the high fibre nonlinearity [40].

For the performed studies, the coherence time T_c of the filtered signal lies slightly below the T_c−values of the unfiltered (floor) noise. This has only a negligible reduction of the coherent OFC bandwidths. Thus, the proposed filtering technique proved to be effective once again [40].

10.4 Conclusion

In this section, we focused on the studies of the pulse intensity noise and the pulse coherence properties of different staged of the proposed fibre-based approach for generation of optical frequency combs for the calibration of astronomical spectrographs in the low- and medium resolution range (Sec. 2.2). For low-noise OFC with sharp frequency lines, it is necessary to produce optical pulses with a low level of intensity noise and a high level of coherence.

We considered the intensity noise IN^B in the second Er-doped amplifying fibre stage of the proposed setup as a function of the initial laser frequency separation *LFS*. First, we observed that the collective soliton crystal state formed in fibre A at low input powers is unstable against the perturbation that arises due to the sudden fibre parameter (GVD and fibre nonlinearity) change at the conjunction between fibre A and B. As a result, the pulses break up in fibre B which leads to the increase of IN^B up to 95%. At the current stage, we conclude that the input-power region of a pure collective soliton state should be avoided within a real experiment. However, further studies are needed to test the stability of the collective soliton state against different types of perturbations (fibre

paramter change, optical fibre losses, varying laser intensities) to make more precise statements about the source of the intensity noise in fibre B at low input powers. For the moment, the best system performance in terms of intensity noise is shown in the input-power region of separated solitons.

Further, the higher values of *LFS* yield lower values of IN^B for any values of the input power P_0 for which an intermediate state between a soliton crystal and separated solitons or just separated solitons are formed in fibre A. So, $IN^B < 1\%$ for $LSF = 160$ GHz and $LSF = 80$ GHz. For $LFS = 40$ GHz, the level of IN^B increased from $IN^B \approx 1\%$ to $IN^B \approx 38\%$ with the value of P_0. The reason for such increase of IN^B for a low value of *LFS* is the break-up of higher-order solitons due to the fibre parameter change at the conjunction between fibre A and B. Since the soliton order increases and, so, the probability of the pulse break-up goes up with the decreasing *LFS*, it is advisable to choose high *LSF* values to achieve low-noise OFC in the second fibre stage.

Having studied the influence of the initial intensity noise power n_0 (Eq. 3.47) on the system performance, we found that all three fibres are highly sensitive to the initial noise. Thus, $IN \approx 0.1\%$ for $n_0 = 2P_0 10^{-10}$ ($\propto$ 90 dB OSNR), $IN \approx 1\%$ for $n_0 = 2P_0 10^{-8}$ ($\propto$ 70 dB OSNR), and $IN \approx 10\%$ for $n_0 = 2P_0 10^{-6}$ ($\propto$ 50 dB OSNR) in fibre A and B. The high level of the material nonlinearity in fibre C induces the pulse break-up and, so, leads to the degradation of the $IN-$performance. Especially, if the initial condition is highly noisy. Thus, we have $IN^C \approx 1\%$ for $n_0 = 2P_0 10^{-10}$ and $IN^C \approx 40\%$ for $n_0 = 2P_0 10^{-6}$. So, for low-noise OFC, the initial intensity noise is to be kept as low as possible. For that, noise filtering techniques need to be deployed. Here, we showed that the techique consisting of two 20 dB bandpass filters (Fig. 2.1) is highly efficient in suppression of the initial intensity noise and should be used within a real experiment.

The studies of the coherence properties showed that the optical pulses exhibit a high level of coherence in fibre A and B: their coherence time T_c was much larger than the FWHM time T_p for the initial intensity noise power $n_0 = 2P_0 10^{-8}$. This coincides with a low level of the timing jitter. The coherence is degraded, i.e. the timing jitter is increased, in fibre C due to the break-up of the pulse pedestals (Fig. 2.2C). Here, the coherence time is the same as the pulse FWHM time which denotes a low level of the timing jitter. Although fibre C is necessary to broaden the OFC and to equalise the comb frequency lines, it degrades the OFC performance in terms of the optical-signal-to-noise ratio due to the increase of the pulse intensity noise and also contributes to the broadening of the frequecy lines due to the high level of the timing jitter. The proposed filtering technique consisting of two bandpass filters slightly improves the coherence time in all three fibres.

11 Overall Conclusion and Outlook

Within this work, we numerically studied the fibre-based approach for generation of optical frequency combs for the purpose of calibration of astronomical spectrographs in the low- and medium resolution range (Sec. 2.2). This approach consists of a conventional single-mode fibre, a suitably pumped amplifying Erbium-doped fibre with anomalous dispersion, and a subsequent low-dispersion highly nonlinear fibre. As a light source, two continuous-wave equally intense lasers emitting in the near infrared are used. The lasers are spectrally separated by an adjustable laser frequency separation *LFS* and generate a deeply-modulated cosine-wave with the central wavelength at $\lambda_c = 1531$ nm (Fig. 2.1).

The pulse-propagation equation that models this approach mathematically is a Generalised Nonlinear Schrödinger Equation (Eq. 3.46) that includes the group-velocity and the higher-order dispersion, the nonlinear interaction terms (the optical Kerr effect, the Raman effect, and the pulse self-steepening), the linear fibre losses, the wavelength-dependent Erbium gain profile for the second fibre of the proposed setup. A suitable initial condition equation that describes the radiation of two continuous-wave lasers is given in Eq. 3.47. The Fourth-Order Runge-Kutta Method in the Interaction Picture (RK4IP) is used for the numerical integration of Eq. 3.46 and Eq. 3.47.

To be able to control the quality and the bandwidth of the optical frequency combs, it is crucial to understand the pulse build-up in the first fibre of the proposed approach. For that, we used the Soliton Radiation Beat Analysis and found out that the deeply-modulated cosine-wave evolves into a collective soliton crystal state for input peak powers $P_0 \rightarrow 0$ W and a state of free, i.e. temporally well-separated, solitons for high input powers ($P_0 \rightarrow 6$ W). There is a continuous regime transition from the soliton crystal to free solitons with increasing input power denoting an intermediate state. Best possible optical frequency combs are achieved when the optical pulses are temporally and spectrally periodic. The intermediate state fulfills these requirements because, within this input-power region, only (well-behaving) fundamental solitons are generated, the temporal and spatial periodicity coming from the soliton crystal state is still imprinted into the pulses' features, and the energetic pulse pedestal content is low. With this knowledge, we determined the following input-power regions in which best possible optical frequency combs are achievable: 2.0 W $< P_0 <$ 3.5 W for $LFS = 80$ GHz, 3.5 W $< P_0 <$ 6.0 W for $LFS = 125$ GHz, and 4.0 W $< P_0 <$ 7.0 W for $LFS = 160$ GHz (Sec. 6).

In the second fibre of the proposed approach, the optical pulses (solitons) are am-

plified due to the Erbium amplification and, at the same time, extremely compressed. We again apply the Soliton Radiation Beat Analysis to determine if the compression process is adiabatic or non-adiabatic. We found that the pulse build-up in the Erbium-doped amplifying fibre critically depends on the features of the pulses formed in the first fibre of the proposed approach. So, adiabatic soliton compression occurs for low and medium vaues of the input power. For high values of the input power, the pulses undergo a non-adiabatic compression that goes along with the emergence of subpulses (soliton fission) which should be prevented since it increases the level of the intensity noise and degrades the frequency comb quality. The soliton fission occurs for input power values $P > 2.8$ W for $LFS = 80$ GHz and $P > 4.5$ W for $LFS = 160$ GHz. The best optical frequency combs are expected to evolve in the second fibre for the input powers $2.0\,\mathrm{W} < P_0 < 2.8\,\mathrm{W}$ for $LFS = 80\,\mathrm{GHz}$ and $4.0\,\mathrm{W} < P_0 < 4.5\,\mathrm{W}$ for $LFS = 160\,\mathrm{GHz}$ (Sec. 7).

Optimum fibre lengths denote propagation points at which the optical pulses are maximally compressed and, so, provide, the broadest possible optical frequency combs, and exhibit the minimum level of pulse intensity noise. Such optimum lengths should be used within a real experiment. Having excluded the optical losses, we found that the optimum lengths of the first fibre vary in the range of $180\,\mathrm{m} < L^A_{opt} < 980\,\mathrm{m}$ depending on the initial power P_0 and the group-velocity dispersion parameter β^A_2. The corresponding optimum lengths of the second fibre take the values of $7.5\,\mathrm{m} < L^B_{opt} < 37.5\,\mathrm{m}$. For different values of LFS and P_0, the optimum lengths were $150\,\mathrm{m} < L^A_{opt} < 1100\,\mathrm{m}$ for the first fibre and $7\,\mathrm{m} < L^A_{opt} < 35\,\mathrm{m}$ for the second fibre. The best system performance in terms of optimum lengths was shown for $\beta^A_2 = -15\,\mathrm{ps}^2/\mathrm{km}$ and $LSF = 80$ GHz. Using these values, we showed that the typical optical fibre losses of $\alpha^A = 0.2$ dB/km can be neglected for $P_0 > 3.0$ W since they do not change the system behaviour in a significant way. In the input-power region $P_0 \leq 3.0$ W, the formation of temporally periodic optical pulses is strongly affected by the optical attenuation. Therefore, the determination of the optimum lengths is not possible (Sec. 8).

As the optical pulses propagate through the fibres, their total energy gets split between the pulses and the broad pedestals. The energy lost into the pedestals cannot be effectively used for pulse the compression process and the increase of the pulse peak power. Therefore, it is advisable to keep the pedestal content PED as low as possible by a proper choice of the system parameters. To describe the amount of energy that remains in the pulse and does not get lost into the pedestal, we introduce a figure of merit FoM that is defined as the ratio between the peak power of a pulse and its average power. The pulse compression effectiveness is described by the compression factor C that is given as the ratio between the pulse width at the beginning of a fibre and the pulse width at the optimum length. For the first fibre of the proposed approach for generation of optical frequency combs, we found that the pulses have almost no pedestals in the input-power region of soliton crystal states. In the P_0-region of separated solitons, the pedestal content in the first fibre increases with P_0 and decreases with LFS. The maximal

pedestal content of $PED = 55\%$ was observed for $LFS = 40$ GHz at $P_0 = 10.0$ W. For the second fibre, minima of $PED-$curves were observed at $P_0 = 3.0$ W for $LFS = 40$ GHz ($PED = 48.5\%$) and at $P_0 = 5.0$ W for $LFS = 80$ GHz (only $PED = 30\%$). As for the figure of merit FoM, we found that it is better for both fibres if the value of LFS is small. At $P_0 = 5.0$ W, the highest values were achieved for $LFS = 40$ GHz: $FoM = 25$ in the first fibre and $FoM = 115$ in the second fibre. The evolution of pulse pedestals degrades, however, the figure of merit in the second fibre: the $FoM-$curves decrease with P_0 after having maxima at $P_0 = 1.5$ W ($LFS = 40$ GHz) and $P_0 = 4.0$ W ($LFS = 80$ GHz). The compression factors increase with the soliton order in the first fibre meaning that the value of the compression factor grows with P_0 and decreases with LFS. The group-velocity limits the compression effectiveness in the second fibre. Therefore, the compression factor value in fibre B decreases with P_0 and LFS. The best system performance in the considered input-power region was achieved for $LFS = 80$ GHz (Sec. 9).

The optical frequency noise leads to the reduction of the optical signal-to-noise ratio of the frequency combs, whereas the timing jitter yield the broadening of the comb lines. Therefore, to obtain low-noise optical frequency combs with sharp frequency lines, it is necessary to produce optical pulses with a low level of intensity noise and a high level of coherence. Here, we found that higher values of the laser frequency separation LFS yield lower values of the intensity noise IN^B in the second amplifying fibre for any values of the input power P_0 for which an intermediate state between a soliton crystal and separated solitons or just separated solitons are formed in the first fibre. So, $IN^B < 1\%$ for $LSF = 160$ GHz and $LSF = 80$ GHz. For $LFS = 40$ GHz, the level of IN^B increased from $IN^B \approx 1\%$ to $IN^B \approx 38\%$ with the value of P_0. Therefore, it is advisable to choose high LSF values to achieve low-noise OFC in the second fibre stage. Having studied the influence of the initial intensity noise power n_0 (Eq. 3.47) on the system performance, we found that all three fibres are highly sensitive to the initial noise. Thus, $IN \approx 0.1\%$ for $n_0 = 2P_0 10^{-10}$ ($\propto$ 90 dB OSNR), $IN \approx 1\%$ for $n_0 = 2P_0 10^{-8}$ ($\propto$ 70 dB OSNR), and $IN \approx 10\%$ for $n_0 = 2P_0 10^{-6}$ ($\propto$ 50 dB OSNR) in the first and second fibre. In the third fibre, we have $IN^C \approx 1\%$ for $n_0 = 2P_0 10^{-10}$ and $IN^C \approx 40\%$ for $n_0 = 2P_0 10^{-6}$. So, for low-noise OFC, the initial intensity noise is to be kept as low as possible. We showed that the techique consisting of two 20 dB bandpass filters is highly efficient in suppression of the initial intensity noise and should be used within a real experiment. The studies of the coherence properties showed that the optical pulses exhibit a high level of coherence in the first and second fibre which coincides with a low level of the timing jitter. The coherence is degraded, i.e. the timing jitter is increased, in fibre C due to the break-up of the pulse pedestals. The proposed filtering technique consisting of two bandpass filters slightly improves the coherence time in all three fibres (Sec. 10).

A better understanding of the pulse build-up in the first fibre and the second fibre is needed to be able to gain a full control of the proposed approach for generation of optical frequency combs for the purpose of the calibration of the astronomical low- and medium resolution spectrographs. For the first fibre, one should perform the Soliton Radiation

Beat Analysis for different fibre parameters (the group-velocity dispersion and the fibre nonlinearity) as well as to include the typical optical fibre losses of 0.2 dB/km to see if the change of these parameters might affect the pulse build-up and, thus, the frequency comb quality. To gain a better understanding of the pulse build-up in the second fibre, one should include an Erbium-saturation term into the pulse-propagation equation Eq. 3.46 as well as take the optical losses into account and perform the Soliton Radiation Beat Analysis with longer propagation lengths as chosen here, i.e. with lengths > 40 m. Within a real experiment, it might be difficult to achieve the absolute equality of the laser intensities. Therefore, the effect of the laser intensity variations on the formation of the soliton crystal and an intermediate state in the first fibre should be thoroughly studied by means of the Soliton Radiation Beat Analysis as well. Further, studies on the stability of the soliton crystal state agains perturbations that arise due to the fibre parameter change as the optical pulses enter the second fibre should be performed to see if the (in)stability of the soliton crystal might lead to the increase of the intensity noise in the second fibre.

Acronyms

In the order of appearance:

OFC optical frequency comb / optical frequency combs

CW continuous wave

LFS laser frequency separation

GNLS Generalised Nonlinear Schrödinger Equation

GVD group-velocity dispersion

NIR near IR (infra-red)

AIP Institute for Astrophysics Potsdam (AIP)

FWM four-wave mixing

HNLF highly nonlinear fibre

EDFA Erbium-doped fibre amplifier

CCD charge-coupled device

BBO beta barium borate

SVEA slowly varying envelope approximation

RK4IP Fourth-Order Runge-Kutta Method in the Interaction Picture

NLS Nonlinear Schrödinger Equation

TOD third-order dispersion

RK4 Fourth-Order Runge-Kutta Method

FFT fast Fourier transform

DMF dispersion-managed fibre

MI modulational instability

AB Akhmediev breather

KM Kuznetsov-Ma soliton

SRBA Soliton Radiation Beat Analysis

IC initial condition

IN intensity noise

L_{opt} optimum fibre length

FWHM full width at half maximum

PED pulse pedestal

FoM figure of merit

C compression factor

Bibliography

[1] T. Udem, R. Holzwarth, T. Hänsch, European Ohysicsl Journal **172** (2009)

[2] J. Ye, S. T: Cundiff, *Femtosecond Optical Frequency Comb: Principle, Operation and Application.* Springer (2005)

[3] T. Hänsch, *Laser Frequency and Time*. `https://www.cfa.harvard.edu/~hrs/icap2002/proceedings/Haensch.pdf`

[4] H. Y. Ryu, H. S. Moon, H. S. Suh, Optics Express **Vol. 15, No. 18** (2007)

[5] N. Yamamoto, K. Akahane, T. Kawanishi, R. Katouf, H. Sotobayashi, Japanese Journal of Applied Physics **49**, 04DG03 (2010)

[6] H. Jung, K. Y. Fong, X. Zhang, H. X. Tang, Optics Letters Vol. 38, Issue 15 (2013)

[7] P. Del'Haye, A. Schliesser, O. Arcizet, T. Wilken, R. Holzwarth, T. J. Kippenberg, Nuture Letters **Vol. 450** (2007)

[8] N. Leindecker, A. Marandi, R. L. Byer, K. L. Vodopyanov, Optics Express **Vol. 19, No. 7** (2011)

[9] S. T. Cundiff, J. Yen, Reviews of Modern Physics **75** (2003)

[10] J. M. Dudley, G. Genty, F. Dias, B. Kibbler, N. Akhmediev, Optics Express **Vol. 17, No. 24** (2009)

[11] G. Yang, L. Li, S. Jia, D. Mihalache, Romanian Reports in Physics **Vol. 65, No. 3** (2013)

[12] S. Pitois, J. Fatome, G. Millot, Optics Letters **Vol. 27, No. 19** (2002)

[13] C. Finot, J. Fatome, S. Pitois, G. Millot, IEEE Photonics Technology Letters **Vol. 19, No. 21**, (2007)

[14] C. Fortier, B. Kibler, J. Fatome, C. Finot, S. Pitois, G. Millot, Laser Physics Latters **Vol. 5, No. 11** (2008)

[15] J. Fatome, S. Pitois, C. Fortier, B. Kibler, C. Finot, G. Millot, C. Courde, M. Lintz, E. Samain, Transparent Optical Networks, ICTON'09 (2009)

[16] I. El Mansouri, J. Fatome, C. Finot, M. Lintz, S. Pitois, IEEE Photonics Technology Letters **Vol. 23, No. 20** (2011)

[17] J. Fatome, S. Pitois, C. Fortier, B. Kibler, C. Finot, G. Millot, C. Courde, M. Lintz, E. Samain, Optics Communications **283** (2010)

[18] K. E. Webb, M. Erkintalo, Y. Xu, N. G. R. Broderick, J. M. Dudley, G. Genty, S. G. Murdoch, Nuture Communications **5** (2014)

[19] K. Griest, J. B. Whitmore, A. M. Wolfe, J. X. Prochaska, J. C. Howk, G. W. Marcy, The Astrophysical Journal **708** (2010)

[20] S. Osterman, S. Diddams, M. Beasley, C. Froning, L. Hollberg, P. MacQueen, V. Mbele, A. Weiner, Proceedings of SPIE **6693** (2007)

[21] S. Osterman, G. G. Ycas, S. A. Diddams, F. Quinlan, S. Mahadevan, L. Ramsey, C. F. Bender, R. Terrien, B. Botzer, S. Sigurdsson, S. L. Redman, Proceedings of SPIE **8450** (2012)

[22] G. G. Ycas, F. Quinlan, S. A. Diddams, S. Osterman, S. Mahadevan, S. Redman, R. Terrien, L. Ramsey, C. F. Bender, B. Botzer, S. Sigurdsson, Optics Express **Vpl. 20, No. 6** (2012)

[23] A. Loeb, The Astrophysical Journal **499** (1998)

[24] W. L. Freedman, Proceeding of the National Academy of Sciences USA **95(1)** (1998)

[25] M. T. Murphy, C. R. Locke, P. S. Light, A. N. Luiten, J. S. Lawrence,Monthly Notices of the Royal Astronomical Society **000** (2012)

[26] D. F. Phillips, A. G. Glenday, Ch.-H. Li, C. Cramer, G. Furesz, G. Chang, A. J. Benedick, L.-J. Chen, F. X. Kärtner, S. Korzennik, D. Sasselov, A. Szentgyorgyi, R. L. Walsworth, Optics Express **Vol. 20 No. 13** (2012)

[27] D. A. Braje, M. S. Kirchner, S. Osterman, T. Fortier, A. Diddams, European Physical Journal D **Vol. 48, Issue 1** (2008)

[28] M. T. Murphy, T. Udem, R. Holzwarth, A. Sizmann, L. Pasquini, C. Araujo-Hauck, H. Dekker, S. D'Odorico, M. Fischer, T. W. Hänsch, A. Manescau, Monthly Notices of the Royal Astronomical Society **Vol. 380, No. 2** (2007)

[29] G. Lo Curto, A. Manescau, G. Avila, L. Pasquini, T. Wilken, T. Steinmetz, R. Holzwarth, R. Probst, T. Udem, T. W. Hänsch, Proceedings of SPIE **8446** (2012)

[30] T. Wilken, C. Lovis, A. Manescau, T. Steinmetz, L. Pasquini, G. Lo Curto, T. W. Hänsch, R. Holzwarth, T. Udem Proceedings of SPIE **7735**, 77350T-1 (2010)

[31] T. Steinmetz, T. Wilken, A. Araujo-Hauck, R. Holzwarth, T. W. Hänsch, L. Pasquini, A. Manescau, S. D'Odorico, M. T. Murphy, T. Kentischer, W. Schmidt, T. Udem, Science **Vol. 321, No. 5894** (2008)

[32] H.-P. Doerr, T. J. Kentischer, T. Steinmetz, R. A. Probst, M. Franz, R. Holzwarth, T. Udem, T. W. Hänsch, W. Schmidt, Proceedings of SPIE **8450** (2012)

[33] A. Kelz, S. M. Bauer, I. Biswas, T. Fechner, T. Hahn, J.-C. Olaya, E. Popow, M. M. Roth, O. Streicher, P. Weilbacher, R. Bacon, F. Laurent, U. Laux, J. L. Lizon, M. Loupias, R. Reiss, G. Rupprecht, Proceedings of SPIE **7735**, 773552 (2010)

[34] R. S. de Jong et. al, Proceedings of SPIE **8446** (2012)

[35] R. de Jong, Telescopes and Instrumentation, The Messenger **145** (2011)

[36] P. Del'Haye, T. Herr, E. Gavartin, M. L. Gorodetsky, R. Holzwarth, T. J. Kippenberg, Physical Review Letters **107** (2011)

[37] J. M. Chavez Boggio, A. A. Rieznik, M. Zajnulina, M Böhm, D. Bodenmüller, M. Wysmolek, H. Sayinc, J. Neumann, D. Kracht, R. Haynes, M. M. Roth, Proceedings of SPIE **8434** (2012)

[38] M. Zajnulina, J. M. Chavez Boggio, A. A. Rieznik, R. Haynes, M. M. Roth, Proceedings of SPIE **8775** (2013)

[39] M. Zajnulina, M. Böhm, K. Blow, J. M. Chavez Boggio, A. A. Rieznik, R. Haynes, M. M. Roth, Proceedings of SPIE **9151** (2014)

[40] M. Zajnulina, J. M. Chavez Boggio, M. Böhm, A. A. Rieznik, T. Fremberg, R. Haynes, M. M. Roth, Applied Physics B **Vol. B 120, Number 1** (2015)

[41] Z. Tong, A. O. J. Winberg, E. Myslivets, B. P. P. Kuo, N. Alic, S. Radic, Optics Express **Vol. 20, No. 16** (2012)

[42] E. Myslivets, B. P. P. Kuo, N. Alic, S. Radic, Optics Express **Vol. 20, No. 3** (2012)

[43] T. Yang, J. Dong, S. Liao, D. Huang, X. Zhang, Optics Express **Vol. 21, Issue 7** (2013)

[44] F. C. Cruz, *Optical Frequency Combs Generated by Four-Wave Mixing in Optical Fibers for Astronomical Spectrometer Calibration and Metrology* `http://arxiv.org/ftp/arxiv/papers/0806/0806.0416.pdf`

[45] G. Agrawal, *Nonlinear Fiber Optics.* Academic Press (2013)

[46] G. P. Agrawal, *Applications of Nonlinear Fiber Optics.* Academic Press (2008)

[47] S. Liu, Applied Physics Letters **89**, 171118 (2006)

[48] S. Arismar Cerqueira Jr., J. D. Marconi, H. E. Hernandez-Fiqueroa, H. L. Fragnito, PIERS Proceedings (2009)

[49] S. A. Cerqueira Jr., J. M. Chavez Boggio, A. A. Rieznik, H. E. Hernandez-Figueroa, H. L. Fragnito, J. C. Knight, Optics Express **Vol. 16, No. 4** (2008)

[50] S. A. S. Melo, S. A. Cerqueira Jr., A. R. do Nascimento Jr., L. H. H. Carvalho, R. Silva, J. C. R. F. Oliveira, Revista Telecomunicacoes **Vol. 15, No. 2** (2013)

[51] L. F. Mollenauer, R. H. Stolen, J. P. Gordon, W. J. Tomlinson, Optics Letters **Vol. 8, No. 5** (1983)

[52] H. A. Haus, IEEE Spectrum **0018-9235** (1993)

[53] P. Colman, C. Husko, S. Combrie, I. Sagnes, C. W. Wong, A. De Rossi, Nature Photonics **Vol. 4** (2010)

[54] A. A. Voronin, A. M. Zheltikov, Physical Review A **Vol. 78, Issue 6** (2008)

[55] T. Inoue, S. Namiki, Laser and Photonics Review **2, No. 1** (2008)

[56] W. Demtröder, *Laserspektroskopie.* Springer (1993)

[57] V. G. Dominic, *Secomd-Harmonic Generation in Optical Fibers and Glass.* Final report, University of Southern California (1992)

[58] D. Z. Anderson, V. Mizrahi, J. E. Sipe, Optics Letters **Vol. 16. No. 11** (1991)

[59] J. Moses, F. W. Wise, Physical Review Letters **97**, 073903 (2006)

[60] W. Nolting, *Grundkurs Theoretische Physik 3. Elektrodynamik.* Springer (2004)

[61] M. Zajnulina, *Nonlinear Phenomena in Coupled Silicon-on-Insulator Waveguides.* Diploma thesis, Technical University Berlin (2012)

[62] C. J. Benton: *Solitons and Nonlinear Optics in Silicon-on-Insulator Photonic Wires.* PhD thesis, University of Bath (2009)

[63] J. Hunt, Journal of Lightwave Technology **Vol. 25, No. 12** (2007)

[64] T. Hohage, F. Schmidt, *On the Numerical Solution of Nonlinear Schrödinger Type Equations in Fiber Optics.* ZIB-Report 02-04 (2002)

[65] Z. Zhang, L. Chen, X. Bao, Optics Express **Vol. 18, No. 8** (2010)

[66] S. Balac, A. Fernandez, F. Mahé, F. Méhats, R. Texier-Picard, HAL Id: hal-00850518, `https://hal.archives-ouvertes.fr/hal-00850518v1/document`

[67] P. G. Drazin, R. S. Johnson: *Solitons: An Introduction.* Cambridge University Press (1989)

[68] N. J. Zabusky, M. D. Kruskal, Physical Review Letters **Vol. 15, No. 6** (1965)

[69] R. K. Dodd, J. C. Eilbeck, J. D. Gibbon, H. C. Morris, *Solitons and Nonlinear Wave Equations.* Academic Press (1982)

[70] T. Aktosun, F. Demontis, C. van der Mee, Inverse Problems **Vol. 23, No. 5** (2007)

[71] T. Aktosun, T. Busse, F. Demontis, C. van der Mee, Topics in Operator Theory: Advances and Applications **Vol. 203** (2010)

[72] L. Lam, *Nonlinear Physics for Beginners. Fractals, Chaos, Solitons, Pattern Formation, Cellular Automata and Complex Systems.* World Scientific (1998)

[73] L. Lam, *Introduction to Nonlinear Physics.* Springer (1997)

[74] K. Porsezian, V. C. Kuriakose, *Optical Solitons. Theoretical and Experimental Challenges.* Lecture Notes in Physics, Springer (2003)

[75] A. J. Scroggie, J. Jeffers, G. McCartney, G.-L. Oppo, Physical Review E **71**, 046602 (2005)

[76] P. Coullet, C. Riera, C. Tresser, Chaos **14** (2004)

[77] M. Zajnulina, C. McIntyre, G.-L. Oppo CLEO Europe - EQEC (2009)

[78] E. Yusufoglu, A. Bekir, Mathematical and Computer Modelling **48** (2008)

[79] I. S. Aranson, arXiv: cond-mat/0106115v1 (2001)

[80] L. A. Lugiato, R. Lefever, Physical Review Letters **58** (1987)

[81] F. Mitschke, A. Hause, C. Mahnke, P. Rohrmann, Nonlinear Phenomena in Complex Systems **Vol. 15, No. 4** (2012)

[82] S. R. Friberg, K. W. DeLong, Optics Letters **Vol. 17, No. 14** (1992)

[83] S. Turitsyn, B. G. Bale, M. P. Fedoruk, Physics Reports **Vol. 25, Issue 4** (2012)

[84] K. J. Blow, N. J. Doran, D. Wood, Optical Society of America B **Vol. 5** (1988)

[85] N. Akhmediev, A. Ankiewicz, *Dissipative Solitons: From Optics to Biology and Medicine.* Springer (2008)

[86] B. Bendow, P. D. Gianino, Journal of Optical Society of America **Vol. 70, No. 5** (1980)

[87] K. J. Blow, N. J. Doran, D. Wood, Optics Letters **Vol. 12** (1987)

[88] A. Hause, H. Hartwig, B. Seifert, H. Stolz, M. Böhm, F. Mitschke, Physical Review A **75**, 063836 (2007)

[89] A. Hause, H. Hartwig, M. Böhm, F. Mitschke, Physical Review A **78**, 063817 (2008)

[90] P. Rohrmann, A. Hause, F. Mitschke, Scientific Reports **2:866** (2012)

[91] P. Rohrmann, A. Hause, F. Mitschke, Physical Review A **87**, 043834 (2013)

[92] A. Boudjemaa, U. Al Khawaja, Physical Review A **88**, 045801 (2013)

[93] S. M. Alamoudi, U. Al Khawaja, B. B. Baizakov, Physical Review A **89**, 053817 (2014)

[94] K. Hammani, B. Wetzel, B. Kibler, J. Fatome, C. Finot, G. Millot, N. Akhmediev, J. M. Dudley, Optics Letters **Vol. 36, Issue 11** (2011)

[95] N. N. Akhmediev, V. I. Korneev, Teoreticheskaya i Matematicheskaya Fizika, **Vol. 69, No. 2** (1986)

[96] C. Mahnke, F. Mitschke, Physical Review A **85**, 033808 (2012)

[97] B. Kibler, J. Fatome, C. Finot, G. Millot, F. Dias, G. Genty, N. Akhmediev, J. M. Dudley, Nature Physics **6** (2010)

[98] K. Hammani, B. Kibler, C. Finot, P. Morin, J. Fatome, J. M. Dudley, G. Millot, Optics Letters **Vol. 36, Issue 2** (2011)

[99] B. Kibler, J. Fatome, C. Finot, G. Millot, G. Genty, B. Wetzel, N. Akhmediev, F. Dias, J. M. Dudley, Scientific Reports **2:463** (2012)

[100] D. J. Kedziora, A. Ankiewicz, N. Akhmediev, Physical Review E **85**, 066601 (2012)

[101] S. V. Chernikov, E. M. Dianov, Optics Letters **Vol. 18, No. 7** (1993)

[102] W. Cao, P. K. A. Wai, Optics Communications **221** (2003)

[103] Q. Li, J. N. Kutz, P. K. A. Wai, Journal of Optical Society of America B **Vol. 27, No. 11** (2010)

[104] A. Komarov, F. Amrani, A. Dmitriev, K. Komarov, D. Meshcheriakov, F. Sanchez, Physical Review A **85**, 013802 (2012)

[105] S. V. Chernikov, P. V. Mamyshev, Journal of the Optical Society of Americal **Vol. 8, No. 8** (1991)

[106] P. V. Mamyshev, P. G. J. Wigley, G. I. Stegeman, V. A. Semenov, E. M. Dianov, S. I. Miroshnichenko, Physical Review Letters **Vol. 71, No. 1** (1993)

[107] M. L. Quiroga-Teixeiro, D. Anderson, P. A. Andrekson, A. Berntson, M. Lisak, Journal of Optical Society of America B **Vol. 13, No. 4** (1996)

[108] M. Böhm, F. Mitschke, Physical Review **E** 73, 066615 (2006)

[109] M. Böhm, F. Mitschke, Applied Physics B **Vol. 86, Issue 73** (2007)

[110] M. Zajnulina, M. Böhm, K. Blow, J. M. Chavez Boggio, A. A. Rieznik, R. Haynes, M. M. Roth, Proceedings of SPIE **9151**, 91514V (2014)

[111] M. Zajnulina, M. Böhm, K. Blow, A. A. Rieznik, D. Giannone, R. Haynes, M. M. Roth: *Soliton Radiation Beat Analysis of Optical Pulses Generated from Two CW Lasers.* Accepted for publication with *Chaos: An Interdisciplinary Journal of Nonlinear Science*, Manuscript #15408R (2015)

[112] F. J. Harris, Proceedings of the IEEE **Vol. 66, No. 1** (1978)

[113] M. Böhm, *Analyse des Solitonengehaltes von optischen Impulsen in Glasfasern.* Universität Rostock (2009)

[114] R. Taylor, *Optical Solitons: Theory and Experiment.* Cambridge University Press (1992)

[115] A. Hause, F. Mitschke, Physical Review A **82**, 043838 (2010)

[116] M. Böhm, F. Mitschke, Physical Review A **76**, 063822 (2007)

[117] G. P. Agrawal, Physical Review A **Vol. 44, No. 11** (1991)

[118] M. J. Hayduk, *Passively Mode-Locked Erbium-Doped Fiber Lasers Using Multiple Quantum Well Saturable Absorbers.* Air Force Research Laboratory (1998)

[119] B. S. Wang, G. Puc, M. Andrejco, Proceedings of SPIE **5623** (2005)

[120] F. I. Vasile, P. Schiopu, Journal of Optoelectronics and Advanced Materials **Vol. 6, No. 4** (2004)

[121] M. J. Ablowitz, T. P. Horikis, S. D. Nixon, D. Frantzeskakis, Optics Letters **Vol. 36, Issue 6** (2011)

[122] S. M. Kobtsev, S. V. Smirnov, Optics Express **Vol. 16, No. 10** (2008)

[123] S. M. Kobtsev, S. V. Smirnov, Optics Express **Vol. 14, No. 9** (2006)

[124] S. M. Kobtsev, S. V. Smirnov, Optics Express **Vol. 13, No. 18** (2005)